**Naval Research Laboratory**
Washington, DC 20375-5320

NRL/5340/FR--2021/3

# Sparse Aperture Multistatic Radar Imaging Techniques: Final Report

MATTHEW J. BURFEINDT
HATIM F. ALQADAH

*Surveillance Technology Branch*
*Radar Division*

January 3, 2022

# REPORT DOCUMENTATION PAGE

**PLEASE DO NOT RETURN YOUR FORM TO THE ABOVE ORGANIZATION**

| | | | |
|---|---|---|---|
| **1. REPORT DATE** | **2. REPORT TYPE** | **3. DATES COVERED** | |
| | | **START DATE** | **END DATE** |
| January 3, 2022 | Formal Report | October 1, 2018 | October 1, 2021 |

**4. TITLE AND SUBTITLE**
Sparse Aperture Multistatic Radar Imaging Techniques: Final Report

| | | |
|---|---|---|
| **5a. CONTRACT NUMBER** | **5b. GRANT NUMBER** | **5c. PROGRAM ELEMENT NUMBER**<br>61153N |
| **5d. PROJECT NUMBER** | **5e. TASK NUMBER** | **5f. WORK UNIT NUMBER**<br>1L40 |

**6. AUTHOR(S)**
Matthew J. Burfeindt, Hatim F. Alqadah

| | |
|---|---|
| **7. PERFORMING ORGANIZATION / AFFILIATION NAME(S) AND ADDRESS(ES)**<br>U. S. Naval Research Laboratory<br>4555 Overlook Avenue, SW<br>Washington, DC 20375-5320 | **8. PERFORMING ORGANIZATION REPORT NUMBER**<br>NRL/5340/FR--2021/3 |

| | | |
|---|---|---|
| **9. SPONSORING / MONITORING AGENCY NAME(S) AND ADDRESS(ES)** | **10. SPONSOR / MONITOR'S ACRONYM(S) NUMBER**<br>NRL | **11. SPONSOR / MONITOR'S REPORT NUMBER(S)** |

**12. DISTRIBUTION / AVAILABILITY STATEMENT**
DISTRIBUTION STATEMENT A: Approved for public release; distribution is unlimited.

**13. SUPPLEMENTAL NOTES**

**14. ABSTRACT**

We report outcomes for an NRL 6.1 Base Program project towards the development of new multistatic-multiview radar imaging techniques from sparse sensors. The algorithmic framework for the techniques is the Linear Sampling Method (LSM), which does not require linear scattering assumptions common to most radar techniques and thus may create imagery of fundamentally higher fidelity. The new techniques are formulated in order to overcome the main challenge to practical imaging with the LSM — its need for impractically dense and wide-angle sensor placement. We present several new techniques and demonstrate significantly improved image fidelity from simulated and experimental target data.

**15. SUBJECT TERMS**
Radar, inverse scattering, multistatic, sparsity

| | | | | |
|---|---|---|---|---|
| **16. SECURITY CLASSIFICATION OF:** | | | **17. LIMITATION OF ABSTRACT** | **18. NUMBER OF PAGES** |
| **a. REPORT** | **b. ABSTRACT** | **c. THIS PAGE** | SAR | 84 |
| U/U | U/U | U/U | | |

| | |
|---|---|
| **19a. NAME OF RESPONSIBLE PERSON**<br>Matthew J Burfeindt | **19b. PHONE NUMBER** *(Include area code)*<br>202-404-8696 |

This page intentionally left blank

# CONTENTS

# FIGURES

# SPARSE APERTURE MULTISTATIC RADAR IMAGING TECHNIQUES: FINAL REPORT

## 1. INTRODUCTION

Radiofrequency (RF) imaging is a powerful modality for interrogating the structure of unknown targets due to its all-weather operation as well as its ability to penetrate nonmetallic media. Applications include target identification and recognition (e.g., [1-6]), subsurface detection of mines or other targets (e.g., [7-11]), nondestructive evaluation (e.g., [12,13]), food and grain contamination monitoring (e.g., [14-16]), industrial fluid flow monitoring (e.g., [17-18]), and medical diagnosis or treatment monitoring (e.g.,[19-25]).

Numerous algorithms for forming images from scattered RF fields have been formulated and studied. Most systems in practical use, such as synthetic aperture radar (SAR) systems, use algorithms that assume simplified linear scattering models. The target is assumed to comprise a constellation of discrete point-like scattering centers. The radar wavefront is assumed to propagate directly from the transmitter to each point scatterer and then to reflect and propagate directly back to the receiver with no multiple scattering interactions within the constellation. The received data are focused by backprojecting the received signal to the pixels in the imaging scene by taking into account the direct-path time of flight between each pixel location and each sensor location, or equivalently by leveraging the signal phase modulation that results from the change in target range with sensor motion [26].

This scattering model imperfectly captures the electromagnetic behavior of complex targets. The point scatterer model that best represents the target is generally dependent upon the angle at which the target is viewed, and thus the target appearance in the image may differ drastically across various rotations. Relatedly, the electromagnetic behavior of targets is often better described by scattering surfaces or volumes as opposed to discrete point scatterers when viewed across a sufficiently wide span of angles. In addition, multiple scattering interactions between target features are common, resulting in focused scattering centers in the RF image that are displaced from any particular feature or that lie entirely off the target body. These model imperfections can result in inconsistent fidelity between the focused image and the true target structure, which can present significant challenges for visual interpretation of the image as well as for identification or evaluation of the imaged target.

These challenges motivate the development of imaging techniques that use a more complete electromagnetic model. This document reports the results of a three-year project towards the development of new imaging techniques that overcome the limits of simplified linear scattering assumptions. The project was funded by the Office of Naval Research via the Naval Research Laboratory 6.1 Base Program under the title “Sparse Aperture Multistatic Radar Imaging Techniques.”

The algorithmic framework for the project is the linear sampling method (LSM) [27]. The LSM is a so-called *qualitative* inverse scattering technique that generates an image of the target support by performing a transmit-focusing operation that bypasses the nonlinear nature of the problem without

---

Manuscript approved January 3, 2022.

introducing linear scattering assumptions. In this way, the LSM is generally less computationally expensive and more robust to noise and imperfect propagation assumptions compared to techniques that attempt to solve the nonlinear problem directly via nonlinear optimization (many of these techniques, like the Born iterative method [28], the distorted Born iterative method [29], and contrast source inversion [30], are often referred to as *quantitative* inverse scattering methods, as they involve finding a quantitative estimate of the spatial distribution of electrical properties of the target in order to fully account for the nonlinearity of the problem).

The primary challenge for imaging with the LSM is its need for wide-angle, densely sampled, multistatic transmit and receive apertures (i.e., arrays or synthetic apertures). In many practical imaging scenarios, it may not be possible to achieve the desired sensor spatial and angular diversity for effective LSM imaging due to limitations in resources or data acquisition time. In some cases, there may only be a handful of mobile or stationary sensor platforms available, and thus the desired variety of combinations of transmit and receive locations surrounding the target may not be achievable, resulting in significant artifacts in the LSM imagery. In other cases, there may be constraints on where sensors may be placed. For instance, it may only be possible to illuminate or observe one side of the target. LSM struggles to localize the target and faithfully reconstruct its shape in such limited-aspect scenarios.

In this project, we developed and evaluated new formulations of the LSM for effective imaging in sparse and limited-aspect sensor scenarios. Our overarching strategy was to mitigate the lack of spatial data channels with information gleaned from other domains. We used our knowledge of propagation and electromagnetics to constrain and stabilize the solution of the LSM optimization. We derived the constraints by considering the effects of the LSM solution on the electric fields in the imaging domain using the perspective of the LSM as a focusing problem and the LSM solution as a set of complex weights applied to the transmitters. Interestingly, this required us to consider the behavior of both the magnitude and phase of the LSM solution, whereas most previous work has focused mainly on only the solution magnitude, most likely due to the critical role of the solution magnitude in forming the final LSM image. The fundamentals of the LSM and how they relate to this focusing perspective are briefly discussed in Section 2.

This document is a comprehensive compilation of the work performed across the project. Research output has previously been documented in a series of peer-reviewed journal articles [31, 32], conference proceedings [33-37], and interim reports [38, 39]. These papers and reports are adapted and reported in the remaining sections as follows: Section 3 reports a formulation of the LSM that constrains the phase of the solution to account for the phase delay resulting from propagation of the incident field. Section 4 reports a formulation that constrains the LSM solution to fulfill electric field boundary conditions on the surface of a conducting target. Section 5 reports a formulation for imaging from limited-aspect apertures that combines the phase delay constraint from Section 3 with a receive-beamforming enhancement. Section 6 reports a new machine learning strategy for classifying targets according to their electrical properties using the phase of the LSM solution. Section 7 reports a formulation for a monostatic LSM, wherein the transmitter and receiver are co-located. Finally, concluding statements and suggestions for future work are given in Section 8.

## 2. LSM BACKGROUND

In this section, we briefly review the fundamentals of the LSM. More detailed explanations of implementation of both the conventional LSM as well as our new formulations are given in the following sections.

The imaging scenario is illustrated in Fig. 1, in which an array of transmitters launches an incident electric field at an unknown target, which then reradiates a scattered electric field $\mathbf{E}_\mathrm{S}$ that is observed and

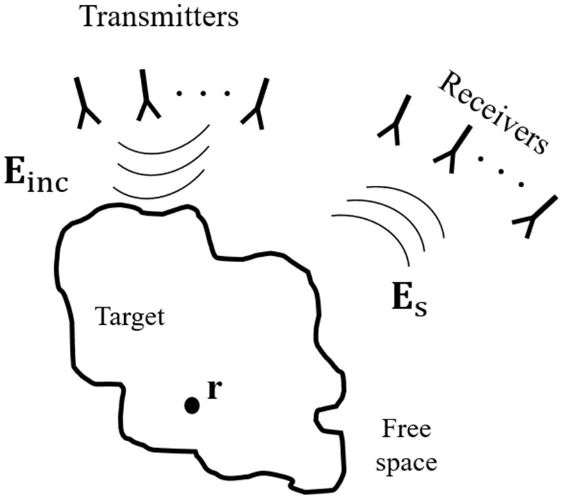

Fig. 1—The imaging scenario, where $\mathbf{E}_{\text{inc}}$ is the incident electric field launched by the transmitters, $\mathbf{E}_{\text{s}}$ is the scattered electric field recorded by the receivers, and **r** is the location of a pixel in the imaging domain

recorded by an array of receivers. Crucially, data is recorded for each individual transmit-receive antenna pair. In radar parlance, the data acquisition is thus multistatic, in that data are collected at multiple receivers for a given transmitter, as well as multiview, in that data are collected across multiple transmitters. In our convention, for a single-frequency data acquisition, $\mathbf{E}_{\text{s}}$ is a matrix wherein the *ij*th element is the scattered electric field phasor resulting from transmitting with the *j*th transmitter and receiving with the *i*th receiver.

The LSM imaging procedure for a pixel location **r** in the imaging domain is to solve for a set of complex weights $\mathbf{g}(\mathbf{r})$ on the transmit antennas that transform $\mathbf{E}_{\text{s}}$ into the pattern observed at the receivers from an elementary current source placed at **r**, denoted $\boldsymbol{\Phi}(\mathbf{r})$. The weights can be found by solving the system of linear equations

$$\mathbf{E}_{\text{s}}\mathbf{g}(\mathbf{r}) = \boldsymbol{\Phi}(\mathbf{r}). \tag{1}$$

The rationale for performing this operation is that the norm of $\mathbf{g}(\mathbf{r})$ will be low if **r** is inside the target and it will be high if **r** is outside the target [27]. Thus, an image of the target can be formed by solving for $\mathbf{g}(\mathbf{r})$ for each **r** in the imaging domain and plotting an indicator function of the solution norm. Indicator functions are commonly of a form similar to

$$I(\mathbf{r}) = \|\mathbf{g}(\mathbf{r})\|^{-1} \tag{2}$$

such that high indicator function values are attained inside the target support and low values are attained outside the target support.

Physical arguments that explain the solution norm behavior have been made in previous work. In [40], the LSM theoretical underpinnings for dielectric targets were analyzed by leveraging the concept of volumetric equivalent currents [41]. In this perspective, the incident field weighted by $\mathbf{g}(\mathbf{r})$ generates a scattered field pattern $\mathbf{E}_{\text{s}}\mathbf{g}(\mathbf{r})$ that is identical to the field that would be generated if the target were replaced by a distribution of equivalent currents within the target support. Assuming **r** is within the target and Eq. (1) is solved successfully, the field is also identical to the field radiated by an elementary current source at **r**, i.e., $\boldsymbol{\Phi}(\mathbf{r})$. The analysis in [40] demonstrated that the low-energy solution to Eq. (1) results in an equivalent current distribution that clusters around **r**. The LSM procedure could thus be said to be focusing the current distribution to approximate the elementary source that generates $\mathbf{\Phi}(\mathbf{r})$. A notional illustration of this behavior is given in Fig. 2.

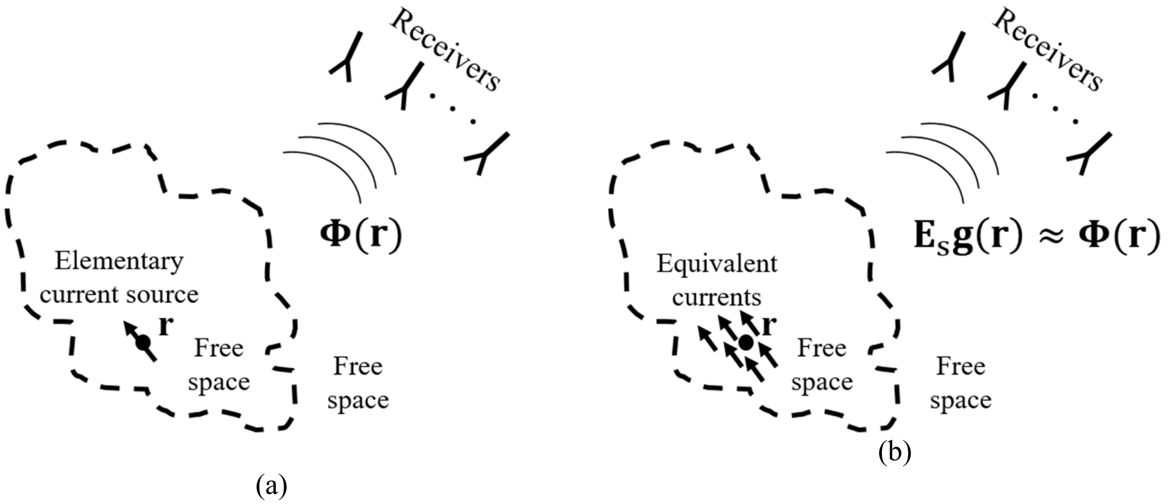

Fig. 2—Notional illustrations demonstrating the principle of LSM as a focusing operation. (a) An elementary current source placed at pixel location **r** that radiates the distribution $\mathbf{\Phi}(\mathbf{r})$ to the receivers. The LSM goal is to choose $\mathbf{g}(\mathbf{r})$ such that the target re-radiates the same field. (b) Successfully solving (1) results in a $\mathbf{g}(\mathbf{r})$-weighted incident field that produces an equivalent current distribution clustering around **r**. The focused equivalent current distribution radiates the weighted field $\mathbf{E}_S\mathbf{g}(\mathbf{r})$ which matches the elementary field pattern $\mathbf{\Phi}(\mathbf{r})$.

Conversely, if **r** is outside the target support, there is no target material surrounding **r** with which to form equivalent currents, and thus the low-energy solution is not available. The difference in energy in the solution for **r** inside and outside the target thus explains the corresponding behavior of the norm of $\mathbf{g}(\mathbf{r})$. Corresponding physical arguments for conducting targets could be made by considering equivalent surface currents on the target boundary via Huygens's principle, as in [42]. In summary, and loosely speaking, the target can only be induced to *efficiently* re-radiate an elementary pattern centered on **r** if there is target material surrounding **r** with which to form the required volume or surface current distribution.

The above description briefly highlights the perspective of the LSM as a transmit focusing problem. In the following sections, we leverage intuition based on this perspective to generate new formulations of the LSM for challenging sparse-aperture and limited-aspect sensing scenarios.

## 3. PHASE-DELAY FREQUENCY VARIATION LSM WITH A MULTIPOLE ENHANCEMENT

This section is adapted from a journal article published in *IEEE Transactions on Antennas and Propagation* [31]. It builds upon preliminary work published in conference proceedings [33] and subsequently captured in an interim report for the project [38].

### 3.1 Background

In LSM imaging, a lack of transmitters or receivers may, in principle, be mitigated to some extent using synthetic aperture data collection approaches. For instance, a data collection with sparsity in receive directions and density in transmit directions could be achieved using a handful of stationary receivers and a single mobile transmit platform that translates around the imaging region and radiates a pulse at each desired transmit location. However, achieving sufficient multistatic density (i.e., collecting data for all desired transmit-receive location pairs) using synthetic aperture approaches for both transmit and receive apertures may be too time-consuming or too challenging to coordinate between multiple moving platforms.

LSM imaging performance in some cases may be improved through the use of multifrequency data. Multifrequency LSM is typically implemented by computing the solution at each individual frequency and then summing the resulting solution norms. If the solution norms for target pixels are more consistent across frequency than the solution norms for artifact pixels, then the sum across frequency results in a larger image contrast between target and non-target space, resulting in a more faithful representation of target support. However, in sparse aperture scenarios, imaging artifacts for different frequencies will often appear at similar image locations, thereby limiting the improvement from multifrequency operation. Alternate formulations for multifrequency LSM are thus desired for sparse aperture imaging.

In this section, we present a formulation of the multifrequency LSM for improving imaging performance in scenarios where either the transmit or receive apertures are sparse by placing a constraint on the phase of the LSM across frequencies according to a priori propagation assumptions. The phase constraint links the solutions at each frequency according to the electrical path length traversed by the incident wave as it travels from the transmitters to the pixel of interest. The constraint is implemented as a penalty on variations from the desired phase behavior across frequency. The rationale for relying on the phase of the incident wave lies in the perspective of the LSM as a problem of focusing the target equivalent currents at the pixel of interest [40]. Image artifacts that do not evince the correct position- and frequency-dependent phase behavior are suppressed, leading to higher-fidelity image results.

There has been little interest paid to date to the phase behavior of the LSM across frequency, perhaps because the final LSM image typically is formed by displaying only the norm of the solution for each pixel. We hypothesize that the phase of the LSM solution also contains valuable information about the imaging scene scattering environment that can help mitigate a lack of spatial information from sparse data collections.

Previous work has shown that LSM imaging performance can be improved for sparse-aperture data by making use of an iterative $L_1$ minimization on overall changes in the LSM solution with frequency [43]. The rationale for this work is that changes in the amplitude of the solution across frequency are expected to be small outside the vicinity of a sparse set of target-dependent resonant frequencies. The work we present here is distinct in that we use a frequency variation formulation not primarily to penalize changes in the solution across frequency, but instead to leverage previously unused propagation-based information embedded in the phase of the LSM solution. This approach has the additional benefit in that it lends itself to a noniterative L2 minimization scheme, as the phase changes across frequency are not expected to be sparse.

We have previously reported preliminary imaging results for the proposed phase-delay frequency variation (PDFV) formulation of the LSM in conference proceedings [33]. In this report, we present a more comprehensive investigation, including an enhancement of the technique making use of multipole electric fields that improves performance for non-convex and high-contrast targets, an investigation into the proper choice of regularization parameters, imaging results from a wider variety of scenarios, including high-contrast targets, and an experimental imaging example.

## 3.2 Imaging Formulation

### *3.2.1 Standard LSM Formulation*

Let $V$ denote the support of a target to be interrogated. Surrounding $V$ are a total of $N_{\text{tx}}$ transmitters and $N_{\text{rec}}$ receivers. Each transmitter sequentially transmits an incident field and the resulting scattered field phasors observed at the receivers at wavenumber $k$ are collected in an $N_{\text{rec}} \times N_{\text{tx}}$ matrix $\mathbf{E}_{\text{s}}(k)$. We assume a two-dimensional transverse magnetic scenario, and thus the elements of $\mathbf{E}_{\text{s}}(k)$ are assumed to be complex scalars. Extension of the technique to multiple polarizations is straightforward, but we neglect this perspective for ease of explication.

For a pixel location $\mathbf{r}$ in the imaging scene, let $\mathbf{\Phi}(k,\mathbf{r})$ be an $N_{\text{rec}} \times 1$ vector of the Green's functions between each receiver location and $\mathbf{r}$. The LSM solution at $\mathbf{r}$ and $k$ is found by solving the following system of equations for the unknown $N_{\text{tx}} \times 1$ vector $\mathbf{g}(k,\mathbf{r})$:

$$\mathbf{E}_{\text{s}}(k)\mathbf{g}(k,\mathbf{r}) = \mathbf{\Phi}(k,\mathbf{r}), \tag{3}$$

A scheme such as Tikhonov regularization is typically used to find a stable solution to Eq. (3). The problem Eq. (3) can be seen as finding beamforming weight vector $\mathbf{g}(k,\mathbf{r})$ acting on the transmitters in order to achieve field distribution $\mathbf{\Phi}(k,\mathbf{r})$ at the receivers, given knowledge of the measured transfer responses between transmitters and receiver given by $\mathbf{E}_{\text{s}}(k)$. In this study, we use the two-dimensional free-space Green's function $\mathbf{\Phi}(k,\mathbf{r}) = H_0^2\big(k\mathbf{d}_{\text{rec}}(\mathbf{r})\big)$, where $\mathbf{d}_{\text{rec}}(\mathbf{r})$ is the $N_{\text{rec}} \times 1$ vector of distances from $\mathbf{r}$ to each receiver and $H_0^2$ denotes the zeroth-order Hankel function of the second kind.

The multifrequency indicator function $I(\mathbf{r})$ is then typically calculated as

$$I(\mathbf{r}) = \sum_k \|\mathbf{g}(k,\mathbf{r})\|^{-1}, \tag{4}$$

where the summation is over all observed $k$, and the norm is $L_2$. In a dense-aperture data collection scenario, the norms in Eq. (4) will be bounded for $\mathbf{r}$ inside $V$ and unbounded for $\mathbf{r}$ outside $V$ [27], and thus an image of the target support can be created by displaying $I(\mathbf{r})$ for all $\mathbf{r}$ in the scene to be imaged.

### *3.2.2 PDFV-LSM Rationale*

Our strategy for enhancing the LSM for sparse aperture imaging is to use *a priori* assumptions on the phase of $\mathbf{g}(k,\mathbf{r})$ to improve imaging performance. Specifically, we constrain the change in phase of $\mathbf{g}(k,\mathbf{r})$ across frequency according to the frequency-dependent change in electrical path length.

In the following description, we assume a dense-transmitter, sparse-receiver data set. However, the proposed technique may also be applied to sparse-transmitter, dense-receiver datasets using the principle of reciprocity.

Our rationale for our proposed approach is based on the perspective of the LSM as a focusing problem. In [40], Catapano *et al* showed that the low-energy solution to Eq. (3) leads to a clustering or focusing around $\mathbf{r}$ of the equivalent currents induced in the target by the incident field. We therefore assume in our formulation that a faithful reconstruction of target support via Eq. (3) requires a focused equivalent current at **r**, and that this is analogous to achieving a focused incident field at **r**. The latter assumption is reasonable for small contrasts between the target and the background medium under the Born approximation

Let the Born-approximated equivalent current induced at location **r**' by the LSM weight vector designed for focus location **r** be given by $J_{\mathrm{eq}}(k,\mathbf{r}') \propto \chi\mathbf{E}_i(k,\mathbf{r}')\mathbf{g}(k,\mathbf{r})$, where $\chi$ is the contrast and $\mathbf{E}_i(k,\mathbf{r}')$ is the $N_{\mathrm{tx}} \times 1$ vector of the unweighted incident fields from each transmitter. If Eq. (3) is satisfied, then $J_{\mathrm{eq}}(k,\mathbf{r}')$ is focused at **r**, according to the above discussion.

Let $\Delta k$ be a small step in wavenumber. Under far-field and homogeneous background conditions, we can write $\mathbf{E}_i(k+\Delta k,\mathbf{r}) \approx \mathbf{E}_i(k,\mathbf{r}) \odot \exp(-j\Delta k\mathbf{d}_{\mathrm{tx}}(\mathbf{r}))$, where '$\odot$' refers to elementwise multiplication and $\mathbf{d}_{\mathrm{tx}}$ is the $N_{\mathrm{tx}} \times 1$ vector of distances between each transmitter and **r**. To maintain the focus of the incident field at the incremented frequency, we assume the LSM weight vector must be modulated to coherently compensate for the phase change. Accordingly, we write our desired phase relationship for the LSM weight vector at adjacent frequency samples as

$$\mathbf{g}(k+\Delta k,\mathbf{r}) \approx \mathbf{g}(k,\mathbf{r}) \odot \exp(j\Delta k\mathbf{d}_{\mathrm{tx}}(\mathbf{r})). \tag{5}$$

In the following subsection, we describe how we implement this constraint into the LSM.

### *3.2.3 PDFV-LSM Implementation*

The proposed PDFV formulation of the LSM is defined by the following minimization problem at every **r** in the scene to be imaged:

$$\min_{\mathbf{g}(k,\mathbf{r})} \sum_k \left\| \mathbf{E}(k)\mathbf{g}(k,\mathbf{r}) - \frac{\boldsymbol{\Phi}(k,\mathbf{r})}{\|\boldsymbol{\Phi}(k,\mathbf{r})\|} \right\|^2 + \alpha\|\mathbf{g}(k,\mathbf{r})\|^2 + \beta\|D(k,\mathbf{r})\|^2, \tag{6}$$

where

$$D(k,\mathbf{r}) = \mathbf{g}(k,\mathbf{r}) - \mathbf{g}(k+\Delta k,\mathbf{r}) \odot \exp\big(j\Delta k\mathbf{d}_{\mathrm{tx}}(\mathbf{r})\big). \tag{7}$$

The first two normed expressions in Eq. (6) constitute a version of the standard Tikhonov-regularized LSM, while the third term constitutes the PDFV penalty that enforces the desired phase relationship in Eq. (5). The parameters $\alpha$ and $\beta$ are used to regularize the solution to the ill-posed problem, the former of which scales the penalty for large-norm solutions and the latter of which scales the penalty for deviations from the desired propagation-based solution phase. A strategy for choosing $\alpha$ and $\beta$ effectively is explored later in this section.

The standard LSM makes no linearizing assumptions in its formulation. Including the PDFV penalty term in Eq. (6) could therefore be seen as a compromise to make up for the lack of spatial data in a sparse-aperture scenario, as the rationale for the PDFV-LSM makes use of the Born approximation. We explore the performance of the PDFV-LSM for high-contrast targets, for which the Born approximation does not apply, later in this section.

In Eq. (6), the vector $\boldsymbol{\Phi}(k,\mathbf{r})$is scaled by its norm. Scaling the right-hand side of the LSM equation is an approach that has been used in previous work in order to improve imaging performance in limited-aspect scenarios, such as in ground-penetrating radar applications [7]. We have found that using this strategy in sparse-aperture scenarios is likewise beneficial to image quality, and thus employ it for the examples in this study. Calculation of Eq. (6) may be performed using a block-matrix implementation similar to the one used in [43], in the following form,

$$\min_{\mathbf{x}(\mathbf{r})} ||\mathbf{A}(\mathbf{r})\mathbf{x}(\mathbf{r}) - \mathbf{b}(\mathbf{r})||^2, \tag{8}$$

where

$$\mathbf{A}(\mathbf{r}) = \begin{bmatrix} \bar{\bar{\mathbf{E}}}_s \\ \sqrt{\alpha}\mathbf{I} \\ \sqrt{\beta}\mathbf{D}(\mathbf{r}) \end{bmatrix} \quad \mathbf{x}(\mathbf{r}) = \begin{bmatrix} \mathbf{g}(k_1, \mathbf{r}) \\ \vdots \\ \mathbf{g}(k_F, \mathbf{r}) \end{bmatrix} \tag{9}$$

$$\mathbf{b}(\mathbf{r}) = \begin{bmatrix} \mathbf{\Phi}(k_1, \mathbf{r})/||\mathbf{\Phi}(k_1, \mathbf{r})|| \\ \vdots \\ \mathbf{\Phi}(k_F, \mathbf{r})/||\mathbf{\Phi}(k_F, \mathbf{r})|| \\ \mathbf{0} \end{bmatrix}$$

In Eq. (9), $k_1 \dots k_F$ refers to the first through the $F$th sampled frequencies, $\mathbf{I}$ is the $N_{\text{tx}}F \times N_{\text{tx}}F$ identity matrix, and $\mathbf{0}$ is a vector of zeros of size $N_{\text{tx}}(2F-1) \times 1$. The matrix $\mathbf{D}(\mathbf{r})$ is of size $N_{\text{tx}}(F-1) \times N_{\text{tx}}F$ and incorporates the penalty term Eq. (7) into the optimization. The main diagonal of $\mathbf{D}(\mathbf{r})$ is filled with ones, and the $N_{\text{tx}}$-diagonal is defined by the concatenation of $F-1$ copies of the vector $-\exp(j\Delta k \mathbf{d}_{\text{tx}}(\mathbf{r}))$. All other elements of $\mathbf{D}(\mathbf{r})$ are zero.

Lastly, the block-diagonal matrix $\bar{\bar{\mathbf{E}}}_\text{s}$ is of size $N_{\text{rec}}F \times N_{\text{tx}}F$ and is given by

$$\bar{\bar{\mathbf{E}}}_\text{s} = \begin{bmatrix} \mathbf{E}_\text{s}(k_1) & 0 & \dots \\ 0 & \ddots & \dots \\ \vdots & \dots & \mathbf{E}_s(k_F) \end{bmatrix}. \tag{10}$$

### 3.2.4 *Multipole Enhancement to the PDFV-LSM*

A well-known property of the single-frequency LSM is its tendency to struggle to reconstruct the support of non-convex targets [44, 45]. Voids or cavities in such targets are often indistinguishable from the target support in the LSM imagery. The use of multiple frequencies can mitigate this weakness, leading to more faithful image results.

However, sparse-aperture LSM will often struggle to reconstruct non-convex or resonant targets even if multiple frequencies are used. As will be seen, the PDFV-LSM will also sometimes fail to reconstruct such features, even if it significantly improves overall imaging performance compared to the standard LSM. The imperfection of the PDFV-LSM in these instances could be caused by the general weakness of various LSM approaches for non-convex features.

We make use of a multipole enhancement to the LSM to overcome challenging target imaging scenarios. Multipole formulations of the LSM have been investigated previously for enhancing non-convex features in LSM imagery [45, 46]. Here, we adapt the formulation of Crocco et al [45]. In this formulation, an LSM solution to Eq. (3) is found for multiple right-hand sides denoted $\mathbf{\Phi}_p^x(k, \mathbf{r})$ and $\mathbf{\Phi}_p^y(k, \mathbf{r})$ for $p = 1, \dots, P$, where

$$\begin{aligned}\mathbf{\Phi}_p^x(k,\mathbf{r}) &= H_p^2(k\mathbf{d}_{\mathrm{rec}}(\mathbf{r}))\cos\big(p\boldsymbol{\theta}(\mathbf{r})\big)\\ \mathbf{\Phi}_p^y(k,\mathbf{r}) &= H_p^2(k\mathbf{d}_{\mathrm{rec}}(\mathbf{r}))\sin(p\boldsymbol{\theta}(\mathbf{r}))\ .\end{aligned} \tag{11}$$

In Eq. (11), $\boldsymbol{\theta}(\mathbf{r})$ is a vector of azimuthal angles between **r** and each receiver location. Each term in Eq. (11) corresponds to a term in the multipole decomposition of the scattered field.

Crocco et al showed that for $p > 0$, the equivalent current distribution is roughly annular in shape, with larger $p$ corresponding to larger inner radii for the annulus. If **r** is at the location of a void in the target, the lowest-energy solution to Eq. (3) will correspond to the order $p$ that produces the annular current that is closest to the dimension of the void. A combined indicator function can therefore be defined to take advantage of this behavior to enhance the appearance of voids in the target image.

We define our combined indicator function as a modification of the indicator from [45], given by

$$I_{\mathrm{MP}}(\mathbf{r}) = a_0 I(\mathbf{r}) + \sum_{p=1}^{P} a_p I_p(\mathbf{r})\ , \tag{12}$$

where $I(\mathbf{r})$ is defined as in Eq. (4), $a_0, \dots, a_P$ are constants that normalize each term according to its maximum value across all **r** in the imaging scene, and

$$I_p(\mathbf{r}) = \frac{\left(\sum_k \|\mathbf{g}(k,\mathbf{r})\|^{-1}\right)^2}{\left(\sum_k \|\mathbf{g}_p^x(k,\mathbf{r})\|^{-1}\right)\left(\sum_k \left\|\mathbf{g}_p^y(k,\mathbf{r})\right\|^{-1}\right)}\ . \tag{13}$$

In Eq. (13), $\mathbf{g}_p^x(k,\mathbf{r})$ and $\mathbf{g}_p^y(k,\mathbf{r})$ refer to the solutions to Eq. (6) wherein $\mathbf{\Phi}(k,\mathbf{r})$ has been replaced with the corresponding multipole term from Eq. (11).

The indicator function used here is similar to the one defined in [45], but differs in the use of the normalization constants and the use of a sum instead of a product in Eq. (12). We make these changes to prevent sparse-aperture-caused artifacts in any single multipole term from dominating the contributions to the indicator function from the rest of the multipole terms.

In the remainder of this section, we will explore the effectiveness of the PDFV-LSM by applying it to simulated and experimental data. We will first describe the data acquisitions in the following subsection.

### 3.3 Data Acquisitions

#### *3.3.1 Simulated Data*

We acquire simulated data using the finite-difference time-domain (FDTD) method for two-dimensional scattering scenes. The scattered field data are recorded in the time domain for each transmitter-receiver pair and then transformed to frequency-domain phasors using discrete Fourier transforms. The data are collected across 51 uniformly spaced frequencies between 100 and 500 MHz. In the remainder of this paper, we will refer to the wavelength at the center of the frequency band as $\lambda_c$. The background material for the simulations is free space.

We place transmit and receive locations on a ring of radius $6\lambda_c$. We use a total of $N_{\mathrm{tx}} = 45$ uniformly spaced transmit locations, at which we launch incident electric fields using elementary current sources. This choice of transmitter density satisfies the spatial Nyquist criterion $N_{\mathrm{tx}} > 2k_{\max}a$ as described in [44] for the maximum wavenumber in the recorded bandwidth and a modestly overestimated maximum target extent from scene center of $a = 2\lambda_c$. We collect scattered fields at 360 uniformly spaced receive locations. We then generate numerous sparse-receiver datasets by selecting subsets of the receive data for $N_{\text{rec}}$ ranging from 2 to 6. Prior to imaging each sparse-aperture subset, we add Gaussian white noise to the data such that the total signal-to-noise ratio (SNR) across all $N_{\text{rec}} \times N_{\text{tx}} \times F$ phasor samples is 40 dB.

We generate dense-transmitter, sparse-receiver data in this manner using three example target supports placed at the center of the ring of transmit and receive locations, illustrated in Fig. 3. The first target is in the form of an L, the second is in the form of a U, and the third is a version of the well-known Austria profile. We generate data for two target materials. The first target material is lossless and has a dielectric constant of 2. The second is perfect electric conductor (PEC).

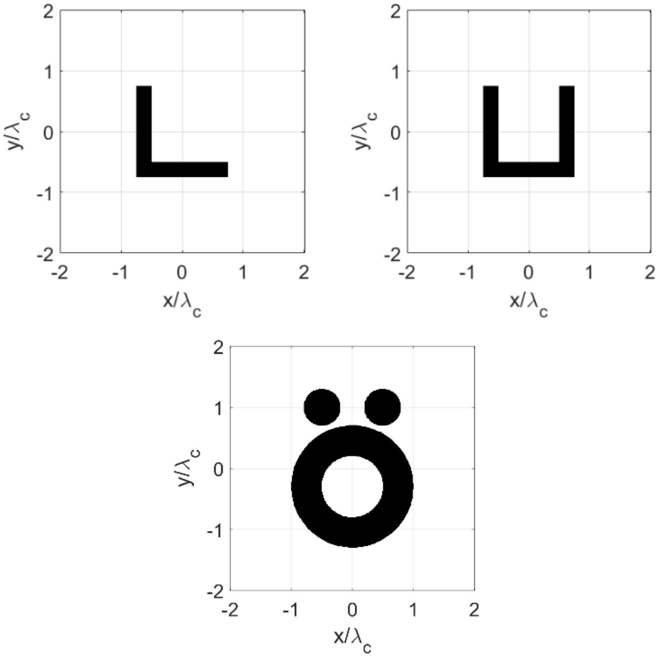

Fig. 3—The supports for the targets used for simulated data acquisitions in this section

### 3.3.2 Experimental Data

We also make use of an experimental dataset provided by the University of Wisconsin Computational Electromagnetics Laboratory that was generated using the layout given in the diagram in Fig. 4. Eight 3.5-cm-long monopole wire antennas were mounted on a brass ground plane around a ring of radius 10 cm. A paraffin wax cylinder of diameter 6.5 cm and height 8.5 cm was placed in the interior of the antenna ring offset from center by 4 cm. An Agilent E8364 vector network analyzer (VNA) was used to collect frequency domain data for all 64 transmit-receive antenna pairs. For every measurement, the VNA's two ports were connected to the feeds of the active antenna pair, which were located underneath the brass plate, and every other antenna feed was terminated with a 50 Ω load. Data were collected in 5 MHz increments starting at 500 MHz. We selected data up to 2000 MHz, resulting in 301 total frequencies, in order to again satisfy the spatial Nyquist criterion on transmit, $N_{\text{tx}} > 2k_{\max}a$, for a modestly overestimated target extent from scene center $a = 9.5$ cm. As with the simulated data described in the previous subsection, we generate various sparse-receiver examples from this data by selecting subsets of the $8 \times 8$ collected signal phasors at each frequency.

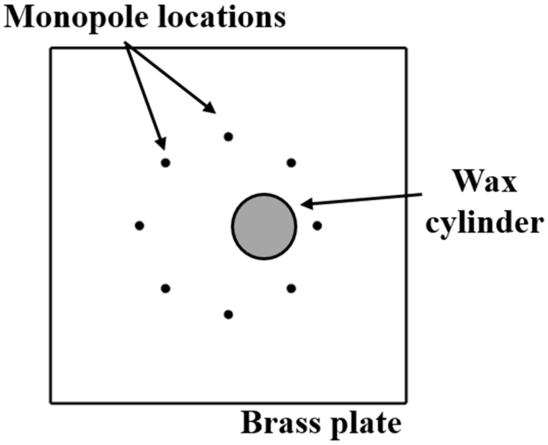

Fig. 4—A diagram of the experimental data acquisition

## 3.4 Results and Discussion

### *3.4.1 Regularization Parameter Selection*

Finding a solution to Eq. (6) that results in a faithful reconstruction of the target shape requires appropriate choice of regularization parameters $\alpha$ and $\beta$. We choose these parameters using a heuristic strategy inspired by the well-known L-curve concept [47].

As will be seen, a poorly regularized PDFV-LSM solution for sparse-aperture data acquisitions will often result in large values for the LSM indicator function throughout the image. This phenomenon can be captured quantitatively by measuring the norm of the LSM image across a selection of pixels. Conversely, a regularization choice that results in a small image norm will typically result in a large residual norm, expressed as $\sqrt{\sum_k \left\| \mathbf{E}_s(k)\mathbf{g}(k,\mathbf{r}) - \mathbf{\Phi}(k,\mathbf{r})/\|\mathbf{\Phi}(k,\mathbf{r})\| \right\|^2}$, which indicates that the solution is a poor fit for the data.

Our strategy is to use the L-curve concept to find a compromise between these two effects. Our approach differs somewhat from the conventional L-curve strategy for ill-posed problems, in which a compromise is found between the residual norm and the norm of the solution to the ill-posed problem, in this case $\mathbf{g}(k,\mathbf{r})$, which has a reciprocal relationship with the image norm for the LSM by Eq. (4). However, as will be seen, focusing on the image norm instead captures the regularized behavior of the sparse-aperture PDFV-LSM well across pixels in the image.

We demonstrate our regularization strategy using scattered field data from the dielectric L shape from Fig. 3. We select an example sparse receiver subset with $N_{\text{rec}} = 4$ using receiver azimuth locations $[0°, 85°, 95°, 180°]$, measured counterclockwise from the $+x$-axis.

We then define a coarsely sampled set of imaging scene pixels, in this case a $5 \times 5$ grid of pixels in the domain $x, y \in \lambda_c[-2,2]$. We then compute the PDFV-LSM solution for each pixel across a two-dimensional parameter sweep in $\alpha$ and $\beta$. In this example, we do not employ the multipole enhancement for simplicity. We compute solutions for four candidate $\alpha$ values running from $10^{-7}$ to $10^{-4}$ on a logarithmic scale, and eight $\beta$ values running from $10^1\alpha$ to $10^8\alpha$ for each $\alpha$, also on a logarithmic scale.

We then plot the resulting image norms against the residual norms, as given in Fig. 5(a). As can be seen, distinct L-curves can be formed by connecting the points corresponding to each candidate $\alpha$. The knees of the curves, representing the best tradeoff between image and residual norms, occurs for parameter ratios $\beta/\alpha$ between approximately $10^3$ and $10^5$.

We then plot a second curve in Fig. 5(b) that relates $\beta$ to the image norm while keeping the parameter ratio constant at a ratio in the vicinity of the identified L-curve knee, in this case $10^5$. As shown in Fig. 5(b), this results in a curve with an inflection point in the vicinity of $\log\beta = -1$ between large- and small-norm images.

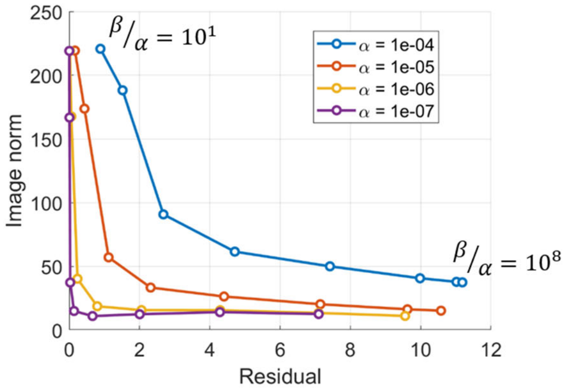

(a)

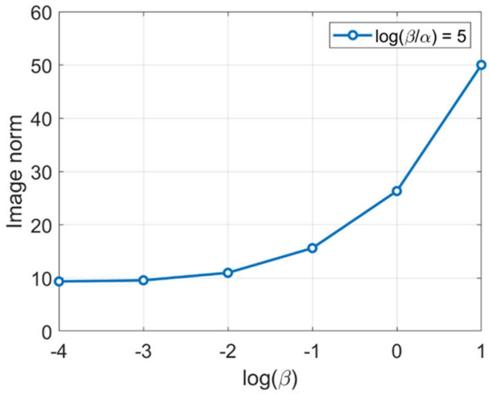

(b)

Fig. 5—(a) L-curves for choosing the ratio $\beta/\alpha$ for a imaging the dielectric L-shaped target with $N_{\text{rec}} = 4$. (b) A curve for choosing $\beta$ based on the behavior of the image norm while keeping the ratio $\beta/\alpha$ constant.

We propose the following heuristic for choosing the PDFV-LSM regularization from these two curves: First, the ratio $\beta/\alpha$ should be chosen in the vicinity of the knee of the L-curve to balance the residual norm and image norms. Second, keeping this ratio constant, $\beta$ should be chosen as large as possible in order to emphasize the desired propagation-based phase behavior via the PDFV constraint in Eq. (6) while not passing into a regime of large image norms, which signify poor solutions.

We now evaluate the effectiveness of this heuristic empirically by considering reconstructed image quality as a function of regularization parameter choice. We form PDFV-LSM images for the same $N_{\text{rec}} = 4$ case on a finer $35 \times 35$ grid of pixels using a variety of choices for $\alpha$ and $\beta$. We assess the quality of each image by finding the pixels that obey the following threshold, defined as in [46]:

$$\log I(\mathbf{r}) > \min \log I(\mathbf{r}) + \gamma(\max \log I(\mathbf{r}) - \min \log I(\mathbf{r})). \tag{14}$$

We set the threshold parameter to $\gamma = 0.5$. We then report the following error metric:

$$\text{Error} = \frac{\text{Number of misclassified pixels}}{\text{Total number of pixels in image}}. \tag{15}$$

In Eq. (15), a misclassified pixel is either a pixel that exceeds the threshold in Eq. (14) despite being outside the target support, or a pixel that is below the threshold while being inside the target support.

The error metric is plotted against the regularization parameters in Fig. 6. Each data point represents the mean error across five trials with different random noise instances. The error for the standard LSM images (i.e., $\beta = 0$) is shown in Fig. 6(a) across a wide range of $\alpha$. The error is consistently high across all choices of $\alpha$, with the exception at $\log \alpha = 0$, where it dips to a somewhat lower value.

In Fig. 6(b), the error metric is plotted against various $\beta$ while keeping constant $\log \alpha = -6$. Results are shown for both the PDFV and a frequency variation (FV) implementation. The FV implementation is similar to the PDFV implementation, with the exception that the $N_{\text{tx}}$-diagonal of $\mathbf{D}$ from Eq. (9) is set to -1 instead of the phase-delay-based complex exponential. Evaluating the FV results against the PDFV results allows us to determine the degree to which imaging improvement achieved by the PDFV is due to penalties on deviation from the desired solution phase relationship, as opposed to penalties on overall changes in $\mathbf{g}(k, \mathbf{r})$ across frequency.

The results in Fig. 6(b) show that the PDFV error decreases as $\beta$ becomes larger than $\alpha$. The error reaches its lowest value of below 0.10 at $\log \beta = -1$, and then begins to increase for larger $\beta$. This behavior is consistent with the proposed L-curve-based heuristic, as the best reconstruction occurs for $\beta/\alpha$ near the knee of the L-curve in Fig. 5(a), and performance degrades as $\beta$ is increased past the inflection point shown in Fig. 5(b). The results in Fig. 6(b) also show that the FV error is consistently worse than the PDFV error and is above 0.25 for all choices of $\beta$, signifying that enforcing the proposed phase relationship across frequency leads to imaging improvements.

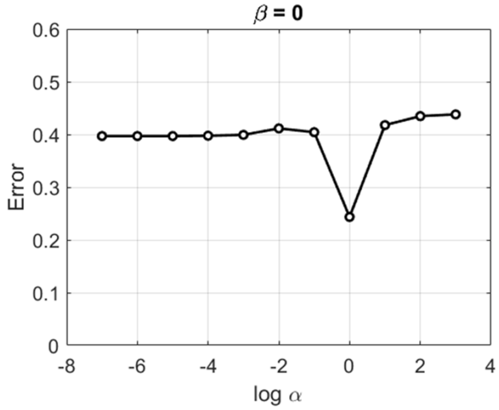

(a)

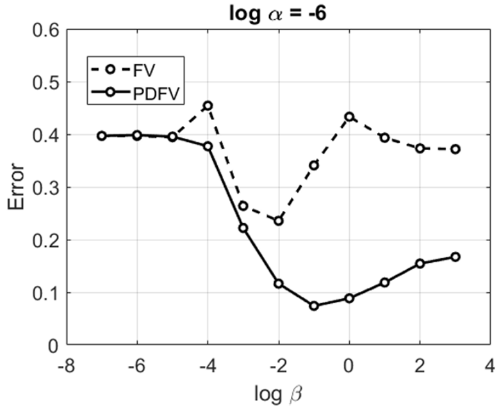

(b)

Fig. 6—Reconstruction error metrics of Eq. (15) as a function of regularization parameters.
(a) Standard LSM image error vs $\alpha$. (b) FV and PDFV images error vs $\beta$ for constant $\alpha$.

Next, we present example image results for the standard, FV, and PDFV techniques. We display $20\log I(\mathbf{r})$ scaled such that 0 dB is set to the pixel of highest value in each image. In each case, and for all following images in this paper, the dynamic range of the color bar is determined by the maximum and minimum values of the indicator function.

Fig. 7(a) shows image results for the standard LSM using the $\alpha$ corresponding to the lowest measured error in Fig. 6(a), i.e., $\log\alpha = 0$. The standard LSM completely fails to reconstruct the target support in the sparse-aperture scenario, as expected. Likewise, Fig. 7b shows an FV-LSM image using regularization parameters of lowest error as given by Fig. 6(b), i.e., $\log\alpha = -6\,, \log\beta = -2$. There is some resemblance to the target shape in the reconstructed region in the center of the image. However, there are also large artifacts in the surrounding regions that obscure the true shape of the target.

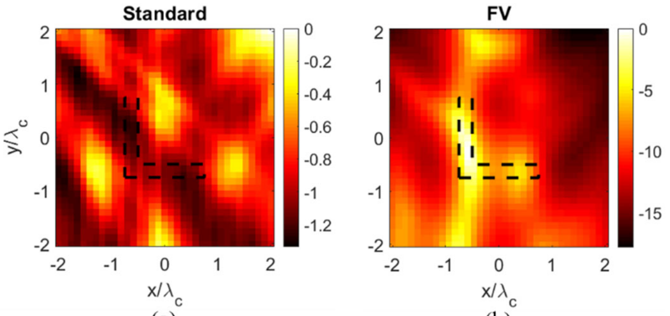

(a) (b)

Fig. 7—(a) Standard LSM reconstruction with $\log\alpha = 0$, (b) FV-LSM reconstruction with $\log\alpha = -6,\ \log\beta = -2$. The receiver angular positions are given by $[0°, 85°, 95°, 180°]$.

Fig. 8 shows PDFV-LSM image results for constant $\log\alpha = -6$ and various $\beta$. Using $\log\beta = -1$, as suggested by the previously described analysis, results in a very high-fidelity image, in that the target shape is well represented by the LSM imagery near the center of the scene and artifacts are minimal. Conversely, using a $\beta$ that does not correspond to an L-curve knee from Fig. 5(a) results in degraded imagery. Choosing $\beta$ too low, i.e., $\beta = 0$ (which is equivalent to the standard LSM) or $\log\beta = -4$, results in imagery with nearly no fidelity to the true target support, and choosing $\beta$ too high, i.e., $\log\beta = 2$, results in numerous image artifacts.

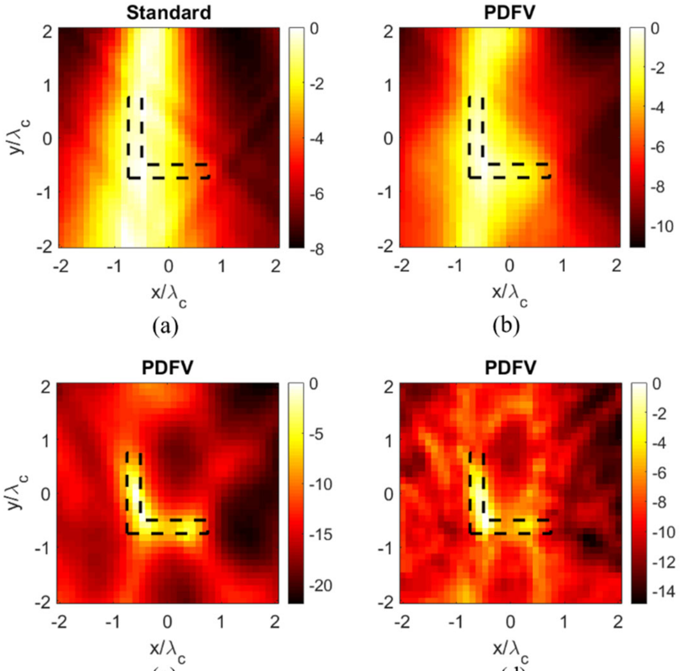

(a) (b)

(c) (d)

Fig. 8—PDFV-LSM image results with $\log\alpha = -6$ and (a) $\beta = 0$, which is equivalent to the standard LSM, (b) $\log\beta = -4$, (c) $\log\beta = -1$, (d) $\log\beta = 2$. The receiver angular positions are given by $[0°, 85°, 95°, 180°]$.

The results in this subsection suggest that incorporating *a priori* propagation information into the LSM reconstruction via the PDFV constraint mitigates the lack of spatial data in a sparse-aperture data collection if the regularization parameters are chosen properly. We explore PDFV-LSM performance across a larger variety of scenarios in the remainder of this section.

### *3.4.2 Effects of Multipole Enhancement*

In this subsection, we apply the multipole-enhanced version of the PDFV-LSM to the simulated data and evaluate imaging performance. We choose imaging scenarios that are expected to challenge the PDFV-LSM, due to either high-contrast electrical properties (in which the Born approximation inherent in the focusing rationale for the PDFV does not apply), a strongly non-convex target shape in the form of the U-shaped target, or a target shape with other nonlinear scattering interactions in the form of the "Austria" profile.

In the following examples, we again use $\log\alpha = -6, \log\beta = -1$. We use $P = 2$ multipole terms. We have found that using more than 2 multipole terms for the targets in this example makes very little change in the resulting imagery.

We first consider the PEC L-shaped target. Fig. 9 shows imaging results for the standard, multipole standard, PDFV, and multipole PDFV version of the LSM for a receiver set defined by angles $[0°, 15°, 180°, 345°]$. Both the standard and multipole standard imaging results bear little resemblance to the true target profile. The PDFV image shows some improvement in that the region of high $I(\mathbf{r})$ somewhat corresponds to the location and shape of the target. However, there is a lack of target detail, and the non-convex nature of the target is not apparent. The multipole LSM image, in comparison, displays much better fidelity to the true target shape.

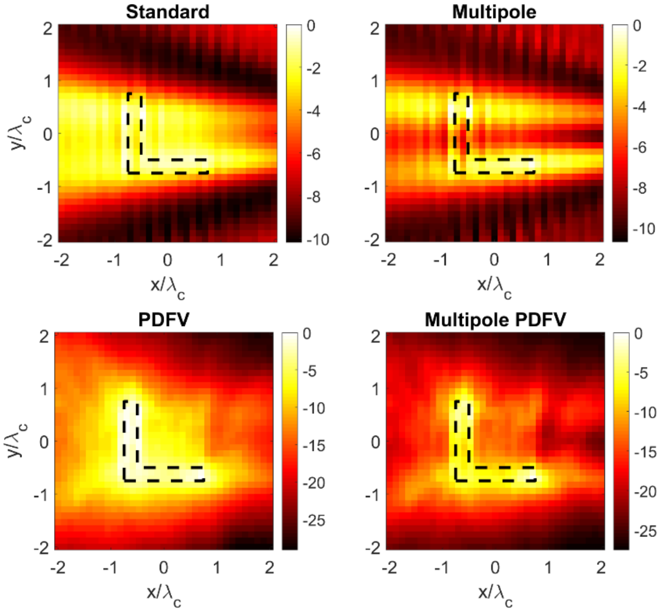

Fig. 9—Imaging results for the various LSM formulations for the PEC L-shaped target using receiver angles $[0°, 15°, 180°, 345°]$

Notably, the addition of the multipole enhancement appears to not only help recover the non-convex nature of the target, but also to improve recovery of the convex portions of the target shape. This can be seen on the leftmost target boundary, where the transition from high to low indicator function values is much closer to the true target boundary in the multipole PDFV results as compared to the PDFV results without the multipole enhancement. The PDFV-LSM may struggle to recover the true target dimension in this example due to the high-contrast nature of the target, which violates the Born approximation that is used in the rationale of the PDFV as described in Section 3.2.2. The multipole enhancement to the PDFV may help to mitigate this challenge by providing additional diversity in scattering information.

Next, we consider imagery for the dielectric and PEC U-shaped targets in Fig. 10 and Fig. 11, respectively, using receiver angles $[0°, 255°, 270°, 285°]$. The results display behavior similar to Fig. 9. The standard and multipole results fail to represent the true shape of the target, while the PDFV results fail to include the target cavity. The multipole PDFV results are the best in both cases, with the cavity in the target clearly visible. Similarly to Fig. 9, the multipole enhancement for the PEC target in Fig. 11 improves reconstruction of the overall target dimensions as well as its shape.

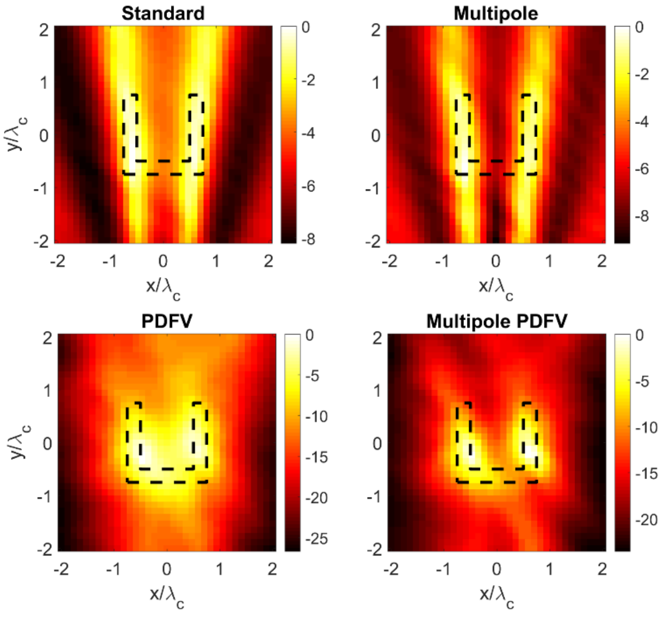

Fig. 10—Imaging results for the various LSM formulations for the dielectric U-shaped target using receiver angles $[0°, 255°, 270°, 285°]$

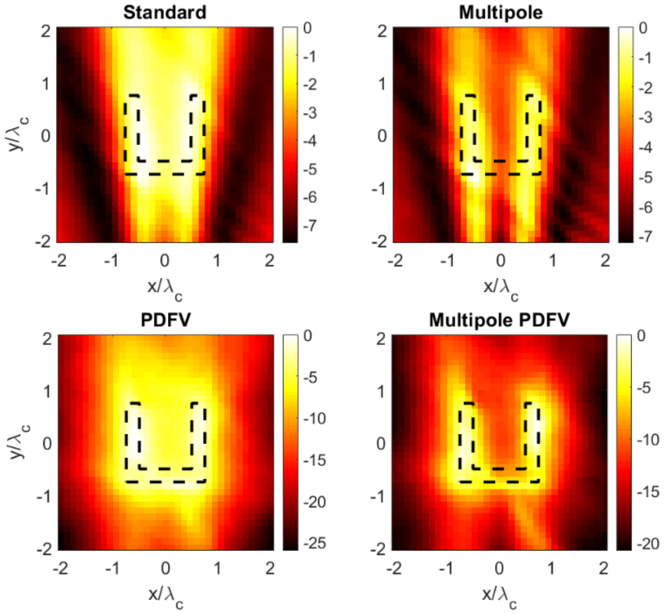

Fig. 11—Imaging results for the various LSM formulations for the PEC U-shaped target using receiver angles $[0°, 255°, 270°, 285°]$

We close this subsection by considering results for the "Austria" profile, which is expected to the most difficult target to image due to the high degree of nonlinear scattering interactions between its various features. Fig. 12 shows results for a dielectric version of the target using the same receiver set used for Fig. 9. As in Fig. 9, the standard and standard multipole results are very poor. The PDFV results are improved in that the areas of high indicator function are localized around the target support, but there is significant missing detail. The multipole PDFV results are of the best quality, in that the ring-shaped nature

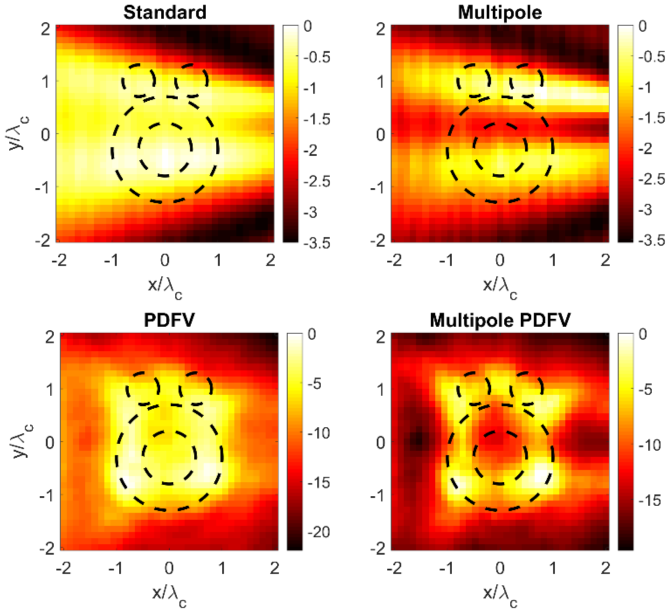

Fig. 12—Imaging results for the various LSM formulations for the dielectric "Austria" target using receiver angles $[0°, 15°, 180°, 345°]$

of the target is apparent and the overall dimension of the target is a reasonable match to truth. There is some aberrance in the multipole PDFV image, as the target void is not centered. Higher indicator function values are concentrated in the vicinity of the two smaller discs, but the two discs are not individually resolved. Still, the multipole PDFV results are clearly superior to the standard LSM imagery. The results across all three targets in this subsection suggest that the PDFV constraint, when combined with the multipole LSM formulation, leads to significant imaging improvement in sparse-aperture cases, even for challenging (i.e., non-convex or high-contrast) targets.

### *3.4.3 Results Across a Variety of Receiver Sets*

In this subsection, we evaluate imaging performance across a wide variety of receiver choices to give a comparison between standard and PDFV-LSM imaging across a more comprehensive randomized variety of receiver sets. For $N_{\text{rec}} = 2 - 6$, we choose 10 random sets of receive locations from a uniform distribution across the aperture, and for each set, we compute the standard LSM, standard multipole LSM, PDFV-LSM, and multipole PDFV-LSM solutions for the dielectric L target. Each image trial uses regularization parameters $\log \alpha = -6, \log \beta = -1$. We then calculate the error metric Eq. (15) and average over the 10 random sets. The results are plotted in Fig. 13.

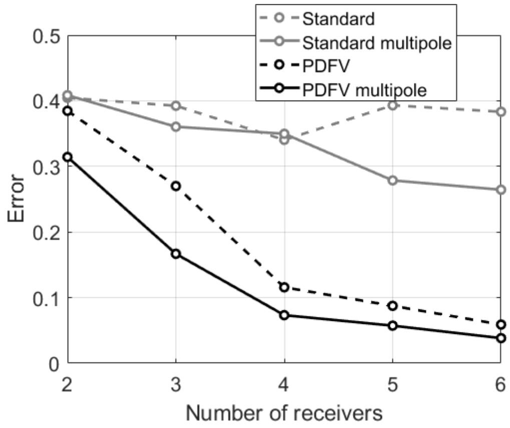

Fig. 13—The error metric for the PDFV and standard LSM formulations as a function of $N_{\text{rec}}$ for the dielectric L-shaped target. Each data point represents the average over 10 randomly chosen sets of receiver positions.

The results demonstrate a clear and significant improvement in imaging performance between the PDFV and standard LSM cases. The addition of the multipole enhancement leads to additional imaging improvements such that the multipole PDFV-LSM gives the best imaging results across all scenarios. For $N_{\text{rec}} \geq 4$, the multipole PDFV-LSM achieves an error rate of less than 0.10, indicating on average a very faithful reconstruction of similar quality to Fig. 8(c). In contrast, the multipole standard LSM results have average errors ranging from 0.25-0.35 over these choices of receivers, which is comparable or worse than the error for the significantly aberrant Fig. 7(b). The error metric worsens significantly for $N_{\text{rec}} = 2$ and 3 for the PDFV results while still outperforming the standard results. The error difference between the PDFV and standard reconstructions narrows as $N_{\text{rec}}$ decreases.

Using the PDFV formulation also leads to less variability in performance between receiver sets. For $N_{\text{rec}} = 4,5,$ or 6, the standard deviation in the fidelity metric is between 0.02 and 0.04 for the multipole PDFV-LSM and between 0.10 and 0.17 for the standard LSM. The standard deviation for the multipole PDFV worsens to between 0.08 and 0.11 for $N_{\text{rec}} = 2$ and 3 (versus 0.13 and 0.14 for the standard LSM), which is consistent with the overall degradation of PDFV performance for these receiver numbers. The variability of the metric about the mean is neglected from Fig. 13 for ease of visualization of the overall trends.

Images from this dataset are shown in Fig. 14 for $N_{\text{rec}} = 2, 3, 5$, and 6. For each choice of $N_{\text{rec}}$, we choose a representative image example from the set of 10 random receiver placements. The receiver angles for each example are listed in Table 1. The standard LSM reconstructions give very poor results for all

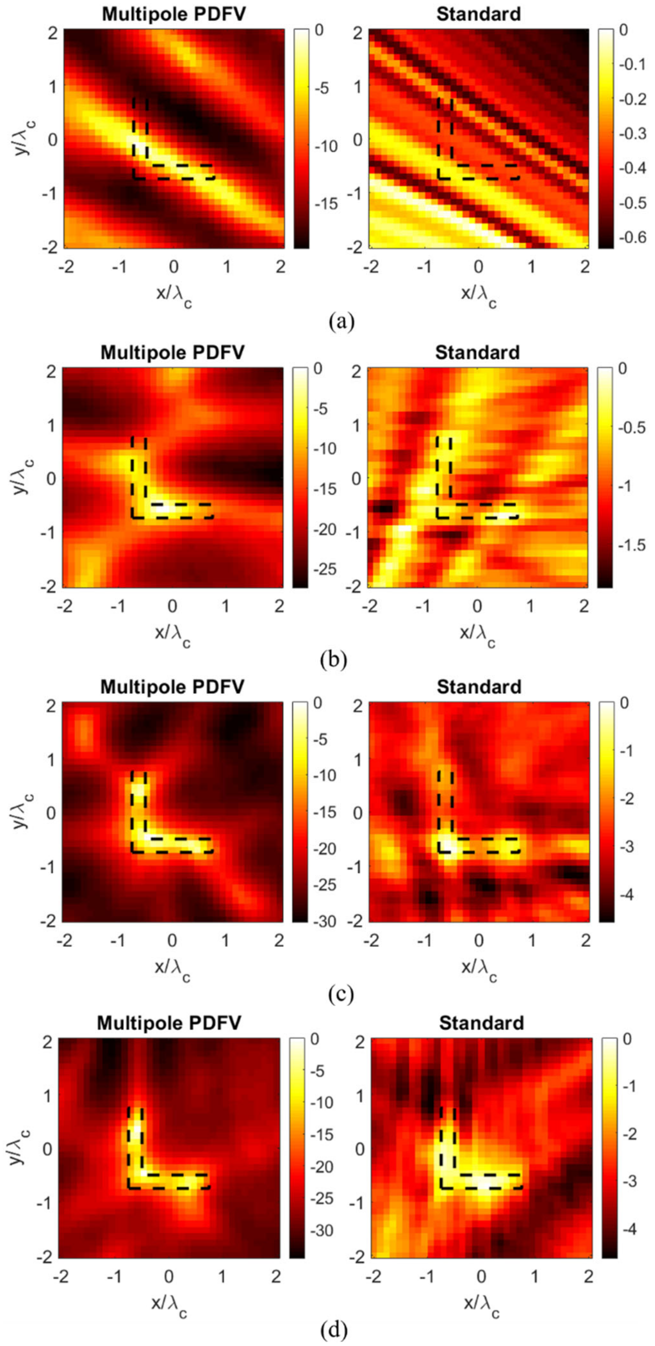

(a)

(b)

(c)

(d)

Fig. 14—Representative image results for the dielectric L-shaped target for (a) $N_{\text{rec}} = 2$, (b) $N_{\text{rec}} = 3$, (c) $N_{\text{rec}} = 5$,(d) $N_{\text{rec}} = 6$

Table 1—Receiver Angles

| $N_{\text{rec}}$ | Receiver angles |
|---|---|
| 2 | $33°, 265°$ |
| 3 | $114°, 214°, 261°$ |
| 5 | $12°, 113°, 249°, 296°, 339°$ |
| 6 | $11°, 32°, 49°, 136°, 162°, 269°$ |

receiver choices. The PDFV reconstruction for $N_{\mathbf{rec}} = 2$ is also of low quality. The PDFV reconstruction for $N_{\mathbf{rec}} = 3$ is a significant improvement over the standard case, but also suffers from several artifacts and a distortion in the reconstructed target shape. The PDFV $N_{\mathbf{rec}} = 5$ and 6 reconstructions are of high quality and are comparable to the four-receiver reconstruction in Fig. 8(c). These image results are consistent with the average results plotted in Fig. 13. These results, along with the results from previous subsections, suggest that high-quality target reconstructions can be achieved for the frequency range and target dimensions chosen for the simulated datasets using $N_{\mathbf{rec}} \geq 4$.

### *3.4.4 Experimental results*

Lastly, we report the results of processing the experimental data. We generate sparse-receive datasets by selecting subsets from the collected data wherein all eight antennas are used to transmit and only three are used to receive. We form standard, standard multipole, PDFV-, and multipole PDFV-LSM images for all possible combinations of three receivers, resulting in $\binom{8}{3} = 56$ sets of images. We form each image on a $9.5 \times 9.5$ cm, $35 \times 35$ cell grid. We use the L-curve procedure and once again select regularization parameters $\log \alpha = -6, \log \beta = -1$. As in previous subsections, we quantify the fidelity of each image using the quantitative error metric Eq. (15), the threshold Eq. (14), and the known target location and radius.

We plot histograms of the resulting error metric distribution across all 56 receiver sets in Fig. 15. The histograms show that the standard LSM results have the worst distribution of error, with a large

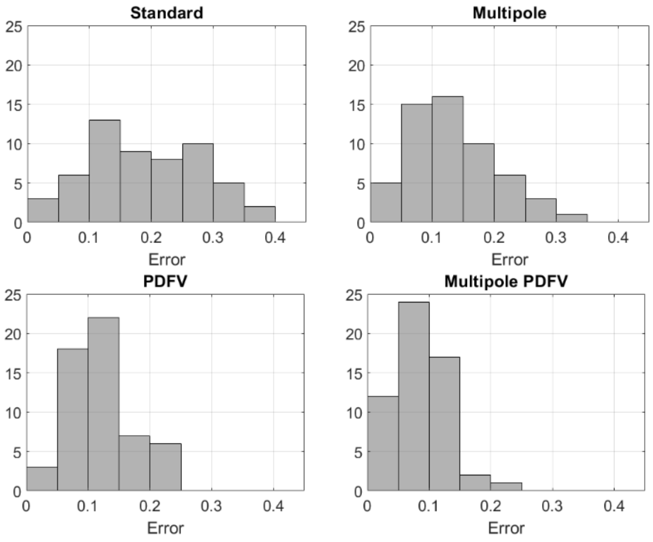

Fig. 15—Histograms of the error metric Eq. (15) for experimental imagery across all 56 possible choices of eight transmitters and three receivers

percentage of the receiver combinations resulting in high error. The multipole enhancement improves the error distributions for both the standard and PDFV cases. Likewise, the PDFV formulation outperforms the standard formulation with and without the multipole enhancement.

The multipole PDFV results are clearly of the highest fidelity, as the error distribution is concentrated at low error values. Only 5% of receiver sets result in errors greater than 0.15 for the multipole PDFV case, compared to 36% for the standard multipole and 61% for the standard cases.

The significant improvement provided by the multipole PDFV also can be observed by considering the error results on a receiver-set-by-receiver-set basis. The multipole PDFV-LSM outperforms the standard LSM and the standard multipole LSM for 91% and 85% of receiver sets, respectively.

We plot representative image examples from this data set in Fig. 16. Multipole PDFV results are shown in the left column and standard multipole results are shown in the right column. In Fig. 16(a), the receiver angles are 90°, 180°, and 270°. The standard multipole results include two long, aberrant tails that extend from the center of the imaging region to the top-left and bottom-left corners. The multipole PDFV results eliminate these aberrant tails and concentrate areas of high indicator function near the true target location, but somewhat off-center. In Fig. 16(b), the receiver angles are 0°, 225°, and 270°. The multipole PDFV results are a more faithful match to the true target shape and location compared to the standard multipole results, and the artifact near the bottom of the image is mitigated. In Fig. 16(c) the receiver angles are 45°, 270°, and 315°. The multipole PDFV image is a very good match to the true target shape and location, and the artifact running from the target to the bottom of the standard multipole image is eliminated. In all three of these examples, the fidelity of the multipole PDFV imagery is significantly improved compared to the standard multipole imagery, as predicted by the error histograms of Fig. 15.

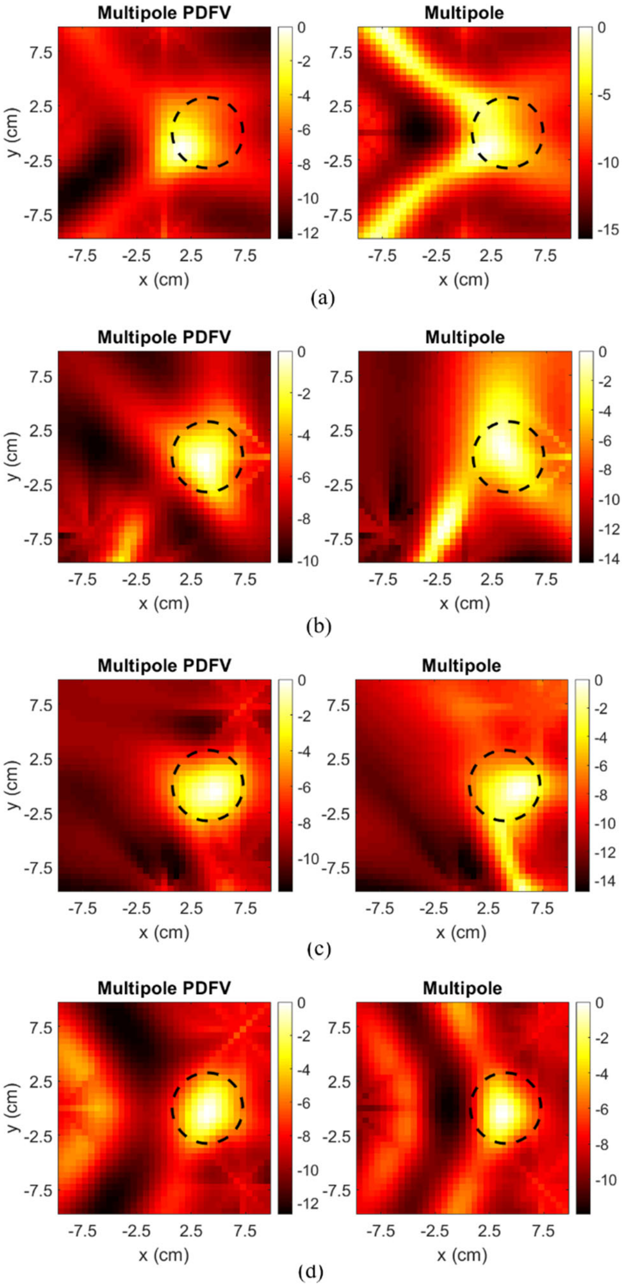

Fig. 16—Experimental imaging results for multipole PDFV and standard multipole formulations using receiver sets (a) [90°, 180°, 270°], (b) [0°, 225°, 270°], (c) [45°, 270°, 315°], and (d) [45°,180°, 315°]. In each image, the dashed lines denote the true boundary of the cylindrical target.

For completeness, we also include an imagery example for one of the few (i.e., 5%) cases in which the standard multipole outperforms the PDFV multipole according to the fidelity metric Eq. (15). This image, corresponding to receiver angles 45°, 180°, and 315°, is given in Fig. 16(d). The target shape and location are reconstructed reasonably well for both formulations, and the multipole PDFV formulation eliminates artifacts along the top and bottom image edges. However, the artifacts observed on an arc in the left half of the image are enhanced for the multipole PDFV formulation.

Overall, the experimental results shown in Fig. 15 and Fig. 16 demonstrate consistent and significant imaging improvement using the PDFV-LSM, especially with the multipole enhancement. These experimental results and the numerical results presented in the previous subsections together demonstrate the robustness of the PDFV-LSM concept across a wide range of sparse-aperture imaging scenarios.

### 3.5 Conclusion

We investigated a formulation of the linear sampling method for qualitative inverse scattering in data collection scenarios in which either the transmit or receive aperture is sparsely sampled in space. The proposed technique mitigates the lack of spatial data by incorporating *a priori* propagation information into the LSM inversion based on the expected phase delay from the transmitters to each pixel of interest. We evaluated the performance of the proposed technique by applying it to simulated and experimental data from various sparse-aperture imaging scenarios. We demonstrated improved imaging performance across a wide variety of sensor placements for both simulated and experimental scenarios. The proposed technique consistently achieves higher imaging fidelity compared to the standard Tikhonov-regularized LSM. We also showed that including a multipole enhancement to the formulation leads to further imaging improvements for targets that are non-convex or high-contrast as well as for experimental cases.

## 4. BOUNDARY-CONDITION-ENHANCED LINEAR SAMPLING METHOD IMAGING OF CONDUCTING TARGETS FROM SPARSE RECEIVERS

This section is adapted from a paper that has been accepted for publication in *IEEE Transactions on Antennas and Propagation* [32]. It builds upon work that was previously published in conference proceedings [35] and subsequently captured in an interim report for this project [39].

### 4.1 Background

Electromagnetic imaging of conducting targets is of interest for various applications such as nondestructive evaluation and target recognition. The imaging problem is generally nonlinear in the unknown contrast and ill-posed. Imaging strategies that rely on linear scattering assumptions such as the matched filter, therefore, often produce aberrant or ambiguous imagery. Conversely, quantitative inverse scattering techniques that seek to solve the nonlinear problem of reconstructing the dielectric profile of the target, such as the Born iterative method or the distorted Born iterative method [28, 29], often struggle to reconstruct high-contrast targets. These challenges motivate the development of qualitative inverse scattering techniques that reconstruct only the support of the conducting target.

A number of techniques for qualitative inverse scattering imaging of conducting targets have been reported in the past. Local shape function techniques (e.g., [48-50]) discretize the imaging domain into small conducting elements and then apply optimization to solve for scattering coefficients for each element. Subspace optimization methods discretize the scene into current lines and then optimize for a binary masking of the current lines that represent the target [51-54]. Several techniques solve for the contrast sources e.g., equivalent currents on the target surfaces, under the assumption that their locations are spatially sparse [55-60] (which is distinct from the problem posed by sparse receivers). Physical-optics-based approaches simplify the problem at high frequencies via linearization assumptions (at the obvious expense of introducing potential multiple-bounce artifacts) [61-63]. Recent inverse-problems-based approaches to radar imaging apply regularization to the conventional focusing problem to extract richer target information

[64-66]. Variations of the well-known MUSIC [67, 68] and the level-set techniques [69-72] also have been applied to the conducting target imaging problem.

In this section, we again focus on the linear sampling method (LSM) (e.g., [7, 27, 31, 33, 35, 40, 46, 73-76]). As previously stated, a significant challenge in imaging with the LSM is its need for dense multistatic-multiview data. In many practical imaging scenarios, constraints on hardware resources or data acquisition time may preclude achieving sufficient channel density in both the transmit and receive apertures simultaneously.

Richness in scattered-field data may in principle be achieved with a limited number of transmitters and receivers using synthetic aperture approaches. In this section, we concentrate on sparse-receive, dense-transmit datasets, which can be collected using a few stationary receivers and a single mobile transmitter. Such an approach is advantageous relative to alternative strategies for limiting hardware resources or data acquisition time. For instance, achieving dense multistatic-multiview sampling on both transmit and receive using synthetic aperture approaches could still require either a significant number of physical sensors or a prohibitive data acquisition time due to the need for multiple passes by the sensors. Alternatively, a low-to-moderate number of stationary sensors could be used on both transmit and receive, but this approach could potentially result in a larger number of overall physical sensors compared to the dense-transmit, sparse-receive configuration of interest.

However, application of standard LSM processing to sparse-receive datasets will often result in a large number of artifacts in the image or a complete loss of fidelity, even if the transmit aperture is densely sampled. Data richness may be enhanced through the use of multifrequency data, but straightforward application of additional frequencies to standard LSM processing may lead to limited improvement or even image degradation if the receive aperture is sparse. These challenges motivate the development of alternate LSM imaging formulations to take advantage of the information in the scattered field for effective sparse-receiver imaging.

Previous dense-transmit, sparse-receive LSM work has approached this problem by placing constraints on the frequency behavior of the LSM solution. In [75] and [43], a frequency variation (FV) formulation penalized overall changes in the LSM solution across frequency under the rationale that these changes are expected to be small in magnitude outside the vicinity of a sparse set of resonances. In [31], a phase-delay frequency variation (PDFV) formulation penalized solutions that deviated from a phase-relationship across adjacent frequencies that was related to the propagation distance between the transmitters and each pixel in the imaging domain. This latter approach relies on the perspective of the LSM as a transmit beamforming problem for focusing equivalent currents in the target volume [44]. It also relies on the Born approximation for derivation of the desired phase-delay behavior.

In this section, we develop and investigate a new formulation of the LSM for sparse-receiver imaging of conducting targets. The proposed approach is to discipline the LSM solution such that electric field boundary conditions for a perfect electric conductor are satisfied at an estimate of the target boundary. This is equivalent to choosing the LSM transmit beamformer weighting such that the resulting incident field on an estimate of the target boundary matches the scattered field, which results in the desired boundary condition of a total electric field of zero. Constraining the LSM solution via the boundary conditions effectively introduces useful *a priori* information into the LSM optimization, which compensates for the lack of spatial channels.

As the true target boundary is unknown, we propose an iterative procedure to jointly estimate the target boundary and the LSM solution by minimizing both the conventional LSM beamforming residual as well as the deviation from the desired boundary conditions. We show that the proposed boundary-condition-enhanced LSM (BC-LSM) results in significant improvements in imaging fidelity for sparse-receive, dense-transmit (or equivalently by reciprocity, dense-receive sparse-transmit) scenarios.

The BC-LSM is distinct from previous approaches to conducting target imaging. It does not discretize the target into a set of smaller canonical scatterers, as in [48-54]. It does not rely on contrast source sparsity to overcome the challenge of ill-posedness, as in [55-60]. It instead relies on a separate physical mechanism: the fundamental ability of the LSM to generate reweighted incident and scattered fields in the imaging domain, which it leverages by constraining for a near-zero field distribution on the target boundary.

The BC-LSM is also distinct from the PDFV-LSM and the radar-type imaging approaches in that it makes no use of the Born approximation. Lastly, unlike both the PDFV- and FV-LSM, the BC-LSM does not depend on small steps in frequency, and therefore may be used with widely spaced discrete-frequency data.

## 4.2 Imaging Formulation

### *4.2.1 LSM Fundamentals*

For ease of explication, we assume two-dimensional transverse magnetic (TM) propagation. A perfectly electrically conducting (PEC) target of unknown support $V$ and unknown boundary $\partial V$ is situated in the imaging domain. It is surrounded by an array of $N_{\mathrm{tx}}$ transmitters and $N_{\mathrm{rec}}$ receivers. The scattered field phasors at wavenumber $k$ for every transmit-receive sensor pair are collected in the multistatic scattered field matrix $\mathbf{E}_{\mathrm{s}}(k)$. The LSM operates by finding a regularized solution to the system of linear equations:

$$\mathbf{E}_{\mathrm{s}}(k)\mathbf{g}(k,\mathbf{r}) = \mathbf{\Phi}(k,\mathbf{r}), \tag{16}$$

where $\mathbf{r}$ is a pixel location in the imaging domain, $\mathbf{\Phi}(k,\mathbf{r})$ is the $N_{\mathrm{rec}} \times 1$ vector of Green's functions between each receiver and $\mathbf{r}$, and $\mathbf{g}(k,\mathbf{r})$ is the $N_{\mathrm{tx}} \times 1$ LSM solution vector for $\mathbf{r}$. In free space, the conventional Green's function for two-dimensional TM propagation is given by $\mathbf{\Phi}(k,\mathbf{r}) = k^2(4\omega\varepsilon)^{-1}H_0^2(k\mathbf{d}_{\mathrm{rec}})$, where $\omega$ is the radial frequency, $\varepsilon$ is the permittivity of the background medium, $H_0^2$ is the zeroth-order Hankel function of the second kind, and $\mathbf{d}_{\mathrm{rec}}$ is the vector of distances between $\mathbf{r}$ and the receive locations.

It can be shown that the norm of the LSM solution depends on whether $\mathbf{r}$ is inside or outside the target support. Solutions for interior pixels will have low norms, while pixels outside the target will have high norms [28]. Thus, an image of the target support can be formed by solving Eq. (3) for all $\mathbf{r}$ in the imaging domain and plotting an indicator function of the solution norm over $\mathbf{r}$. A typical indicator function for a multifrequency solution is given by

$$I(\mathbf{r}) = \int \|\mathbf{g}(k,\mathbf{r})\|^{-1} dk, \tag{17}$$

where the summation is over all collected frequencies.

As will be seen, solving Eq. (16) using a sparse set of transmitters or receivers will result in an $I(\mathbf{r})$ that is of low fidelity to the true target geometry. Our proposed approach to improving imaging performance is to incorporate electric field boundary conditions into the LSM regularization and then to jointly optimize the boundary-condition-regularized LSM residual and the estimated target boundary. The following two subsections cover the boundary condition regularization and the boundary estimation, respectively.

### 4.2.2 BC-LSM Regularization

Let $\partial U$ be an estimate of the true target boundary $\partial V$. We wish for the incident and scattered fields on $\partial U$ resulting from weighting the transmitted signals by $\mathbf{g}(k,\mathbf{r})$ to sum to zero, thereby fulfilling the boundary conditions for a PEC target. Simultaneously, we also wish for $\mathbf{g}(k,\mathbf{r})$ to satisfy Eq. (16) in order to achieve the LSM solution vector that allows for creation of the target image via Eq. (17).

Let $\partial U$ be discretized into $N_b$ boundary points whose locations in the imaging domain are given by $\mathbf{r}_\mathrm{b}^i, i = 1, \ldots, N_b$. We collect the incident fields at each boundary point arising from radiation from each transmitter into the $N_b \times N_\mathrm{tx}$ matrix $\mathbf{E}_\mathrm{i}^{\partial U}(k)$. Since the incident field is by definition the field from the transmitters when no target is present, it may be computed with knowledge of the transmitter locations and $\mathbf{r}_\mathrm{b}^i$. The incident fields resulting from applying the LSM weights are thus given by the product $\mathbf{E}_\mathrm{i}^{\partial U}(k)\mathbf{g}(k,\mathbf{r})$.

Likewise, we define the $N_b \times N_\mathrm{tx}$ matrix $\mathbf{E}_\mathrm{s}^{\partial U}(k)$ to be the collection of scattered fields on $\partial U$ resulting from radiation from each transmitter. If we assume that Eq. (16) has been solved faithfully, then by definition, applying the LSM weights to this scattered field matrix results in $\mathbf{E}_\mathrm{s}^{\partial U}(k)\mathbf{g}(k,\mathbf{r}) = \mathbf{\Phi}^{\partial U}(k,\mathbf{r})$, where $\mathbf{\Phi}^{\partial U}(k,\mathbf{r})$ is the $N_b \times 1$ vector of Green's functions between the boundary points and $\mathbf{r}$. Performing this transformation is useful because $\mathbf{E}_\mathrm{s}^{\partial U}(k)$ is dependent on the target, whereas $\mathbf{\Phi}^{\partial U}(k,\mathbf{r})$ can be computed directly using only knowledge of $\mathbf{r}$ and $\mathbf{r}_\mathrm{b}^i$.

Thus, constraining the LSM solution by the boundary conditions requires the minimization of the weighted total field quantity given by $\mathbf{E}_\mathrm{i}^{\partial U}(k)\mathbf{g}(k,\mathbf{r}) + \mathbf{\Phi}^{\partial U}(k,\mathbf{r})$. We incorporate this constraint into the LSM solution via the following optimization:

$$\min_{\mathrm{g}} \|\mathbf{E}_\mathrm{s}(k)\mathbf{g}(k,\mathbf{r}) - \mathbf{\Phi}(k,\mathbf{r})\|^2 + \alpha\|\mathbf{g}(k,\mathbf{r})\|^2 + \beta\left\|\mathbf{E}_\mathrm{i}^{\partial U}(k)\mathbf{g}(k,\mathbf{r}) + \mathbf{\Phi}^{\partial U}(k,\mathbf{r})\right\|^2. \tag{18}$$

The first normed term in Eq. (18), which we refer to as the residual, measures the closeness of the LSM solution to the desired relation in Eq. (16). The second normed term penalizes large-norm solutions. The third normed term penalizes deviations from the proposed boundary condition constraint. The scalars $\alpha$ and $\beta$ are regularization parameters that control the degree of penalty applied by each constraint. Setting $\beta = 0$ results in standard Tikhonov-regularized LSM.

### 4.2.3 Boundary Optimization

In order for the boundary condition constraint in Eq. (18) to enhance imaging performance, the boundary estimate $\partial U$ should be a good match to the true boundary $\partial V$. Otherwise, the boundary constraints will impose erroneous conditions on the LSM solution, potentially leading to low-fidelity imagery. Our approach is to jointly optimize the boundary and the BC-LSM solution. As will be seen, this optimization can be expected to be generally non-convex in the boundary, and thus challenging. We address this challenge via a procedure which involves iteratively perturbing the estimated boundary in order to lower the BC-LSM residual. The procedure is summarized via the flowchart in Fig. 17 and is explained in more detail below.

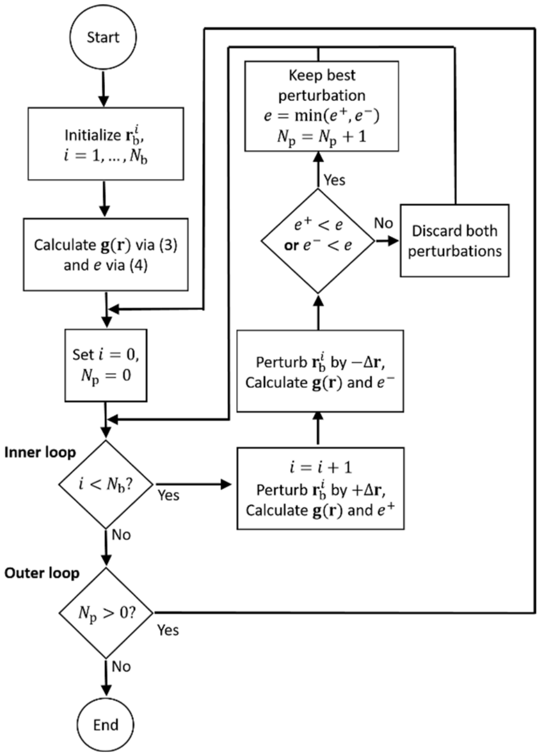

Fig. 17—A flowchart describing the procedure for estimating the target boundary via joint optimization with the BC-LSM solution

We begin by initializing $\partial U$ on a closed contour in the imaging region and distributing boundary points along it with uniform spacing. We form the BC-LSM solution via Eq. (18) and record the following function of the residual:

$$e = \frac{1}{A}\int_U \left(\int \|\mathbf{E}_\mathrm{S}(k)\mathbf{g}(k,\mathbf{r}) - \mathbf{\Phi}(k,\mathbf{r})\|^2 \,\mathrm{d}k\right)^{1/2} \mathrm{d}\mathbf{r}. \tag{19}$$

In Eq. (19), the spatial integration is over all points in $U$, i.e., the open set bounded by $\partial U$, the frequency summation is once again over all collected $k$, and the normalization factor $A$ is the area of $U$.

We then update $\partial U$, perturbing the boundary points in the following manner. We first initialize a variable representing the number of boundary point perturbations to $N_p = 0$. We cycle through each individual boundary point in sequence. For the $i$th boundary point, we perturb $\mathbf{r}_b^i$ first by vector $+\mathbf{\Delta r}_b^i$ and then by $-\mathbf{\Delta r}_b^i$, where $+\mathbf{\Delta r}_b^i$ points towards the center of the imaging scene. For each of the two perturbations, we compute Eqs. (18) and (19). The boundary point is then updated to the location $\mathbf{r}_b^i$, $\mathbf{r}_b^i + \mathbf{\Delta r}_b^i$, or $\mathbf{r}_b^i - \mathbf{\Delta r}_b^i$ that generates the lowest $e$. If the lowest $e$ is achieved by either $\mathbf{r}_b^i + \mathbf{\Delta r}_b^i$, or $\mathbf{r}_b^i - \mathbf{\Delta r}_b^i$, i.e., if perturbing the boundary point decreased the residual, then we increase $N_p$ by one. After cycling through all $N_b$ boundary points, we evaluate whether $N_p > 0$. If it is, then we reset the variable $N_p = 0$ and repeat the perturbation process over all boundary point again. We repeat the above process until no further perturbations lower the residual, i.e., until a loop over all boundary points ends with $N_p = 0$.

The rationale for this iterative procedure is based on the assumption that perturbing a section of $\partial U$ closer to the true $\partial V$ provides higher-fidelity *a priori* information to the LSM optimization via the boundary condition constraint in Eq. (18). Higher-fidelity constraints then result in a more faithful solution to Eq. (16) and thus a lower residual calculation in Eq. (19). We empirically investigate the assumptions underlying this heuristic by analyzing the effect of boundary changes on the residual in the following subsection. As will be seen, achieving a well-behaved boundary optimization depends on proper choice of regularization parameter as well as boundary initialization.

## 4.3 Results and Discussion

### *4.3.1 Simulated Data*

We generate simulated data for this study using the finite-difference time-domain (FDTD) method. The FDTD simulations assume two-dimensional TM propagation. An illustration of the simulation setup is given in Fig. 18.

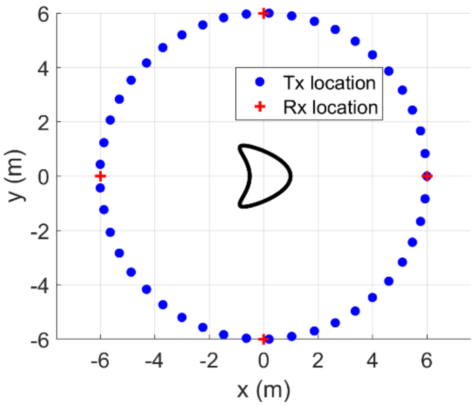

Fig. 18—A diagram of the simulation setup with the kite target

For each dataset, we place a target in the simulation domain and assign it a conductivity of $5.7 \times 10^7$ S/m, which is similar to copper. The rest of the domain is assigned free-space dielectric properties.

We uniformly and densely distribute transmit locations around the target on a circle of radius 6 m. Unless otherwise specified, we use 45 transmit locations. We then sequentially source each transmit location with an elementary current source. The resulting scattered fields are recorded at a sparse set of receive locations also uniformly distributed on a circle of radius 6 m. Unless otherwise specified, we use four receive locations. If we define the two-dimensional simulation domains with Cartesian *xy*-coordinates, then the four receivers are each placed along one of the cardinal axes. The recorded scattered fields are transformed to frequency-domain phasors using the discrete Fourier transform. We populate the $\mathbf{E}_s(k)$ matrices with the resulting phasors. The result is a sparse-receive, dense-transmit scattered field dataset. Following data acquisition, we add Gaussian white noise to the data. Unless otherwise stated, we choose the noise level such that the total signal-to-noise ratio (SNR) across all transmit-receive pairs is 40 dB.

### *4.3.2 Simulated Target Imaging Results: Fundamentals*

We begin imaging demonstrations using simulated data for the well-known kite target scaled to maximum dimension of around 2 m. The kite target support is visualized along with the data acquisition setup in Fig. 18. We perform multifrequency LSM and BC-LSM reconstructions using frequencies 100, 125, and 150 MHz.

For BC-LSM reconstructions, we place $N_b = 50$ boundary points in the imaging scene. As the transmitters in the simulated dataset are elementary current sources, we calculate $\mathbf{E}_{\mathrm{i}}^{\partial U}(k)$ for use in Eq. (18) in a straightforward manner by computing the Green's functions between each transmit location and $\mathbf{r}_b^i$.

In previous sparse-aperture LSM work using two regularization terms [31], we have found that the effect of the regularization parameters on imaging performance is mostly a function of the ratio between the two parameters. We have found this to be true for the BC-LSM, as well. For brevity, we therefore set a constant $\log\alpha = -5$ and vary only $\beta$ in order to investigate the effects of stronger or weaker boundary condition penalties on imaging performance.

We first evaluate the characteristics of the residual in order to determine whether the optimization strategy can be expected to converge to the true target boundary. In Fig. 19, we plot *e* for boundaries in the form of circles centered in the imaging domain. It is not practical to evaluate the residual function for every perturbation of each individual boundary point, and thus we instead evaluate the behavior of the residual by varying only the radii of circles. The set of $\mathbf{r}_b^i$ are distributed uniformly across each circular boundary. For each data point in Fig. 19, we first compute the BC-LSM solution via Eq. (18) for an imaging domain of dimension $3 \times 3$ m on a $50 \times 50$ cell grid and then compute and plot *e* via Eq. (19). We consider the behavior for choices of $\log\beta$ ranging from –9 to 0.

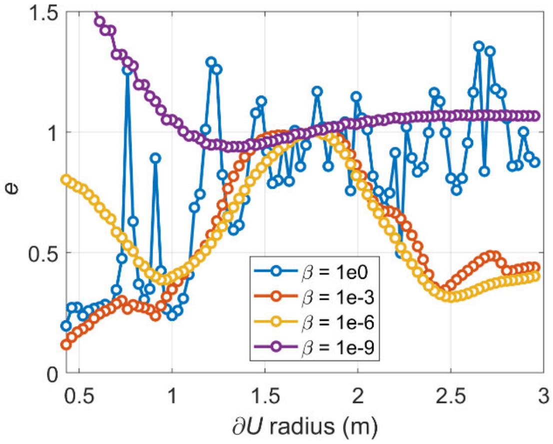

Fig. 19—The residual function *e* from Eq. (19) for the kite target using circles of varying radius as the estimated boundary. For each choice of $\beta$, the *e* curve is normalized to its value at 1.75 m.

Each residual function curve in Fig. 19 has a local minimum in the vicinity of a boundary radius of around 1 m, which is comparable to the average radius of the kite target. For $\log\beta = -9$, and $\log\beta = -6$, the residual functions appear to be locally convex for a relatively broad range of radii in the vicinity of this local minimum. For $\log\beta = -9$, there are no other local minima on the investigated range of radii. However, the residual curve for this $\beta$ varies slowly in the vicinity of the minimum, which suggests that boundary perturbations result in small changes to the residual function. Increasing $\log\beta$ to $-6$ results in a deeper local minimum near a radius of 1 m, as well as an additional local minimum near 2.5 m. Increasing $\log\beta$ to $-3$ and $0$ results in residual functions that are locally convex over a smaller range of radii in the vicinity of 1 m. It also results in significantly more numerous local minima. The residual curve for $\log\beta = 0$ is particularly chaotic.

These results suggest that for an appropriate choice of regularization parameter and an initial boundary that is not too far from the true boundary, the residual function may be made approximately locally convex, and thus perturbing the estimated boundary towards the true boundary lowers the residual function in Eq. (19). In principle, this enables the boundary optimization procedure from Section 4.2.3 to generate a boundary estimate that is of similar dimension as the true boundary.

Next, we investigate empirically whether the full boundary-point-by-boundary-point optimization procedure described in Section 4.2.3allows for estimating the target boundary shape as well as its size. We initialize $\partial U$ to be a circle of radius 1.3 m, which is about halfway between the local minimum corresponding to the true target dimension and the adjacent local maximum for the $\log\beta = -6$ curve. In principle, we could instead choose to initialize the boundary radius directly at the radius of the residual function minimum. We instead choose an initial radius offset from the minimum, but within the convex region near the minimum, to provide a more interesting demonstration of the robustness of the optimization method in converging to the true boundary. We set the boundary point perturbation step size to be 0.1 m. We generate the images on a domain of dimension $2 \times 2$ m on a $35 \times 35$ cell grid.

Image results are shown in Fig. 20. In these images and all subsequent images in this paper, we plot $20\log I(\mathbf{r})$ as defined in (17). Each image is scaled so that 0 dB is defined by the most intense pixel and the lowest value in the color bar is given by the least intense pixel.

Fig. 20(a) shows the image obtained via standard Tikhonov-regularized LSM. As expected, due to the sparsity of the receive aperture, the image is a poor match to the true target geometry, with many artifacts distributed throughout the imaging domain. Fig. 20(b) shows a BC-LSM reconstruction with $\log\beta = -3$ for the initial placement of the boundary points. The boundary point locations are marked in the image with blue circles. This image is also very aberrant, as the initialized boundary is a poor match to the true target boundary.

The remaining subfigures in Fig. 20 show BC-LSM images obtained after convergence of the boundary estimates following the procedure outlined in Section 4.2.3. The results for Fig. 20(c-f) were obtained using $\log\beta = -9, -6, -3$, and 0, respectively. It is clear from the results that the image quality as well as the boundary estimate fidelity are both a strong function of $\beta$. Choosing $\log\beta = -9$ results in a poor boundary estimate and a poor image. The boundary estimate is most likely of poor quality due to the weak dependence of $e$ on boundary point location for this choice of $\beta$, as seen in Fig. 19. The weak dependence may signify a higher probability that perturbations in the wrong direction may lower the residual for some individual boundary points due, for instance, to noise or other imperfections. Choosing $\log\beta = -6$ results in a high-fidelity boundary estimate due to the favorable behavior of $e$ for this choice of $\beta$, i.e., a significantly decreasing, approximately convex residual in the vicinity of the true target boundary. However, the BC-LSM image is of low quality in this instance. This is most likely because the value chosen for $\beta$ scales the boundary condition penalty term too low relative to $e$ to effectively constrain the behavior of the norm of $\mathbf{g}(k, \mathbf{r})$, even though the penalty injects enough scattering information to allow for a well-behaved residual in the vicinity of the true boundary.

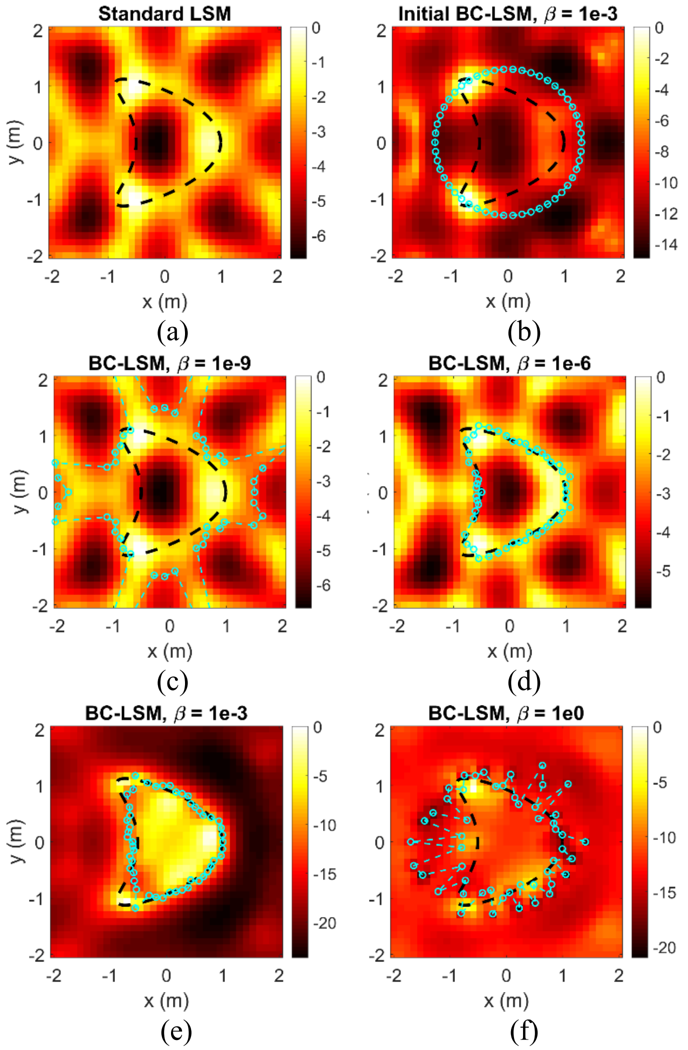

Fig. 20—LSM and BC-LSM imagery for a kite target and a sparse set of four receivers. (a) Standard Tikhonov-regularized LSM. (b) BC-LSM for the initial placement of boundary points. (c–f) BC-LSM after convergence of the estimated boundaries for various choices for $\beta$. Blue circles represent boundary point locations. Color bars are on a logarithmic scale, with 0 dB referenced to the most intense pixel.

Choosing $\log \beta = -3$ results in a reasonable boundary estimate that does not fully capture the non-convex portion of the kite. The corresponding BC-LSM imagery is of much improved quality, with diminished artifacts outside the true target support, due to the higher value of $\beta$ and thus the increased influence of the boundary condition penalty on the reconstructions. Lastly, choosing $\log \beta = 0$ results in a poor boundary estimate and poor image quality. The greater error in boundary estimate can be explained by the higher prevalence of local minima for higher $\beta$ values, as seen in Fig. 19.

Fig. 19 and Fig. 20 demonstrate that the BC-LSM optimization strategy results in accurate target boundary estimation and improved imaging performance if regularization parameters are chosen correctly. Furthermore, the results suggest a tradeoff in choice of $\beta$. Choosing $\beta$ high enough to inject sufficient boundary condition *a priori* information to achieve a significantly decreasing residual function in the vicinity of the true boundary, but low enough to avoid a significant number of other local minima, allows the optimization to converge to a faithful estimate of the target boundary. However, a $\beta$ that is low enough to avoid unwanted local minima may be too low to effectively constrain the behavior of the LSM solution norm. Conversely, a $\beta$ that is high enough to influence the solution norm may lead to a poorly or sub-optimally converged boundary estimate, which may then degrade the final image quality.

The benefits of both high and low $\beta$ may be achieved by using different $\beta$ for boundary optimization and the final image formation. The choices for $\beta$ may be selected via the following heuristic-based process, which we refer to as a multiple-$\beta$ reconstruction.

First, $e$ as a function of boundary radius and $\beta$ is plotted in the fashion of Fig. 19. The best $\beta$ for boundary optimization is chosen by selecting the most favorable residual function. We define the most favorable residual function to have qualities most similar to the $\log \beta = -6$ curve in Fig. 19, i.e., 1) it appears locally convex across a broad range of radii around the local minimum of interest, thereby allowing for the avoidance of false solutions, and 2) it is not shallow or nearly flat in the vicinity of the minimum, which helps to avoid perturbations of boundary points in the wrong direction due to noise or other imperfections. The local minimum of interest, which corresponds approximately to the overall dimension of the target, may be identified by generating an estimate of the target size from the scattered field data by, for instance, conventional backprojection processing.

We initialize the boundary as a circle with a radius within the convex region of the local minimum of interest, i.e., 1.3 m for the kite as in the previous examples. We then perform the iterative boundary optimization procedure with the selected $\beta$ to achieve a high-fidelity boundary estimate.

Second, the converged boundary is kept constant and a new series of BC-LSM images is created via Eq. (18) with a variety of $\beta$. The final BC-LSM image is chosen to be the one that results in the largest fraction of the image norm inside the converged boundary. That is, the image is chosen that corresponds to $\beta$ that satisfies the following maximization

$$e \max_{\beta} \left( \int_{U} I^2(\mathbf{r}) d\mathbf{r} \right)^{1/2} \left( \int_{\substack{\text{Entire} \\ \text{domain}}} I^2(\mathbf{r}) d\mathbf{r} \right)^{-1/2} . \tag{20}$$

We demonstrate a multiple-$\beta$ reconstruction of this type using the kite data. We select $\log \beta = -6$ for the boundary optimization step. We then compute the ratio in Eq. (20) using the converged boundary and $\log \beta$ ranging from –9 to 3. The resulting image norm ratios are plotted in Fig. 21(a). Lastly, we display the final BC-LSM image for the choice of $\log \beta = -2$, which maximizes Eq. (20). This result is shown in Fig. 21(b). As can be seen, the multiple-$\beta$ reconstruction results in high fidelity for both the LSM image as well as the estimated target boundary.

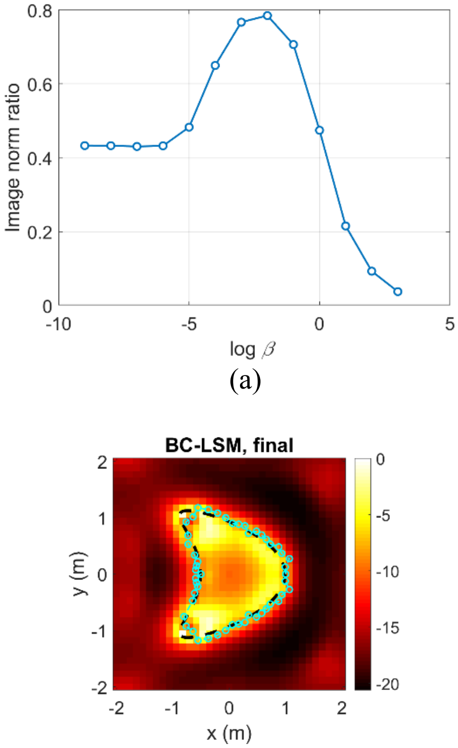

(a)

(b)

Fig. 21—Results of a multiple-$\beta$ reconstruction. (a) The ratio of image norm inside the converged estimated target boundary to the image norm throughout the image. (b) The BC-LSM reconstruction for the $\beta$ that maximizes this ratio. The color bar and blue circles have the same meaning as in Fig. 20.

We close this subsection with a note on computational expense. Using the multiple-$\beta$ reconstruction behavior, Eq. (18) must be solved many times between the initial parameter selection step, the optimization of the boundary, and the final parameter selection and image formation step. However, the computational expense is not prohibitive, as the LSM is a relatively low complexity inverse scattering technique that only requires finding solutions to systems of linear equations.

As an illustrative example, we report the total computation time needed to generate the image in Fig. 21(b) using the multiple-$\beta$ reconstruction procedure on a laptop running MATLAB with a 4-core 3.1 GHz processor and 32 GBs of RAM. The computation time was approximately 45 seconds to compute the results in Fig. 19 for selection of the initial $\beta$ and approximately 1 minute to perform the boundary optimization and computation of the final image via the image norm ratio. Computation time may be minimized by only calculating Eqs. (18) and (19) for points interior to the current boundary during the boundary optimization step. In general, the computational expense for other imaging cases can be expected to scale with the number of receivers, transmitters, frequency samples, pixel density, and number of boundary points.

### *4.3.3 Effects of Noise Level*

Next, we consider the effects of varying levels of noise on the BC-LSM reconstruction. Using the same kite target and data acquisition setup, we scale the noise such that the resulting SNRs are 30, 20, 10, and 0 dB. We generate BC-LSM images using the same imaging setup and multiple-$\beta$ reconstruction approach.

The results are shown in Fig. 22. The 30 and 20 dB SNR boundary estimates and reconstructions are very similar to the results shown in Fig. 21 and are both of high fidelity. The 10 dB SNR example also evinces a high-fidelity boundary estimation and a reasonably high-fidelity reconstruction. Lastly, the 0 dB SNR example has a modestly degraded boundary estimation and a very poor BC-LSM reconstruction. Overall, the results suggest that the BC-LSM is reasonably robust to noise.

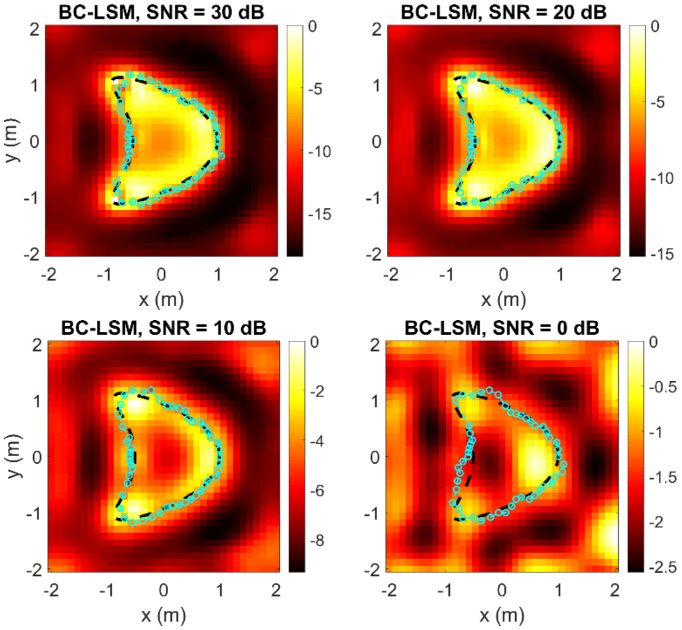

Fig. 22—BC-LSM reconstructions for varying noise levels. The color bar and blue circles have the same meaning as in Fig. 20.

### 4.3.4 *Effects of Lower Conductivity*

In this subsection, we consider the performance of the BC-LSM when the target conductivity is lower and thus the total field at the target boundary may diverge from the PEC boundary condition assumed in Eq. (18). While the primary purpose of the BC-LSM is for imaging highly conducting targets, observing the behavior of the technique in lower-conductivity cases provides additional context on the robustness of the technique to the optimization assumptions. It also provides a demonstration of the effects of erroneous boundary estimates and boundary conditions on the BC-LSM reconstruction.

We generate simulated data for the kite target using conductivities of 64, 16, 4, and 0 mS/m and dielectric constants of 2 and 6. We perform a multiple-$\beta$ reconstruction for each choice of dielectric properties. We use the same choices of transmitter/receiver numbers and frequencies as in the previous examples and set the initial boundary radius to 1 m.

We plot the converged BC-LSM imagery in Fig. 23 for each choice of dielectric properties. For a conductivity of 64 mS/m, the reconstructions are of high fidelity and very similar to the reconstruction from the original higher-conductivity examples. The boundary estimates also closely adhere to the true target boundary. This result demonstrates that near-perfect conduction is not required for the boundary condition constraint in Eq. (18) to enable high-fidelity imaging from sparse receivers. If a near-zero LSM-weighted

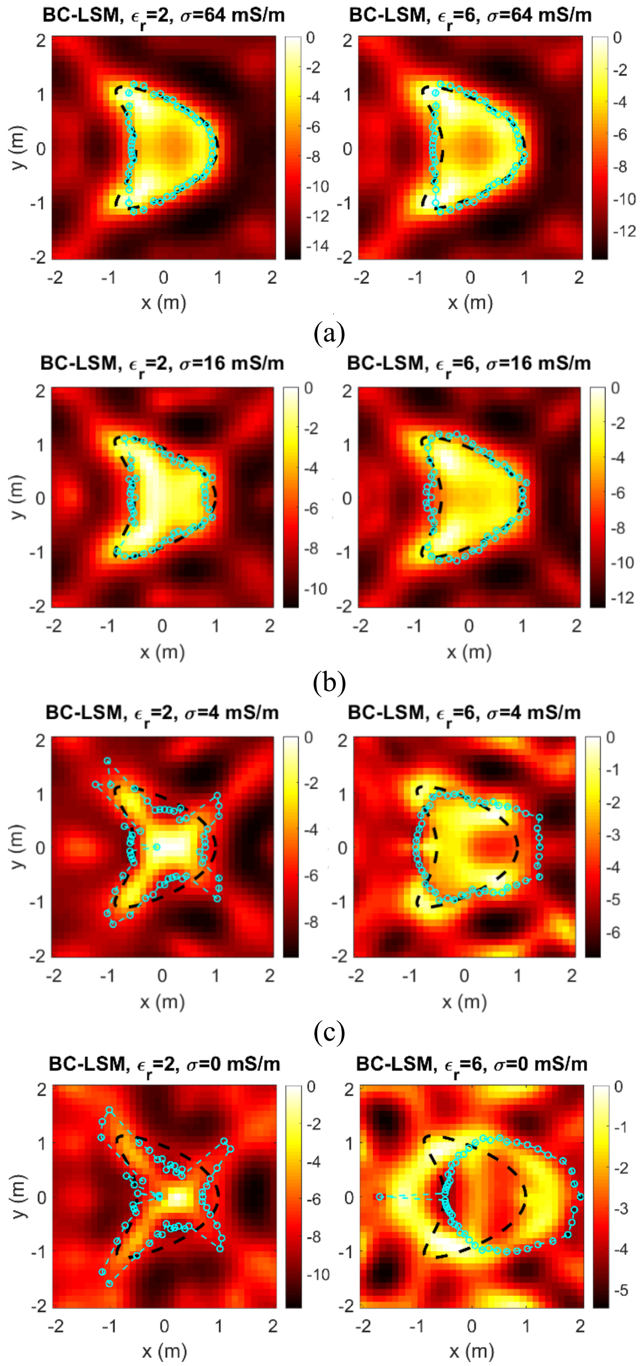

(a)

(b)

(c)

(d)

Fig. 23—BC-LSM reconstructions for lower conductivity. The target dielectric constants are (left) 2 and (right) 6. The conductivities are (a) 64, (b) 16, (c) 4, and (d) 0 mS/m. The color bar and blue circles have the same meaning as in Fig. 20.

field distribution can be achieved along the target boundary, as suggested by the boundary estimates in Fig. 23(a), then *a priori* information from the boundary condition constraint will still mitigate the lack of spatial channels.

As conductivity decreases, the boundary estimates progressively degrade and the BC-LSM reconstructions degrade accordingly. The nature of the boundary estimate degradation is different for the two choices of dielectric constant. For a dielectric constant of 2, the boundary is stretched towards the four corners of the image as the conductivity decreases. For a dielectric constant of 6, the boundary becomes progressively elliptical and shifted to the right. The characteristics of the degradation in each case are most likely the result of the joint boundary-LSM optimization converging to a local minimum. The differences in erroneous boundary are most likely due to differences in the scattered field, the LSM-weighted incident fields, and the resulting total fields caused by the differing target properties, which, in turn, determine the optimization local minima.

The nature of the BC-LSM reconstruction degradation also differs between the two choices of dielectric constant. When the dielectric constant is 2 and the conductivity approaches zero, the resulting BC-LSM reconstruction no longer has a high indicator function throughout the target support, but is instead mostly concentrated at the target center. When the dielectric constant is 6 and the conductivity approaches zero, the BC-LSM reconstruction's region of high indicator function is mostly outside of the true target support.

The differing degrees of reconstruction degradation between the two choices of dielectric constant in the lossless case are most likely due to the differences in the shapes of the estimated boundaries. For a dielectric constant of 2, the estimated boundary mostly envelopes pixels that are interior to the target and for which a low-norm solution to Eq. (16) therefore theoretically exists. Thus, the results in Fig. 23(d) suggest that for a collection of pixels in the interior of the target and the erroneous boundary, there exists an approximate solution to Eq. (16) that results in near-zero total fields on the optimized boundary. Conversely, the estimated boundary for a dielectric constant of 6 envelops a large proportion of non-target space for which Eq. (16) cannot be satisfied according to the fundamentals of LSM regardless of the boundary conditions, resulting in worse artifacts.

### *4.3.5 Behavior at Target Resonances*

It is well known that the full-aperture LSM solution norm grows very large for a discrete set of target-dependent resonant frequencies (i.e., Dirichlet or transmission eigenvalues). Single-frequency LSM images formed at a resonance are often of reduced fidelity, as the indicator function may be comparable for pixels inside and outside the target support. More positively, the resonances identified via measurement of the LSM frequency response may be leveraged for characterizing target properties (e.g., [12, 77-79]) or for target recognition (which has previously been investigated specifically for conducting targets [80]), as the set of resonant frequencies is dependent upon the target constitution and geometry. An investigation of such an application of the BC-LSM is outside the scope of this study. However, these positive and negative aspects of the LSM frequency response motivate an investigation into whether the BC-LSM responds similarly to resonances. In this subsection, we demonstrate the BC-LSM resonant response and compare it to the standard LSM response for sparse-receive scenarios.

We first investigate whether the norm of the solution to Eq. (18) evinces the expected resonant behavior and whether this behavior occurs at the expected frequencies. We again form multiple-$\beta$ BC-LSM solutions of the conducting kite target. We set the SNR to 30 dB. For the boundary estimation step, we again use frequencies 100, 125, and 150 MHz. We then calculate the final $\beta$ via Eq. (20) and calculate the solution to Eq. (18) with the optimized boundary using a denser set of 121 frequencies from 100 to 300 MHz in order to capture the resonant behavior.

We then identify pixels that satisfy the threshold

$$\log I(\mathbf{r}) > \min \log I(\mathbf{r}) + \nu(\max \log I(\mathbf{r}) - \min \log I(\mathbf{r})). \tag{21}$$

This threshold has been used in previous work [31, 46] to identify pixels belonging to the target support. We set the threshold parameter $\nu$ to 0.5. At each individual frequency, we then calculate the maximum norm of $\mathbf{g}(\mathbf{r}, k)$ across all identified pixels.

The results are plotted in Fig. 24 for two different sparse-receiver scenarios. In Fig. 24(a), we use the same distribution of four receive locations and 45 transmit locations as we used in previous subsections. In Fig. 24(b), we increase the number of receive locations to 5 and the number of transmit locations to 180. In each case, we plot BC-LSM and standard Tikhonov-regularized LSM results for four different target rotation angles. The range of target rotations in each scenario is chosen to achieve the widest possible angular variety after taking into account rotational symmetry from the point of view of the receivers. In each plot, we denote the expected resonant frequencies of the target with vertical dashed lines. We calculate the expected resonant frequencies by scaling the first five resonances of the kite target as computed in [81] by 133% to account for the difference in the size of the target used here. The resulting expected resonances are at 138.5, 201.6, 221.2, 269.4, and 273.7 MHz.

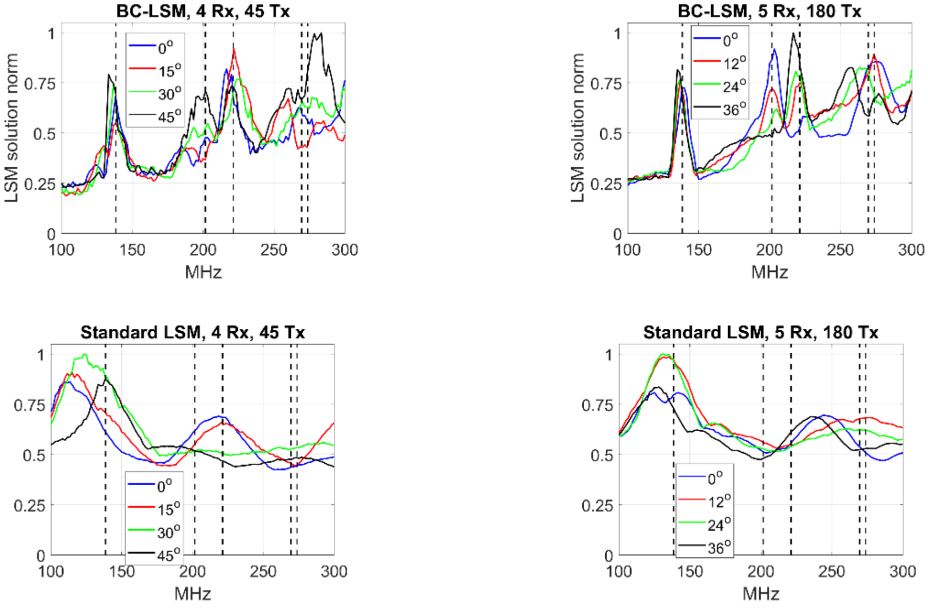

(a) (b)

Fig. 24—BC-LSM and standard LSM solution norms as a function of frequency for the kite target using (a) four receive locations and 45 transmit locations, and (b) five receive locations and 180 transmit locations. The legend refers to target rotations. Values are normalized to the maximum value across all curves in each plot. Vertical lines correspond to the theoretical resonant frequencies for the PEC kite target.

The BC-LSM solutions evince identifiable peaks in the close vicinity of the lowest three expected resonant frequencies for most target rotations. Peaks are also identifiable in the vicinity of the higher two resonances, but they are less precise in their clustering. The larger variation in the shift of the peaks for these two resonances may be due to their very close spacing or to the greater challenge of capturing higher spatial frequencies with the sparse receiver set. All observed peaks are sharper and more consistent for the BC-LSM solutions in Fig. 24(b), most likely due to the larger number of sensor locations.

In contrast, the standard LSM solutions in both Fig. 24(a) and Fig. 24(b) capture the resonances of the target less faithfully. The peaks in the curves are broader and less consistently centered on the expected resonances. In particular, the standard LSM curves in both scenarios do not individually resolve the second and third resonances, whereas the BC-LSM curves in in Fig. 24(b) have distinct local maxima at these resonances in three out of four of the target rotations. These results demonstrate that the BC-LSM better conserves the expected resonant frequency response in sparse-receiver scenarios as compared to standard Tikhonov-regularized LSM.

The above confirmation of the locations of the resonances under the BC-LSM framework allows us to next investigate the effects of operating the full BC-LSM directly at a resonance. For the scenario with five receivers and 180 transmitters, we first form a BC-LSM single-frequency, multiple-$\beta$ reconstruction at the lowest target resonance of 138.5 MHz. The results are shown in Fig. 25(a). Both the boundary estimate and the reconstruction are of poor fidelity. We then shift the reconstruction frequency by -15 and +15 MHz and plot the results in Fig. 25(b) and Fig. 25(c), respectively. These results demonstrate that shifting the reconstruction frequency away from the resonance improves the boundary estimation and reconstruction. Lastly, we perform a reconstruction using five frequencies distributed between 100 and 138.5 MHz, i.e., we perform the BC-LSM reconstruction with one resonant frequency and four non-resonant frequencies, which also results in an improved boundary estimation and reconstruction compared to Fig. 25(a). These results demonstrate that the BC-LSM can suffer from artifacts in single-frequency mode in the vicinity of a resonance, but, like standard Tikhonov LSM, these effects can be mitigated through multiple-frequency operation using the so-called "parallel" indicator function given in Eq. (17) [74].

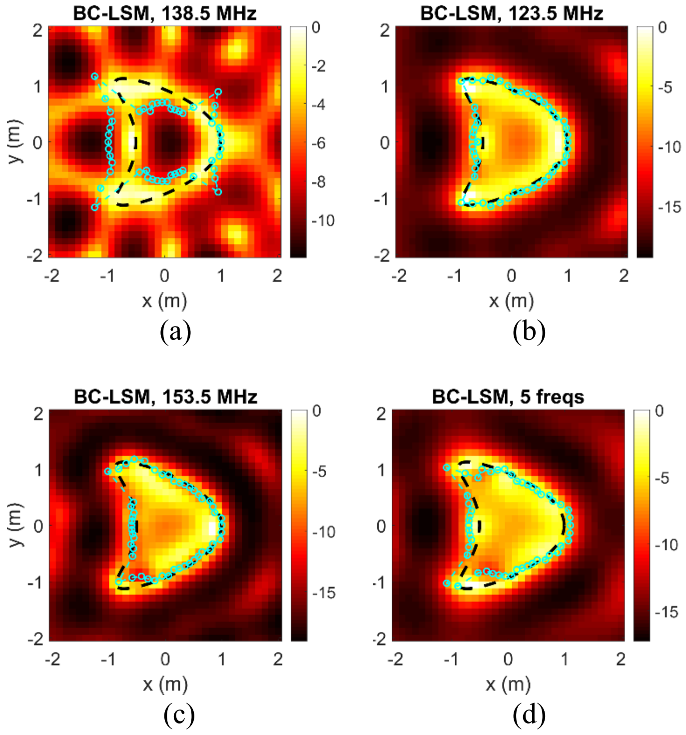

Fig. 25—BC-LSM images showing the effect of resonances on the reconstruction. (a)-(c): Single-frequency images at 138.5 MHz, (the lowest kite resonance), 123.5 MHz, and 153.5 MHz, respectively. (d): A reconstruction with five frequencies uniformly distributed from 100 to 138.5 MHz, inclusive of the target resonance at 138.5 MHz.

#### *4.3.6 Additional Results From Simulated Targets*

In this subsection, we explore the robustness of the proposed BC-LSM image formation strategy across a wider variety of simulated complex targets. We once again set the number of receivers to four. We increase the number of frequency samples to 21 uniformly distributed between 100 and 300 MHz and decrease the perturbation step size to 0.05 m in order to reconstruct targets of higher geometric complexity.

Standard and BC-LSM image results for three example target scenes are given in Fig. 26. The first example, shown in Fig. 26(a), uses a conducting version of the Austria target that has been used in previous studies (e.g,[31,46]). The second, shown in Fig. 26(b), uses a cross target. The last, shown in Fig. 26(c), uses two disconnected targets in the form of an L-shaped scatterer and a disc.

The standard LSM reconstruction of each scene is of poor quality due to the sparse set of receivers. In each case, numerous high-level artifacts are distributed throughout the image. The reconstructed target shapes are also either distorted or incomplete, especially for the cases of the Austria and L-and-disc scenes.

We generate the BC-LSM images in Fig. 26 using the multiple-$\beta$ reconstruction strategy. For each target, we perform a residual function analysis of the same form as shown in Fig. 19. The residual function curves are similar to the curves in Fig. 19, and are thus neglected here for brevity. The result of the curve analysis is that the optimum regularization parameter choice for boundary optimization is once again $\log \beta = -6$ for each scene.

The converged boundaries are a good match to the target geometries for each scene. For the Austria and cross targets, the estimated boundaries closely approximate the convex hulls of the true target boundaries. Similarly, the estimated boundary for the most challenging L-and-disc scene is a good match to the outer-facing boundaries of both constituent scatterers. Based on these results as well as the results in Fig. 21, it appears that the BC-LSM boundary estimation procedure may capture non-convexities for some targets, but may capture non-convexities imperfectly in general.

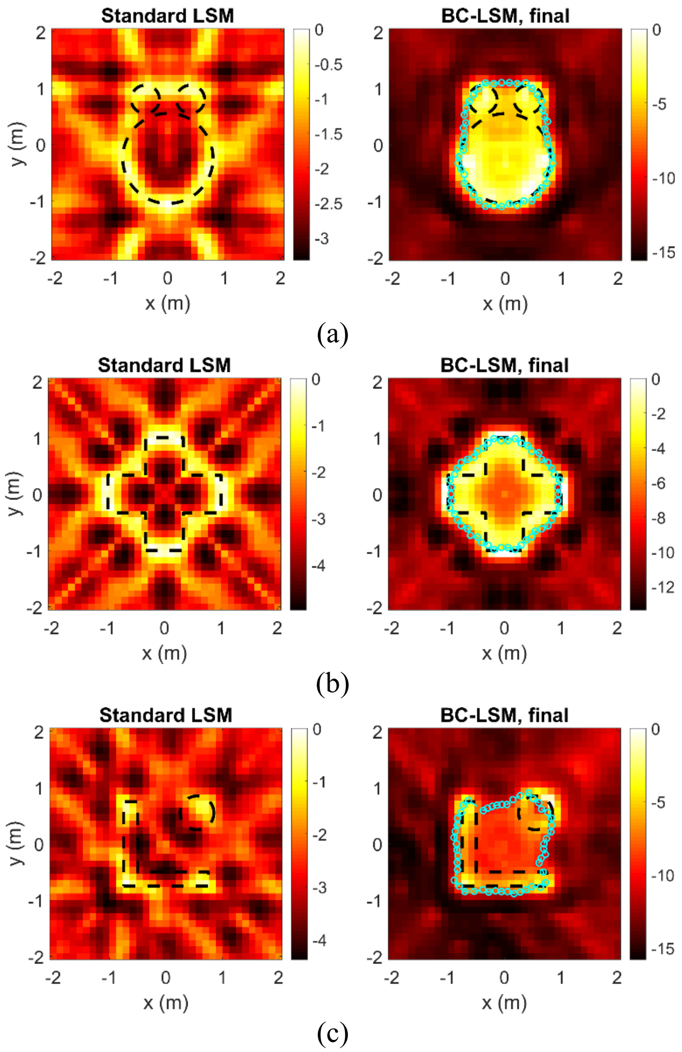

Fig. 26—Image results for three complex targets from synthetic data. For each case, the left image is the result from standard LSM and the right image is the final result after applying the multiple-$\beta$ procedure for the BC-LSM. (a) The Austria-type target. (b) The cross target. (c) The L and disc disconnected targets. The color bars and blue circles have the same meaning as in Fig. 20.

After obtaining the converged boundaries, we select the final $\beta$ for image formation using the image norm ratio step via Eq. (20). The resulting final $\log\beta$ for BC-LSM image formation with the converged boundary is $-2, -3,$ and $-3$ for the Austria, cross, and L-and-disc scenes, respectively.

The resulting BC-LSM images are clearly of improved quality compared to the standard LSM images. In each case, the artifacts distributed throughout the standard imagery have been greatly reduced. The regions of high indicator are concentrated within the true target boundaries and closely approximate the true target shapes. This is true even though the boundary estimates imperfectly capture the non-convexities in the targets. This is especially true for the L-and-disc scene, in which each individual scatterer is faithfully reconstructed while the space between the scatterers is assigned a lower indicator value. These results demonstrate that the BC-LSM penalty provides a useful constraint to the LSM solution even when only the outermost target boundaries are well-estimated.

### *4.3.7 Experimental Results: Manitoba Data Set*

Next, we consider the performance of the BC-LSM technique using experimental data. First, we use the publicly available experimental dataset from the University of Manitoba [82]. The Manitoba dataset was generated using a two-dimensional array of 24 Vivaldi antennas uniformly distributed on a circle of approximate radius 22.4 cm. Two conducting targets are available in the form of conducting pipes of diameters 2 and 3.5 inches. In this paper, we image the 2-inch pipe data.

To image the conducting pipe data via BC-LSM, we must calculate the incident fields on the estimated target boundary. However, the incident fields in the imaging region arising from the Vivaldi antennas are unknown *a priori*. We overcome this challenge using a simple calibration procedure described below.

We first simulate a data collection with a calibration target using FDTD as described previously. As the 2-inch pipe is the imaging target, we choose the 3.5-inch pipe to be the calibration target. We do not model the Vivaldi antennas, but instead replace them with elementary current sources. We collect the multistatic electric field phasors for all transmit-receive pairs. For each pair, we compute the calibration factor $\gamma = S_{\text{meas,cal}}/E_{\text{sim}}$, where $S_{\text{meas,cal}}$ is the scattered signal measurement for the calibration target and $E_{\text{sim}}$ is the corresponding simulated scattered field phasor.

We then calculate the average $\gamma$ across all multistatic pairs. We discard all but four of the receive channels while keeping all transmit channels, resulting in sparse-receive dense-transmit data of size $4 \times 24$. We then apply the calibration procedure and apply the multiple-$\beta$ reconstruction strategy to the calibrated data. We reconstruct the target on a domain of size $0.1 \times 0.1$ m with a grid of dimension $50 \times 50$ cells. We use frequencies 3.0, 3.5, 4.0, 4.5, and 5.0 GHz. We once again use 50 boundary points and distribute their initial locations on circular boundaries. We set the boundary perturbation step size to 0.5 cm.

Lastly, we apply the calibration factor to the measured imaging target data such that $E_{\text{corrected}} = S_{\text{meas,test}}/\gamma_{\text{mean}}$, where $S_{\text{meas,test}}$ is the measured signal for the target to be imaged and $E_{\text{corrected}}$ is the electric field phasor resulting from applying the calibration. This calibration procedure is similar to the one described in [82], with the exception that we apply the same mean calibration factor to all channels, whereas in [82] it is suggested to apply calibration factors on a channel-by-channel basis.

We then apply the BC-LSM algorithm using the $E_{\text{corrected}}$ phasors as the measured scattered field data at the antennas. We once again use the Green's function between each transmit location and boundary point to form $\mathbf{E}_{\text{i}}^{\partial U}(k)$ in Eq. (18). Applying the mean calibration factor to all measured channels ensures that the scattered field data and the boundary incident field data are on equivalent scales.

The residual function curves are shown in Fig. 27(a). The set of curves is similar to Fig. 19 in that $\log \beta = -6$ is associated with the most favorable residual functions with well-separated and deep local minima. Once again, lower $\beta$ leads to slowly decreasing residual functions and higher $\beta$ leads to unsmooth functions with many closely spaced local minima. We therefore select $\log \beta = -6$ for the boundary optimization. We initialize the optimization using a circular boundary of radius 4 cm, which is at the edge of the convex region surrounding the lowest local minimum. We initialize the boundary at the edge of the convex region in order to provide a more challenging demonstration for this geometrically less complex target.

The standard LSM reconstruction is shown in Fig. 27(b). The standard reconstructions is of poor quality, with many artifacts distributed throughout the image.

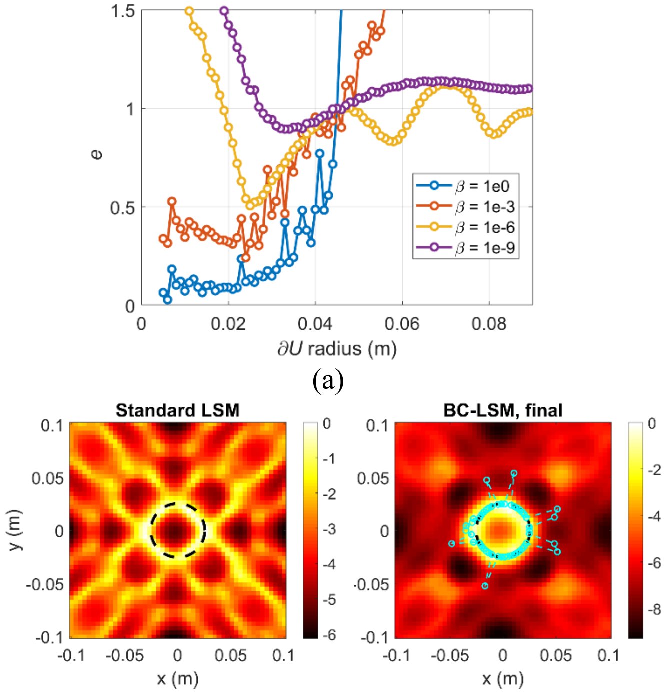

(a)

(b) (c)

Fig. 27—Experimental results for the 2.0-inch conducting pipe from the Manitoba data set. (a) The residual function curve. The curves are normalized to their values at a radius of 4.5 cm. (b) The standard LSM image. (c) The converged BC-LSM image created with the multiple-$\beta$ reconstruction strategy. The color bars and blue circles have the same meaning as in Fig. 20.

The converged BC-LSM reconstruction is shown in Fig. 27(c). The converged estimated boundary is a good match to the true target shape and size, with a handful of outlier boundary points. The image norm ratio procedure produces an optimum final $\log\beta = -5$. The resulting BC-LSM imagery is of much improved quality compared to the standard LSM imagery. The vast majority of the artifacts outside the target boundary have been mitigated, and the interior of the target reconstruction is more consistently filled in.

### *4.3.8 Experimental Results: Fresnel Data Set*

Next, we perform BC-LSM imaging using the publicly available dataset from the Fresnel Institute [83]. The Fresnel data is a two-dimensional dataset with 36 transmit locations and 72 receive locations. We choose to image the conducting U-shaped target. We calibrate the data in the same manner as in the previous subsection. We choose the non-centered conducting rectangle as the calibration target.

We again downsample the receive aperture to achieve a sparse-receive dataset. We keep five receive locations. Since the Fresnel data does not include receive data for 60° arcs around the monostatic direction, this results in four receive channels for each transmitter. We again reconstruct the target on a $0.1 \times 0.1$ m, $50 \times 50$ cell grid. We use frequencies 2, 4, 6, 8, and 10 GHz. We use 50 boundary points and set the perturbation distance to 0.5 cm.

The residual function plot is shown in Fig. 28(a). In this case, only the $\log\beta = -9$ curve is free of

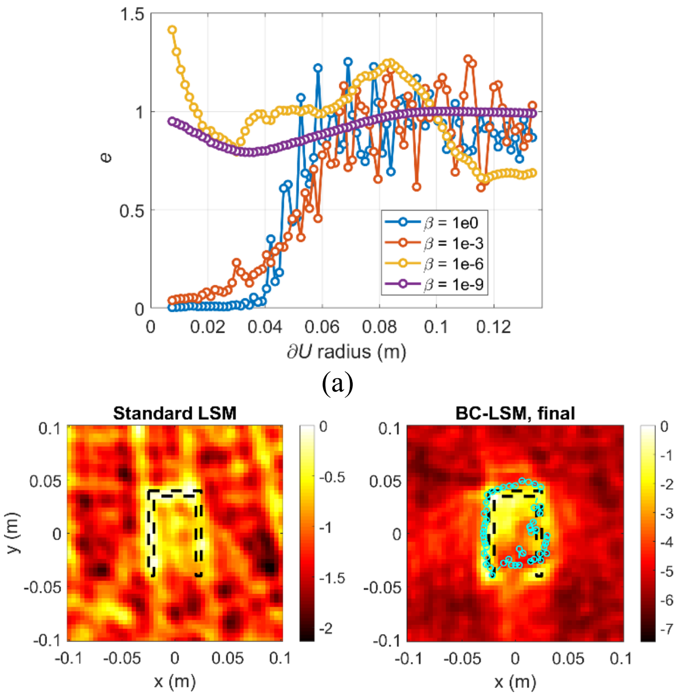

(a)

(b)

(c)

Fig. 28—Experimental results for the U-shaped target from the Fresnel dataset. (a) The residual function curve. The curves are normalized to their values at a radius of 10 cm. (b) The standard LSM image. (c) The converged BC-LSM image created with the multiple-$\beta$ reconstruction strategy. The color bars and blue circles have the same meaning as in Fig. 20.

closely spaced local minima, and thus we choose this value of boundary optimization, despite the fact that the corresponding minimum is not particularly deep as desired. We initialize the estimated boundary radius to 6.0 cm and perform a multiple-$\beta$ reconstruction. The image norm ratio procedure in this cases produces an optimum final regularization value of $\log \beta = -4$.

The standard and BC-LSM image results are shown in Fig. 28(b) and (c), respectively. The standard LSM image is a poor reconstruction with many artifacts. The converged BC-LSM estimated boundary is a reasonable estimate to the true target shape. The converged BC-LSM image is of superior quality to the standard reconstruction, as the artifacts have been mitigated and the overall size and shape of the region of high image value is a good match to the target. The non-convexity is partially apparent in the estimated boundary and more apparent in the image. This is notable, as the non-convexity is typically the most challenging feature to reconstruct for this target.

### *4.3.9 Limited-Aspect Examples*

We now consider sparse-receiver scenarios where both the transmit and receive apertures are limited in aspect. We first consider a simulated-data example using the kite target. We distribute 11 transmit locations and three receive locations across a 150° arc centered on the +*y*-axis, as illustrated in Fig. 29(a). We then perform a multiple-$\beta$ reconstruction at 100, 125, and 150 MHz. We initially distribute 25 boundary

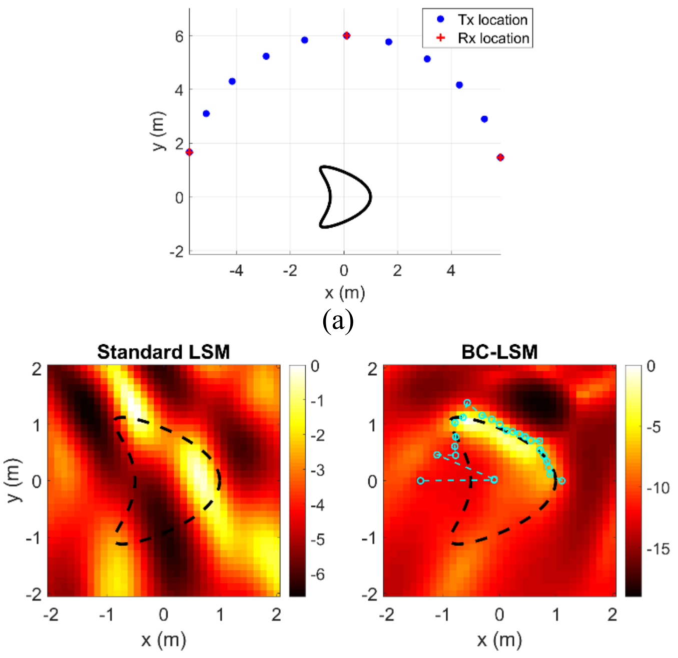

(a)

(b) (c)

Fig. 29—A limited-aspect, sparse-receive example from simulated data. (a) The imaging scenario. (b) The standard Tikhonov-regularized LSM reconstruction. (c) The BC-LSM reconstruction.

points on a 180° arc of radius 1.3 m centered on the +$y$-axis. Our rationale for this choice of initial boundary is that the received data will mostly contain information from the portion of the target illuminated by the sensors, and thus having boundary points along the non-illuminated portions of the target would be unhelpful. We slightly modify the LSM equation to be solved to $\mathbf{E}_s(k)\mathbf{g}(k,\mathbf{r}) = \mathbf{\Phi}(k,\mathbf{r})/\|\mathbf{\Phi}(k,\mathbf{r})\|$. Normalizing the right-hand side of the equation in this way has been shown to improve limited-aspect LSM performance in previous work [7].

The resulting standard and BC-LSM reconstructions are shown in Fig. 29(b) and (c), respectively. The standard LSM results are of low fidelity. The BC-LSM boundary estimation accurately captures the target surface facing the sensors. The resulting BC-LSM reconstruction also faithfully captures the geometry of the target surface facing the sensors.

Next, we perform a limited-aspect reconstruction from experimental data using the Manitoba 2-inch pipe target. Similarly to the limited-aspect kite example, we discard all channels except for those corresponding to 10 transmit locations and three receive locations uniformly distributed along a 150° arc. We initially distribute the boundary points along a 4-cm arc, but limit the arc to 25 boundary points across a 180° span. The results are shown in Fig. 30. The standard LSM image in Fig. 30(a) is of very low fidelity. The BC-LSM estimated boundary and reconstruction in Fig. 30(b) are of high fidelity to the target surface facing the sensors.

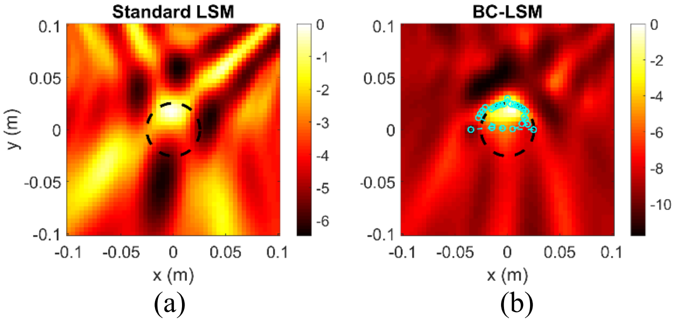

(a) (b)

Fig. 30—A limited-aspect, sparse-receive experimental example from the Manitoba data set. (a) The standard Tikhonov-regularized LSM reconstruction. (b) The BC-LSM reconstruction.

### *4.3.10 Quantification of Reconstruction Accuracy*

Lastly, we provide quantitative metrics of reconstruction accuracy for a subset of the results in previous sections. While the BC-LSM results reported in this study evince clear visual improvement relative to the standard Tikhonov-regularized results, we can achieve additional confidence in our subjective judgements of image quality by using a quantitative measure of fidelity.

We choose to quantify image fidelity using the Jaccard index, which has been used in previous qualitative inverse scattering studies (e.g., [84,85]). We threshold each image and compute the ratio

$$J = \frac{\text{Thresolded image } \cap \text{ True target footprint}}{\text{Thresholded image } \cup \text{ True target footprint}}. \tag{22}$$

Using this index, a perfect reconstruction results in $J = 1$.

We plot the results for several examples from this study in Fig. 31, including the simulated kite example, the three complex target simulated examples, the experimental example from the Manitoba dataset, and the experimental example from the Fresnel data set. In each case, we plot $J$ for both the BC-LSM and the standard Tikhonov-regularized LSM as a function of the threshold parameter $\nu$ from Eq. (21).

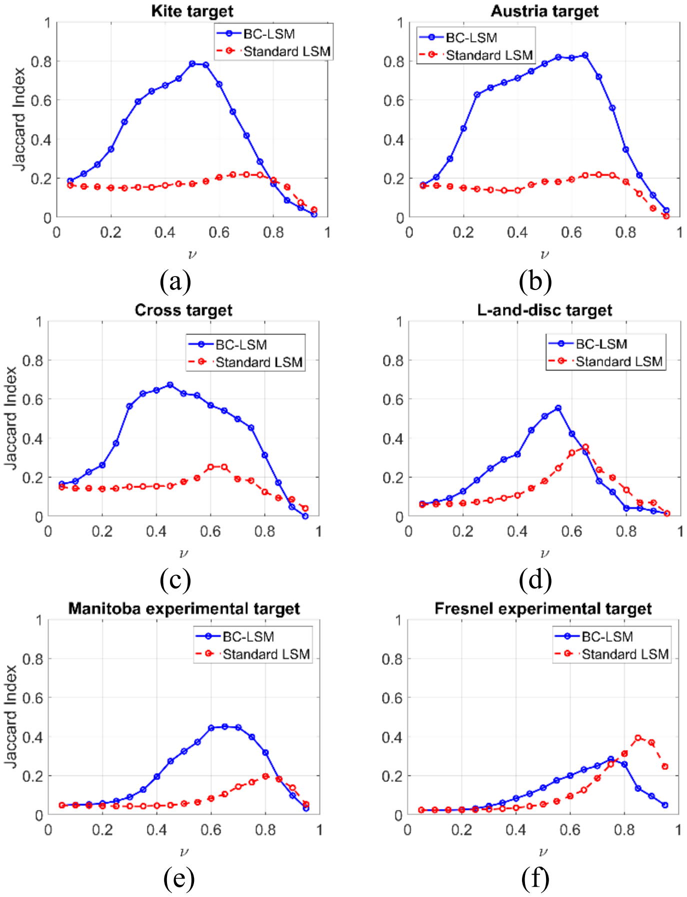

(a) (b) (c) (d) (e) (f)

Fig. 31—The Jaccard index versus the threshold parameter for various BC-LSM and standard LSM reconstructions. (a) The simulated kite. (b-d) The simulated complex targets. (e) The experimental Manitoba example. (f) The experimental Fresnel example.

In six out of the seven examples, the BC-LSM clearly outperforms the standard LSM according to the quantitative metric. The metric for the example in Fig. 31(f), the Fresnel experimental example, is more ambiguous. The standard LSM reconstruction outperforms the BC-LSM reconstruction for this example only for very high values of $\nu$ which mask out the wide distribution of artifacts in the standard LSM image. Both the BC-LSM and standard LSM results have a relatively low peak $J$. This is because the walls of the U-shaped target from the Fresnel dataset are thin compared to the apparent resolution of the imaging techniques, and thus there are many thresholded pixels outside the true target footprint even when artifacts have been minimized, as in the BC-LSM reconstruction from Fig. 28(c). Overall, the Jaccard index results are consistent with our visual judgements that the BC-LSM technique results in significantly improved image fidelity.

### *4.3.11 Discussion*

The results in this study demonstrate that the proposed BC-LSM method generates high-fidelity imaging results across a wide variety of sparse-receiver imaging scenarios. The BC-LSM's improvement in these scenarios compared to the standard Tikhonov-regularized LSM is clear and consistent.

The results also demonstrate properties of the BC-LSM that could make it potentially advantageous compared to non-LSM-based conducting-target imaging techniques in some scenarios. Unlike techniques that output only the target image, the BC-LSM also outputs additional target information that can aid in image interpretation, namely the estimated boundary as well as the solution's target-dependent resonant frequency information. Generating the target image via a qualitative inverse scattering approach is an ill-posed process, and thus it is reasonable to expect that even high-fidelity reconstructions will be imperfect and present some degree of visual ambiguity. Thus, these auxiliary sources of target information are of interest.

Several examples from this study demonstrate how the estimated boundary could serve as an additional visual cue for image interpretation. Regions of high indicator value that appear exterior to the estimated boundary, as in Fig. 27(c), may in some cases be provisionally discounted as artifacts. Consistency between the BC-LSM image and the boundary estimate may provide additional confidence that the appearance of a hard-to-resolve feature in the reconstruction, such as the cavity in Fig. 28(c), represents a true feature and not an artifact. Target structure information observable from the boundary estimate may also be especially valuable in cases where image quality is limited by noise, as in the 0 dB SNR example from Fig. 22.

The results of this study also suggest a path of future research into leveraging the BC-LSM resonant frequency response for aid in image interpretation or target recognition. Fig. 24 demonstrates the close match between the observed and expected target-dependent resonant frequencies for the lowest three resonances (especially for the scenario in Fig. 24(b) with more sensors). Thus, improved confidence in target identification could potentially be achieved if a good match is found between not only the reconstruction and the expected target footprint, but also simultaneously the observed and expected spectrum of resonances. More advanced schemes could potentially be formulated that use the observed resonances, the estimated boundary, and geometrical information from the imagery as features for automatic target recognition.

### 4.4 Conclusion

In this section, we formulated and investigated a boundary-condition-enhanced linear sampling method (BC-LSM) formulation for imaging conducting targets from sparse receive data. Based on the perspective of the LSM as a transmit beamforming operation, the technique places constraints on the LSM solution in order to enforce electric field boundary conditions on an estimate of the target boundary. The boundary condition constraints discipline the LSM solution in order to mitigate the lack of channels in the receive aperture. Using simulated datasets, we demonstrated efficacy of the BC-LSM method and formulated strategies for choosing optimization parameters to achieve consistent results. We demonstrated the effects of noise, conductivity, and target resonances. We further validated performance by applying the BC-LSM to experimental data from publicly available datasets. The results from both simulated and experimental data show that the proposed technique significantly improves imaging performance over standard LSM imaging when the receive aperture is sparse

## 5. RECEIVE-BEAMFORMING-ENHANCED LINEAR SAMPLING METHOD IMAGING

This section is adapted in part from a paper previously published in conference proceedings [36].

### 5.1 Background

In this section, we study the effects of performing a receive beamforming operation on the scattered field prior to solving the LSM system of equations. We hypothesize that the decrease of dimensionality of the LSM system resulting from beamforming may benefit imaging performance from a sparse or limited-aspect set of sensors. Beamforming enhancements to quantitative inverse scattering techniques (which, unlike qualitative techniques such as the LSM, reconstruct target material parameters as well as shape) have previously been introduced for the purpose of improving noise performance or lowering computational complexity [86, 87].

In the following subsections, we first present the mathematical formulation of the beamforming-enhanced LSM under two different regularization frameworks — namely, conventional Tikhonov regularization and a phase-delay frequency variation (PDFV) regularization we have previously introduced for sparse-aperture imaging [31]. We then provide an imaging demonstration of data from a simulation of a challenging limited-aperture, sparse-receiver scenario.

## 5.2 Imaging Formulation and Analysis

We assume two-dimensional transverse magnetic propagation. A collection of $N_{\text{tx}}$ transmitters and $N_{\text{rec}}$ receivers are placed around an unknown target. The scattered electric field phasors for every transmit-receive pair are collected in the $N_{\text{rec}} \times N_{\text{tx}}$ matrix $\mathbf{E}_s$. For a pixel location **r**, conventional LSM imaging is performed by finding the solution **g** to the system of equations

$$\mathbf{E}_{\text{s}}\mathbf{g}(\mathbf{r}) = \boldsymbol{\Phi}(\mathbf{r})\ , \tag{23}$$

where $\boldsymbol{\Phi}(\mathbf{r})$ is the $N_{\text{rec}} \times 1$ vectors of Green's functions relating **r** to each receive location.

We modify the formulation in Eq. (23) by multiplying each side by $\boldsymbol{\Phi}^{\text{H}}(\mathbf{r})$, resulting in

$$\mathbf{e}^{\text{H}}\mathbf{g}(\mathbf{r}) = ||\boldsymbol{\Phi}(\mathbf{r})||^2, \tag{24}$$

where $\mathbf{e}^{\text{H}} = \boldsymbol{\Phi}^{\text{H}}\mathbf{E}_{\text{s}}$. Clearly, $\mathbf{e}^{\text{H}}$ can be seen as the $1 \times N_{\text{tx}}$vector resulting from applying receive beamforming weights $\boldsymbol{\Phi}(\mathbf{r})$ to the multistatic data matrix.

Regularization is typically used to overcome challenges related to the ill-posed nature of the LSM imaging problem. We first consider the effects of commonly used Tikhonov regularization. The Tikhonov regularized solution to Eq. (24) may be written as

$$\mathbf{g}(\mathbf{r}) = \left(\mathbf{e}\mathbf{e}^{\text{H}} + \alpha\mathbf{I}\right)^{-1}\mathbf{e}||\boldsymbol{\Phi}(\mathbf{r})||^2, \tag{25}$$

where **I** is the identity matrix and $\alpha$ is a regularization parameter. Using the Sherman-Morrison formula for a matrix inverse, it can be shown that Eq. (25) reduces to

$$\mathbf{g}(\mathbf{r}) = \left(\frac{\mathbf{e}}{\alpha + ||\mathbf{e}||^2}\right)||\boldsymbol{\Phi}(\mathbf{r})||^2. \tag{26}$$

If we assume that $\alpha$ is chosen to be small relative to $||\mathbf{e}||$, then we can approximate the indicator function as

$$I(\mathbf{r}) \approx \frac{||\mathbf{e}||}{||\boldsymbol{\Phi}(\mathbf{r})||^2}. \tag{27}$$

Thus, under a Tikhonov-regularized framework, the indicator function is dominated by the correlation between the signal and the Green's function. This correlation function may not fully leverage the available target scattering information in some cases.

Next, we consider an alternative regularization technique with the goal of extracting richer target information. We implement into the beamforming-enhanced LSM the phase-delay frequency variation (PDFV) constraint we have previously introduced to improve sparse-aperture LSM imaging [31]. The PDFV regularization stabilizes the LSM solution by enforcing a constraint on the change of the phase of the solution according to the assumed electrical path length of the incident wave. The PDFV-regularized problem statement for the beamforming-enhanced LSM is written:

$$\min_{\mathbf{g}(k,\mathbf{r})} \sum_k \begin{matrix} \left|\mathbf{e}^{\mathrm{H}}\mathbf{g}(k,\mathbf{r}) - \|\boldsymbol{\Phi}(\mathbf{r})\|^2\right|^2 + \alpha\|\mathbf{g}(k,\mathbf{r})\|^2 \\ + \beta D^2(k,\mathbf{r}) \end{matrix}, \tag{28}$$

where $k$ is the wavenumber, the sum is over all collected wavenumbers, $\beta$ is a regularization parameter, and

$$D(k,\mathbf{r}) = \|\mathbf{g}(k,\mathbf{r}) - \mathbf{g}(k+\Delta k,\mathbf{r}) \odot \exp(j\Delta k\mathbf{d})\|. \tag{29}$$

In Eq. (29), $\Delta k$ is a small wavenumber step between adjacent frequencies and $\mathbf{d}$ is the $N_{\mathrm{tx}} \times 1$ vector of distances between **r** and each transmitter.

### 5.3 Imaging Results: Limited Aspect, Sparse-Receive Scenario

We generate scattered field data using the two-dimensional finite-difference time-domain (FDTD) method. A layout of the simulation domain is given in Fig. 32(a). We place three discs in a triangular formation in the domain and assign them an electrical conductivity similar to copper ($5.7 \times 10^7$ S/m). We distribute 31 transmit locations and five receive locations on a 90° arc of radius 6 m, thereby creating a challenging limited-aspect, sparse receiver geometry.

We obtain electric field phasors for every transmit-receive location pair for 21 frequencies between 100 and 300 MHz. We add Gaussian white noise to the data such that the total signal-to-noise (SNR) ratio is 20 dB. We apply the standard LSM and the beamforming-enhanced LSM with both Tikhonov and PDFV regularization to the data. We generate multi-frequency indicator functions in each case by computing Eq. (4).

The imaging results are shown in Fig. 32(b)-(d). The standard LSM and Tikhonov-regularized beamforming-enhanced LSM fail to faithfully reconstruct the targets. In contrast, PDFV-regularized beamforming-enhanced LSM accurately reconstructs the surfaces of the targets facing the sensors.

Interestingly, the system dimensionality reduction from beamforming (when combined with PDFV regularization) may have stabilized the reconstruction by encouraging a reduction of geometric complexity of the image from cross-sections to partial surfaces. Reconstructing only surfaces in this case is reasonable given the limited target illumination in the limited-aspect geometry.

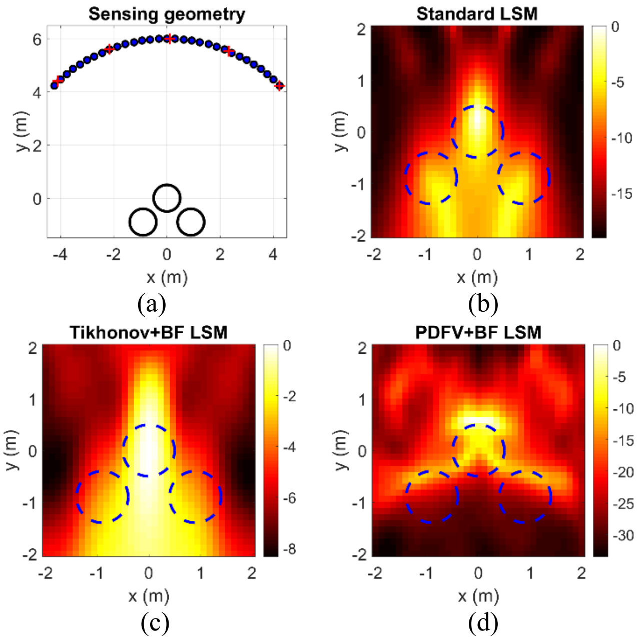

Fig. 32—(a) The layout of the simulated data acquisition. Transmit locations are denoted with circles and receive locations are denoted with cross-hairs. (b) Standard LSM imaging results. (c) Beamforming-enhanced LSM results using Tikhonov regularization. (d) Beamforming-enhanced LSM results using PDFV regularization. In (b)-(d), the color bars denote $\mathbf{20\log \mathit{I}(r)}$, with 0 dB referenced to the most intense pixel and the lower limit determined by the dynamic range of the image.

## 5.4 Imaging Results: Limited Aspect, Synthetic Aperture Scenarios

Next, we generate data and imagery for scenarios that assume only a single transmitter and 5 receivers, as illustrated in Fig. 33a. The sensors are placed in formation with 2-degree spacing. The transmitter is centered in the formation. We assume the formation moves across a 10-m radius, 90° synthetic aperture while taking multistatic data at 1° increments. The scenario is of interest because it would allow for imaging with only five physical sensors while collected many samples in the synthetic aperture, thus creating a data set of significant information diversity with limited resources. We again simulate the scenarios via FDTD. We record the multistatic electric field phasors at 6 frequencies between 1.5 and 1.6 GHz. We again add noise such that the SNR is 20 dB.

To image the data, we structure the data matrix in multidiagonal form as described in [88]. We then apply both the standard LSM and the PDFV-regularized beamforming-enhanced LSM. Imaging results are shown in Fig. 33(b)-(d) for a conducting cross target, a conducting disc target, and the conducting three-disc target formation. The standard LSM fails to faithfully reconstruct the target geometry for both the cross target and the three-disc formation. For the single-disc target, the target response in the standard LSM image is somewhat accurately localized, but the reconstructed target region is inaccurate in shape and size. Conversely, the beamforming-enhanced LSM with PDFV regularization accurately reconstructs the surfaces of the targets facing the synthetic aperture in all cases.

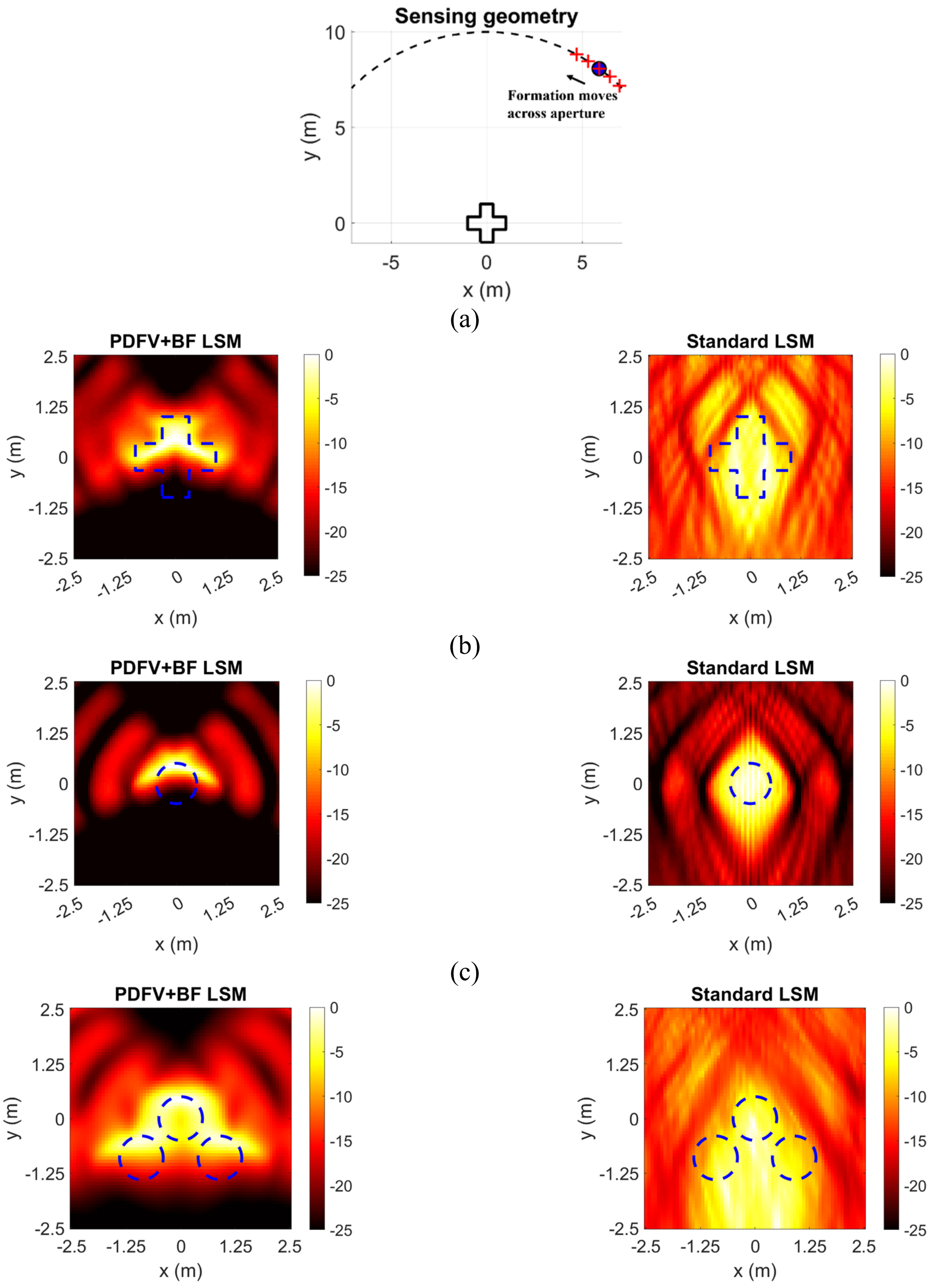

(a)

(b)

(c)

(d)

Fig. 33—(a) The layout of the sensing geometry for a synthetic-aperture-radar-style scenario. The transmitter is denoted with the circle and the receivers are denoted with cross-hairs. The sensor spacing is exaggerated for the purposes of visualization. The sensor formation moves across the synthetic aperture while taking data. (b) Imaging results for a conducting cross target. (c) Imaging results for a conducting disc target. (d) Imaging results for a three-disc target. In (b)-(d), the color bars denote $20 \log I(\mathrm{r})$, with 0 dB referenced to the most intense pixel and the lower limit set to -25 dB.

### 5.5 Conclusion

We presented a study of the effects of a beamforming-enhanced linear sampling method for imaging from sparse or limited-aspect sensor distributions. We presented the formulation of the beamforming enhancement under two regularization frameworks. We then demonstrated imaging performance using limited-aspect datasets. The results demonstrated successful reconstruction of the target surfaces facing the sensors when the technique is regularized with a phase delay constraint. The promising results motivate further study.

## 6. MACHINE LEARNING FOR EXTRACTING TARGET ELECTRICAL PARAMETERS FROM QUALITATIVE INVERSE SCATTERING IMAGERY

This section is adapted from a paper published in conference proceedings [34].

### 6.1 Background

An emerging area of investigation is to use the behavior of the LSM solution vector to extract not only target shape, but also other target characteristics. Various studies have explored the frequency behavior of the norm of the LSM solution in order to use the target resonance spectrum (i.e., transmission eigenvalues) for, e.g., target type classification, target void detection, and target dielectric properties characterization[78-80]. The phase of the solution has received much less attention, even though the phase of the transmit beamforming weight is clearly a function of the target scattering characteristics and may therefore have exploitable information embedded within it.

In this section, we introduce and evaluate a machine-learning-based strategy to exploit the phase of the LSM solution to classify targets according to their constituent dielectric properties. We generate simulated scattered field data for a variety of target shapes and sizes. We image the data using the LSM and then use the phase of the resulting solutions to build training vectors for a support vector machine (SVM). We then apply the SVM to separately generated testing data to classify targets as being composed of either low dielectric or highly conducting materials. In this way, we use qualitative inverse scattering imagery to extract quantitative target information.

Previous studies have explored alternate strategies for using machine learning to extract dielectric properties information from scattered fields. In some [89, 90], the machine learning algorithm is applied directly to the scattered field data. However, this strategy would fail if there are multiple scatterers in the scene with large differences in dielectric properties, assuming that the training data is generated only for single scatterers. Our proposed approach is advantageous in that the SVM can be applied only to image pixels that compose the identified target of interest. We will show that this strategy allows us to isolate the scattering contributions from interference from other scatterers in the scene. Applying the machine learning strategy to imagery as opposed to raw data is therefore a critical step, as in many practical target imaging scenarios we should expect unwanted scatterers to be in the vicinity of the target.

Previous studies have also explored using machine learning to enhance the imaging capabilities of quantitative inverse scattering techniques [91-94] Our work here is distinct in that it makes use of the advantages of qualitative over quantitative inverse scattering approaches, namely the ease of algorithmic implementation, and the lower computational expense.

## 6.2 Method

We once again assume an LSM imaging problem in the form of Eq. (3). For consistency with the published conference paper, we use $\omega$ to denote frequency in this section, whereas in previous sections, we used $k$.

We assume a matrix of training data $\mathbf{A} = [\mathbf{a}_1, \mathbf{a}_2, \ldots, \mathbf{a}_{N_\mathrm{v}}]$, where $\mathbf{a}_i$ is the $i$th training vector and $N_\mathrm{v}$ is the number of training vectors. Each vector corresponds to a training data acquisition where a single target is placed in the imaging domain. The vector of training labels is denoted **b**. Its $i$th entry is +1 for a dielectric target and –1 for a conducting target.

The $i$th training vector is defined as

$$\mathbf{a}_i = \left[\angle\mathbf{g}^\mathrm{T}(\mathbf{r}_{i1}, \omega_1), \ldots \angle\mathbf{g}^\mathrm{T}\left(\mathbf{r}_{iN_\mathrm{p}}, \omega_1\right), \angle\mathbf{g}^\mathrm{T}(\mathbf{r}_{i1}, \omega_2), \ldots, \angle\mathbf{g}^\mathrm{T}\left(\mathbf{r}_{iN_p}, \omega_{N_\mathrm{f}}\right), \mathbf{d}^\mathrm{T}(\mathbf{r}_{i1}), \ldots \mathbf{d}^\mathrm{T}\left(\mathbf{r}_{iN_\mathrm{p}}\right)\right]^\mathrm{T}, \tag{30}$$

where $\mathbf{r}_{ij}$ is the $j$th LSM image pixel selected for the $i$th training sample, $N_\mathrm{p}$ is the number of image pixels to train with, $\omega_k$ is the $k$th data acquisition frequency, $\angle\mathbf{g}(\mathbf{r}_{ij}, \omega_k)$ is the $N_\mathrm{tx} \times 1$ vector of phases of the LSM solution for pixel $\mathbf{r}_{ij}$ and frequency $\omega_k$, and $\mathbf{d}(\mathbf{r}_{ij})$ is the $N_\mathrm{tx} \times 1$ vector of distances between each transmit location and $\mathbf{r}_{ij}$. We include $\mathbf{d}(\mathbf{r}_{ij})$ in the training vector on the expectation that the phase of the LSM solution will be related to the electric length, and therefore propagation distance, traversed by the incident wave to the pixel of interest. We denote the length of each training vector as

$$L = N_\mathrm{tx} N_\mathrm{p} (N_\mathrm{f} + 1). \tag{31}$$

We use a linear SVM training algorithm with **A** to generate classifier weights **w** and $w_0$, where **w** is of size $L \times 1$ and $w_0$ is a scalar. We choose the method of sequential minimal optimization [95] for this purpose. Given a test vector $\mathbf{a}_\mathrm{test}$ generated in the same form as given in Eq. (30) for a target of unknown electrical properties, we then compute the quantity $b_\mathrm{test} = \mathbf{w}^\mathrm{T}\mathbf{a}_\mathrm{test} + w_0$. If $b_\mathrm{test} > 0$, the unknown target is classified as a dielectric, and if $b_\mathrm{test} \leq 0$, the target is classified as conducting.

## 6.3 Procedure for Technique Evaluation

### *6.3.1 Data Generation, LSM Imaging, and Classification Procedure*

The imaging setup is illustrated in Fig. 34. Twenty transmit/receive locations are uniformly distributed along a circular arc of radius 8 m. Within the transmit/receive circle interior is an imaging domain, i.e., the two-dimensional domain over which LSM images are created, of lateral dimension 10.8 m and vertical dimension 4.8 m. Within the imaging domain are two target domains denoted $\Omega_1$ and $\Omega_2$, which are offset from the imaging domain center to the left and right, respectively, by 3 m. Both $\Omega_1$ and $\Omega_2$ are square in shape with side lengths of 4 m.

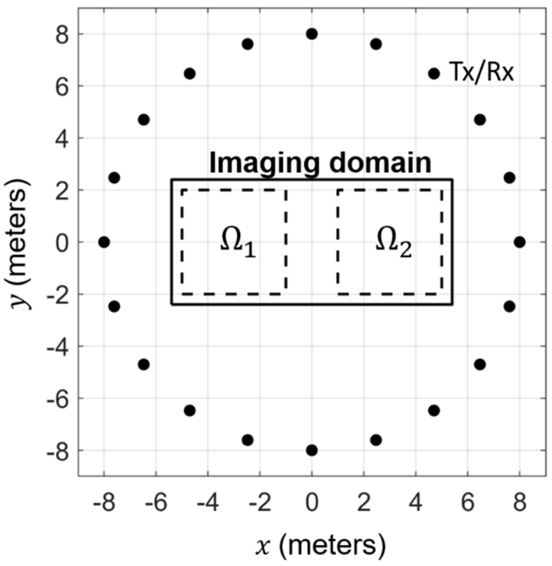

Fig. 34—The imaging setup for generating training and testing data

We generate sets of training vectors in the following manner. For each desired training vector, we place a single target in $\Omega_1$. We then generate scattered field data using two-dimensional transverse magnetic finite-difference time-domain (FDTD) simulations. We place a current source at each transmit location in sequence, feed the current source with a transmit signal in the form of a Gaussian pulse, and record the resulting scattered electric field at each receive location. We then transform the time-domain scattered field data to complex phasor form at 21 frequencies ranging from 50 to 100 MHz using the discrete Fourier transform and populate $\mathbf{E_s}(\omega)$.

We repeat this process to generate 400 training vectors for $\Omega_1$. The target spatial placement in $\Omega_1$ varies randomly between vectors. Depending on the target type under investigation, the target shape or size may also vary randomly, as described in the following subsection. Half of the samples use a lossless target with dielectric constant 2, i.e., a dielectric target, and the other half use a target with electric conductivity of $5.7 \times 10^7$ S/m, i..e, a conducting target. For each training vector, we add Gaussian white noise such that the signal to noise ratio (SNR) is 50 dB and solve for $\mathbf{g}(\mathbf{r}, \omega_k)$ using $\alpha = 10^{-5}$ on a Cartesian grid in the imaging domain with a discretization of 8.1 cm. We then select $\mathbf{g}(\mathbf{r}_{ij}, \omega_k)$ for an $11 \times 11$ grid of pixels $\mathbf{r}_{ij}$ with one-pixel spacing centered on the target location and populate the vector $\mathbf{a}_i$ as in Eq. (30). With $N_{\text{tx}} = 20$, $N_{\text{p}} = 121$, and $N_{\text{f}} = 21$, the length of $\mathbf{a}_i$ is thus $L = 53{,}240$ by Eq. (31).

We repeat the procedure in the preceding two paragraphs to create 400 training vectors for $\Omega_2$. We then create classifier weights $\mathbf{w}_1, w_{01}$ for $\Omega_1$ and $\mathbf{w}_2, w_{02}$ for $\Omega_2$.

We then generate a series of test data samples on the same domain. For each test data sample, we randomly place one dielectric target in $\Omega_1$ and one conducting target in $\Omega_2$. Thus, unlike in the training data, each testing data sample includes two targets of disparate dielectric properties. Using this testing data will evaluate the effectiveness of using LSM imaging prior to application of the SVM in order to isolate signal contributions from multiple targets that interfere with one another in the formation of $\mathbf{E_s}(\omega)$.

We acquire $\mathbf{E_s}(\omega)$ for the test data sample, add noise to achieve a 30 dB SNR, and form separate $\mathbf{g}(\mathbf{r}_{ij}, \omega_k)$ and $\mathbf{a}_{\text{test}}$ vectors for both targets in the same manner as is described above for the training data.

We choose a lower SNR than we used for the training data under the assumption that training data may be controlled better than test data acquired in a practical imaging scenario in the field. We apply $\mathbf{w}_1, w_{01}$ to the test vector for the target in $\Omega_1$ and $\mathbf{w}_2, w_{02}$ to the test vector for the target in $\Omega_2$ and record whether the SVM accurately classified each target. The process is repeated until 50 tests have been performed.

We apply this procedure across multiple training and testing datasets to evaluate the effectiveness of the SVM-based strategy for classification of target electric parameters. The following section describes the simulated data sets we use for this purpose.

### *6.3.2 Target Scenarios*

We evaluate the effectiveness of the proposed SVM-based classification method across four different target scenarios. The scenarios are listed and described in Table 2. Scenarios A and B use discs as the imaging targets. For Scenario A, the discs are of radius 0.5 m for all samples, while for Scenario B, the radii of the discs vary randomly from sample to sample with a uniform distribution ranging from 0.25 to 0.5 m.

Table 2—Descriptions of Target Scenarios Used to Generate Test Data

| **Target Scenario** | **Description** |
|---|---|
| Scenario A | Discs of radius 0.5 m |
| Scenario B | Discs with radii ranging from 0.25 to 0.5 m |
| Scenario C | Train: complex targets 1-6<br>Test: complex targets 1-6 |
| Scenario D | Train: complex targets 1-3<br>Test: complex targets 4-6 |

Scenarios C and D use the set of six complex target shapes pictured in Fig. 35. In both cases, the target used for testing and training vector is selected randomly from this set. For Scenario C, both the training and testing data sets use all six targets, while in Scenario D, the training data sets use only targets 1 through 3 and the testing data sets use only targets 4 through 6.

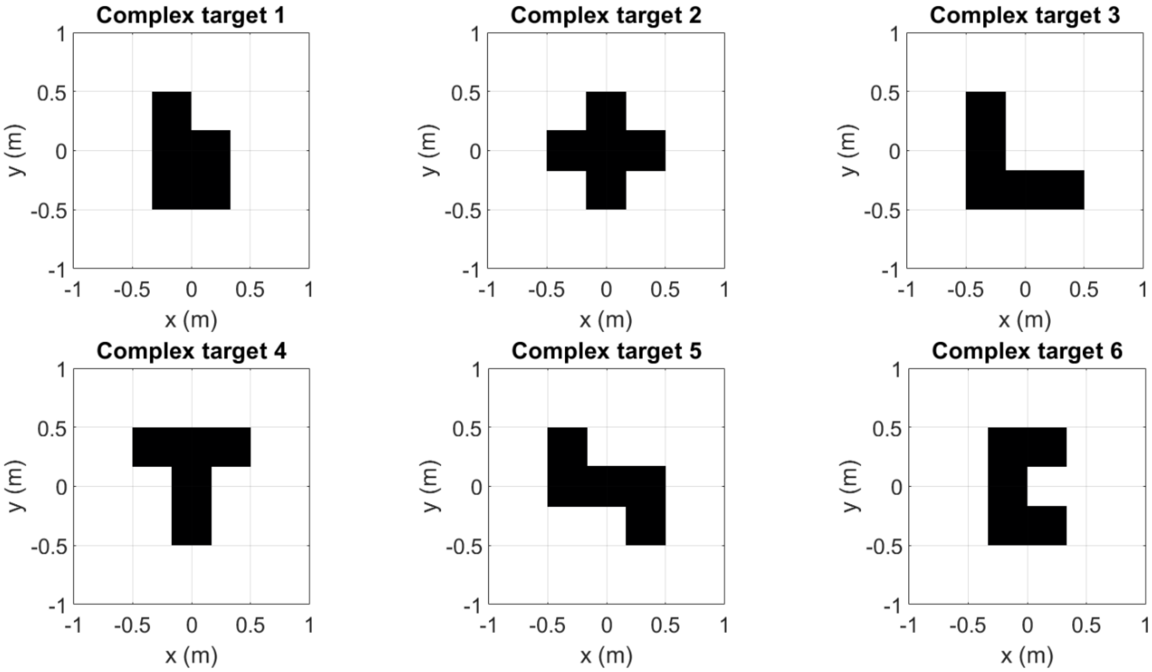

Fig. 35—Complex targets used for Scenarios C and D

## 6.4 Results and Discussion

### *6.4.1 LSM Imagery*

We first report representative LSM image results for several test cases. Fig. 36(a) shows $20\log I(\mathbf{r})$ for example test data from Scenario B where the dielectric disc on the left side of the image is of radius 44 cm and the conducting disc on the right side of the image is of radius 27 cm. Fig. 36(c) shows a detail view of the conducting target response with $\mathbf{r}_{i1},\ldots,\mathbf{r}_{iN_p}$ overlaid. Fig. 36(b) shows $20\log I(\mathbf{r})$ for example test data from Scenario C where the dielectric target is complex target 3 and the conducting target is complex target 5

In both example images, the target response of the left side of the imaging domain is isolated from the target response on the right side of the imaging domain. This demonstrates that the LSM imaging technique can be used to distinguish pixels belonging to individual targets in the scene for the purpose of building the feature vector $\mathbf{a}_{\text{test}}$.

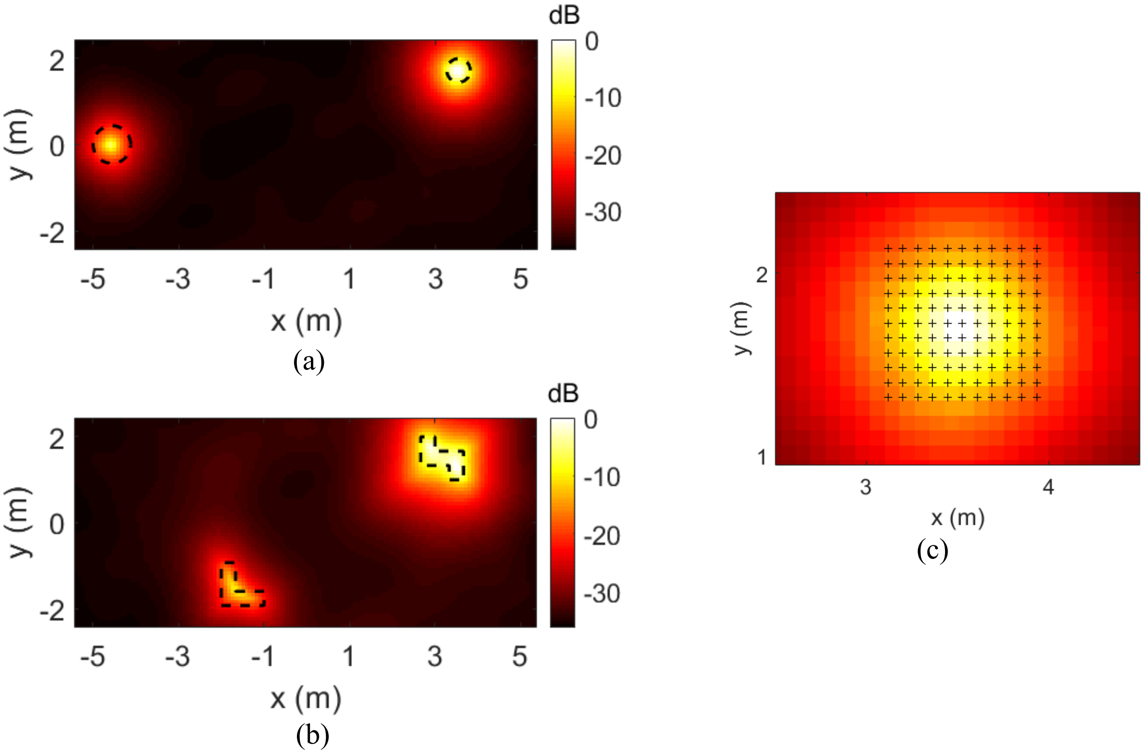

(a)

(b)

(c)

Fig. 36—LSM magnitude images $20\log I(\mathbf{r})$ for (a) Scenario B and (b) Scenario C test examples. In both cases, the target boundaries are denoted with the dashed lines. (c) Detail view of the right (conducting) circular target image, with crosshairs signifying the locations $\mathbf{r}_{i1}, \ldots, \mathbf{r}_{iN_\mathrm{p}}$.

Fig. 37 shows LSM solution phase distributions for example test data from Scenario A. In each case, the phase associated with the transmitter at coordinates $(x,y) = (8,0)$ m at 50 MHz is plotted. There is no clear visually apparent pattern in the phase distributions distinguishing the responses from the dielectric targets on the left side of the domain from the conducting targets on the right side of the domain. In the next subsection, we apply the proposed machine learning technique to determine whether the SVM can discern phase patterns across the data vectors that may not be visually apparent but can nevertheless be used to classify the targets according to their electric parameters.

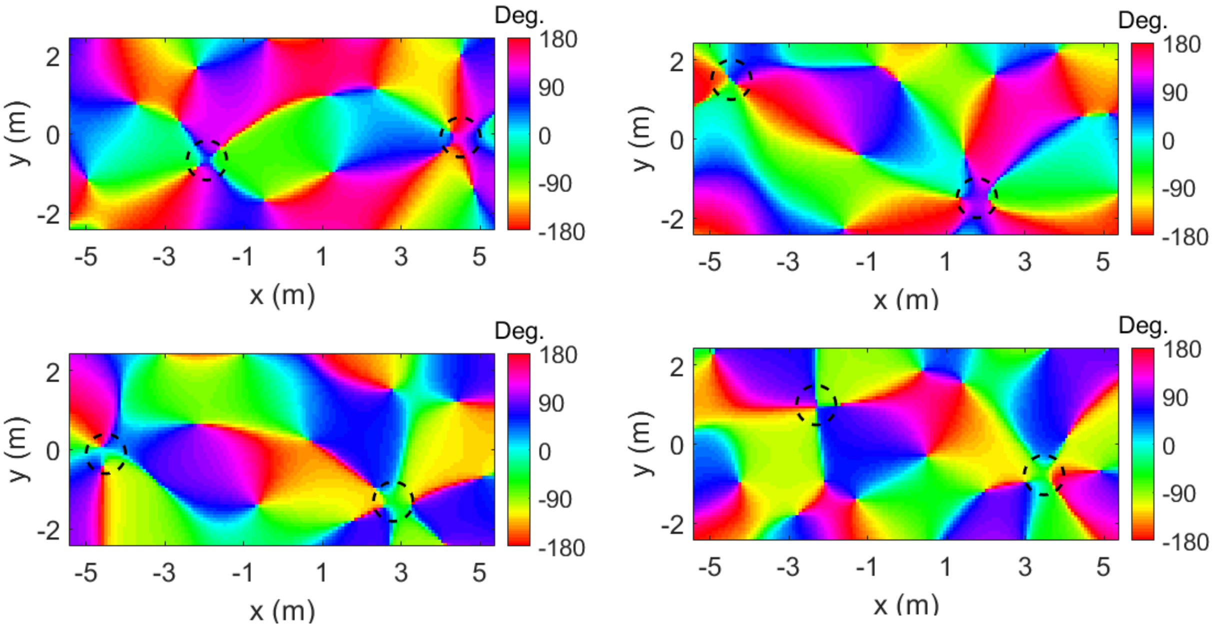

Fig. 37—Four example phase distributions of the LSM solution from the Scenario A test set. The displayed phase is for the transmitter at coordinates (8,0) m and frequency 50 MHz. The dashed lines signify the boundary of the targets.

### *6.4.2 Classification Accuracy*

Fig. 38 displays classification error results for each of the four target scenarios described in Table 2. The classifications errors are plotted against the number of training vectors used to generate $\mathbf{w}_1, w_{01}$ and $\mathbf{w}_2, w_{02}$, ranging from 40 to 400 in steps of 40 vectors. The data points represent means over 10 independently generated noise instances, while the error bars display the maximum and minimum errors over the noise instances. Each plot gives both the classification error recorded after applying the SVM weight vectors to the training data as well as the testing data.

As expected, the classification error is significantly lower when the SVM weights are applied to the training data than when they are applied to the testing data. The training error decreases significantly as the number of training vectors increases from 40. After using around 160 training vectors, the classification error is at or near zero.

The testing classification error also decreases significantly as the number of training vectors increases from 40. The error approaches a minimum around after using 160 or 200 training vectors. The error behaves inconsistently if more than 200 training vectors are added, with significant increases in error and large variances across noise instances occurring in some cases. This inconsistent behavior, along with the observation that the error for the training set converges to near zero for similar numbers of training vectors, suggest that the SVM technique is overfitting for more than 160 to 200 training samples. The results suggest a straightforward heuristic of choosing the appropriate number of training vectors according to convergence of the training classification error.

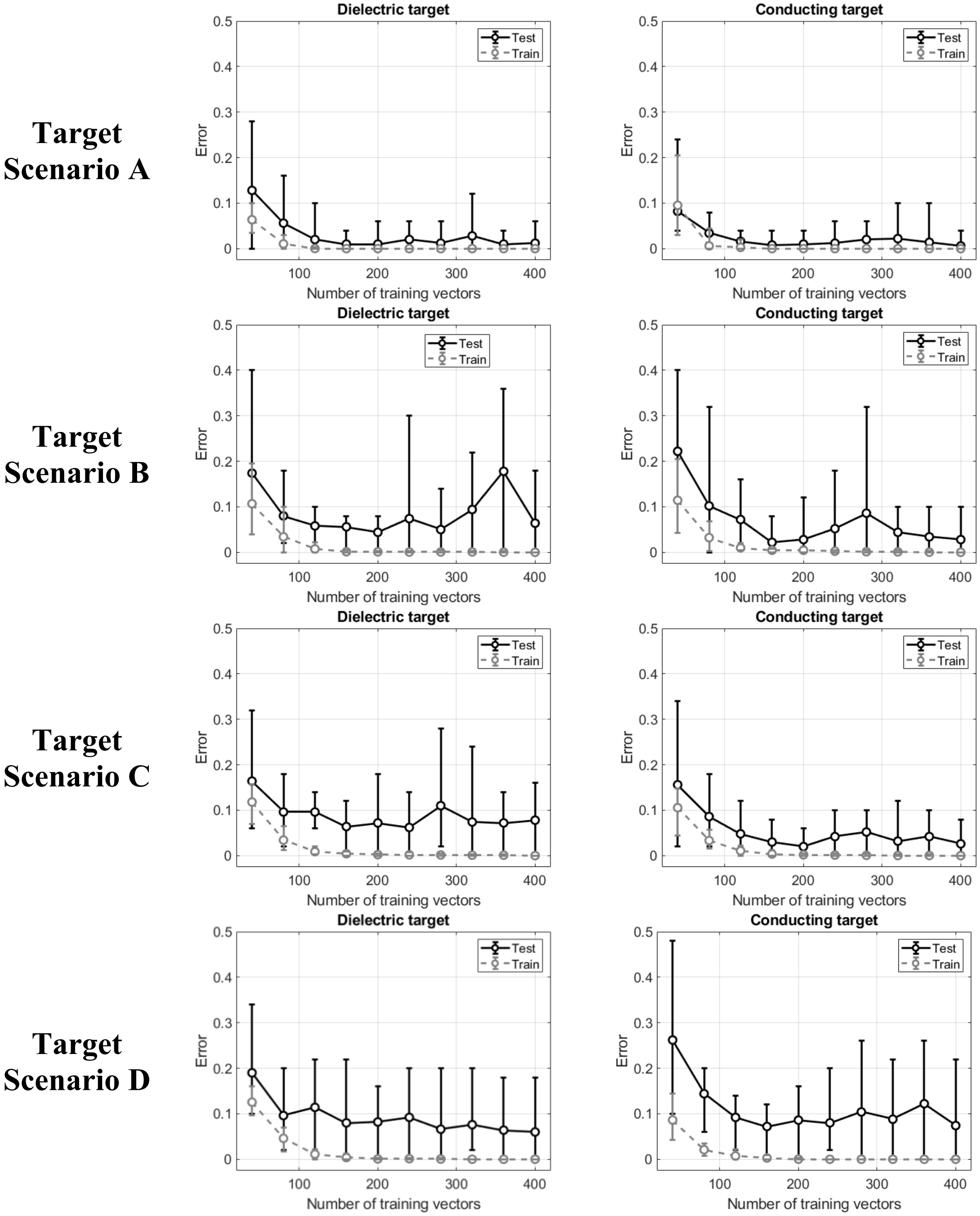

Fig. 38—Classification error vs the number of training vectors used to calculate the SVM for each target scenario. Error results are plotted for application of the SVM to both the training data sets and the testing data sets. Plotted points signify the mean error across 10 noise instances and error bars signify the maximum and minimum errors.

We report the mean testing error rates when using 160 training vectors for each scenario in Table 3.

Table 3—Testing Error Rates for 160 Training Vectors Averaged Across 10 Noise Instances

| **Target Scenario** | **Dielectric Target** | | **Conducting Target** | |
|---|---|---|---|---|
| | $\mathbf{d}(\mathbf{r})$ included in **A** | $\mathbf{d}(\mathbf{r})$ excluded in **A** | $\mathbf{d}(\mathbf{r})$ included in **A** | $\mathbf{d}(\mathbf{r})$ excluded in **A** |
| Scenario A | 1.0% | 1.6% | 0.8% | 1.4% |
| Scenario B | 5.6% | 7.0% | 2.2% | 3.2% |
| Scenario C | 6.4% | 4.4% | 3.0% | 3.8% |
| Scenario D | 8.0% | 7.0% | 7.2% | 11.6% |

We observe the lowest overall testing error for the Target Scenario A data, in which both the target shape and size are constant for all samples. The lowest mean error for this scenario is around 1% for both the dielectric and conducting targets. Testing error rates are higher for the other three scenarios due to the larger degree of target variability the SVM must accommodate. We observe modest error increases for Target Scenarios B and C, where the target size and shape vary between samples, respectively. The mean error for these two cases ranges between approximately 2% and 6%. The worst error is observed for Target Scenario D. This is expected due to the mismatch in target shape between the training and testing data. The mean error for this case is around 8% for the dielectric targets and around 7% for the conducting targets

Thus, the average classification error across all data sets in this study is less than 10%, assuming the number of training vectors used for SVM weight generation is not large enough to lead to overfitting. These results suggest that the phase patterns in the LSM solution vector contain information relevant to the target material properties and that this information can be exploited via a machine learning approach. Furthermore, it suggests that the LSM technique effectively isolates the signal contributions from each target in the scene by localizing its phase response to pixels in the vicinity of the target support.

We also report in Table 3 the mean testing error rates observed when the transmitter-to-pixel ranges $\mathbf{d}(\mathbf{r})$ are excluded from the training vectors. The results show that excluding the ranges increases the error rate in six of eight cases. The average error rate increase is about 1 percentage point across the eight cases, and the worst error rate increase is 4.4 percentage points. These results suggest that including $\mathbf{d}(\mathbf{r})$ in the training vectors is typically helpful. Further investigation is required to select the best features with which to augment the training matrix.

### *6.4.3 Future Work*

The favorable results reported in the previous subsection motivate continued study of machine learning approaches to extracting target information from the LSM solution vector. Future work will involve investigating machine-learning approaches for classification based on a wider variety of dielectric materials. This may include investigating and compensating for the effects of dielectric uncertainty or heterogeneity. A wider study of data collection parameters is also warranted. In particular, performance may be improved via alternate choices of frequencies. The frequencies in this study were chosen such that the targets are electrically small. Choosing higher frequencies, such that the targets span several wavelengths, may enable more complex LSM phase patterns in the target interiors, which may aid in material classification. Incorporating additional image features, such as the LSM pixel magnitude, may also improve performance. Lastly, enhancements may be available through the use of more complex machine learning approaches such as multilayer perceptrons or deep neural networks.

### 6.5 Conclusion

We investigated a machine-learning approach to classifying targets in qualitative inverse scattering imagery according to their electrical properties. We hypothesized that the phase associated with the LSM solution for target pixels contains exploitable target-material-dependent information. We evaluated this hypothesis by generating simulated scattered field training data for both dielectric and conducting targets, imaging the data using the LSM, constructing a support vector machine classifier using the phase of the LSM imagery, and applying the resulting classifier to simulated testing data. The proposed technique distinguished between dielectric and conducting targets in the testing set with error rates of less than 10% across all data sets, assuming the number of training vectors was chosen to avoid overfitting via a straightforward heuristic. The results support the validity of the proposed machine learning strategy. Additional performance enhancements may be achieved in future work by incorporating alternate frequency bands and LSM magnitude data into the support vector machine or by investigating strategies based on deep learning or neural networks.

## 7. A FAR-FIELD TRANSFORMATION PROCEDURE FOR MONOSTATIC LINEAR SAMPLING METHOD IMAGING

This section is adapted from a paper previously published in conference proceedings [37].

### 7.1 Background

Of the works that have addressed the problem of sparse aperture quantitative inverse scattering, there have been approaches that rely on incorporating multifrequency information either in the native frequency domain [77] or from a time-domain perspective [96]. Others such as [75] introduced more sophisticated regularization schemes that attempted to leverage additional priors from multispectral data. However, all of these approaches also would fail when both the transmit and receive apertures are sparse. What has been lacking in the literature are studies in which the LSM can exploit the highly redundant nature of multistatic data prior to inversion. Some examples of multistatic enrichment procedures have been presented in previous works such as in [97], where a pseudo total-variation scheme was considered; however, we argue the use of schemes such as total variation or Tikhonov for enrichment are local techniques that do not specifically leverage the fact that dense multistatic data is somehow low-dimensional.

In this section, we take a different approach toward an enrichment algorithm for qualitative inverse scattering with the specific case of imaging from monostatic geometries. Our approach is a two-step procedure that is based on exploiting multistatic redundancy from a K-space perspective. In the first step, we find regions where the support of monostatic and bistatic geometries intersect in K-space, which are then used to fill in the missing data points. The second step aims to complete the remainder of the bistatic apertures for which there is no intersection with monostatic support using a matrix completion procedure [98].

### 7.2 Preliminaries

For the sake of simplicity, we restrict ourselves to $\mathbb{R}^2$ in this work. Assume a homogeneous background medium embedding extended targets with reflectivity $\rho(\boldsymbol{x})$ and whose support $\Sigma \subset \mathbb{R}^2$ is compact with connected boundary $\Gamma$. Let $S$ denote the unit circle and let $u^i(\boldsymbol{x};\widehat{\boldsymbol{d}})$ represent an interrogating monochromatic planewave traveling in a direction $\widehat{\boldsymbol{d}} \subset S$ with wavenumber $k > 0$. The incident field induces a scattered field $u^s(\boldsymbol{x})$ for which the total field satisfies

$$\nabla^2 u(\boldsymbol{x}) + k^2 n(\boldsymbol{x}) = 0, \text{for } x \in \mathbb{R}^2 \backslash \Gamma \tag{32}$$

$$u(\boldsymbol{x}) = u^i(\boldsymbol{x}; \widehat{\boldsymbol{d}}) + u^s(\boldsymbol{x}) \tag{33}$$

$$\lim_{r \to \infty} \sqrt{r} \left( \frac{\partial u^s}{\partial r} - iku^s \right) = 0, r = |\boldsymbol{x}|. \tag{34}$$

Here, $n(\boldsymbol{x})$ is the index of refraction, which assumes the form $n(\boldsymbol{x}) = 1 - \rho(\boldsymbol{x})$. The total field $u(\boldsymbol{x})$ (in most reasonable cases) can be represented in the form of a Lippmann-Schwinger integral,

$$\min_{\mathbf{x}(\mathbf{r})} \|\mathbf{A}(\mathbf{r})\mathbf{x}(\mathbf{r}) - \mathbf{b}(\mathbf{r})\|^2, \tag{35}$$

where we have the homogeneous Green's function defined as

$$G(\boldsymbol{x}, \boldsymbol{y}) = \frac{i}{4} H_0^1(k|\boldsymbol{x} - \boldsymbol{y}|). \tag{36}$$

Writing Eq. (35) in operator form, we can compactly write the forward problem as

$$\left(I + k^2 A_\rho\right)^{-1} u(\boldsymbol{x}) = u^i(\boldsymbol{x}; \widehat{\boldsymbol{d}}), \tag{37}$$

where we have defined

$$A_\rho f(\boldsymbol{x}) \coloneqq \int_{\mathbb{R}^2} G(\boldsymbol{x}, \boldsymbol{y}) \rho(\boldsymbol{y}) f(\boldsymbol{y}) d^2 y. \tag{38}$$

The forward problem being well-posed [99] allows us to write

$$u(\boldsymbol{x}) = \left(I + k^2 A_\rho\right)^{-1} u^i(\boldsymbol{x}; \widehat{\boldsymbol{d}}). \tag{39}$$

The inverse scattering problem is to recover $\rho(\boldsymbol{x})$ from knowledge of the scattered field $u_s(\boldsymbol{x})$. Under the condition that $\|A_\rho\| < 1$, we can expand the inversion operator in Eq. (39) into a Neumann series [100]:

$$u(\boldsymbol{x}) = \left(I - k^2 A_\rho + k^4 A_\rho^2 - k^6 A_\rho^3 + \cdots\right) u^i(\boldsymbol{x}; \widehat{\boldsymbol{d}}). \min_{\mathbf{x}(\mathbf{r})} \|\mathbf{A}(\mathbf{r})\mathbf{x}(\mathbf{r}) - \mathbf{b}(\mathbf{r})\|^2. \tag{40}$$

From Eq. (40), we can see that although the mapping between $u$ and $u^i$ is linear, it is nonlinear between $u$, (and equivalently $u^s$) and $\rho$. The Born approximation, being a so-called weak scattering relaxation, dictates that only the first two terms in the expansion Eq. (40) is relevant, which effectively linearizes the inverse problem. Thus, retaining only the first two terms in Eq. (40) and then subtracting out the incident field from the equation, we obtain a linear relationship between $\rho$ and $u^s$,

$$u^s(\boldsymbol{x}) = -k^2 \int_{\mathbb{R}^2} G(\boldsymbol{x}, \boldsymbol{y}) \rho(\boldsymbol{y}) u(\boldsymbol{y}) d^2 y, \tag{41}$$

in the far-field where, as $r \to \infty$, we have that $u^s(\boldsymbol{x}, \widehat{\boldsymbol{d}})$ asymptotically approaches its corresponding far-field pattern $u_\infty^s(\widehat{\boldsymbol{x}}, \widehat{\boldsymbol{y}})$ and

$$G(\boldsymbol{x},\boldsymbol{y}) \longrightarrow G_\infty(\hat{\boldsymbol{x}},\boldsymbol{y}) = \frac{e^{\frac{i\pi}{4}}}{\sqrt{8\pi k}} e^{-ik\hat{\boldsymbol{x}}.\boldsymbol{y}}. \tag{42}$$

Therefore, in the far-field, we have

$$u_\infty^s(\hat{\boldsymbol{x}},\hat{\boldsymbol{y}}) = -\gamma \int_{\mathbb{R}^2} e^{-ik(\hat{\boldsymbol{x}}-\hat{\boldsymbol{d}}).\boldsymbol{y}} \rho(\boldsymbol{y}) d^2\boldsymbol{y}, \tag{43}$$

with

$$\gamma = \frac{k^2 e^{\frac{i\pi}{4}}}{\sqrt{8\pi k}}, \tag{44}$$

the spatial frequencies (knots) as $\boldsymbol{k} = k(\hat{\boldsymbol{x}} - \hat{\boldsymbol{d}})$, we obtain a Fourier relationship between the image and the Born-approximated scattered field,

$$u_\infty^{\mathrm{BA}} = -\gamma \int_{\mathbb{R}^2} e^{-i\boldsymbol{k}.\boldsymbol{y}} \rho(\boldsymbol{y}) d^2\boldsymbol{y}. \tag{45}$$

Conventional back-projection imaging is based on applying an inverse Fourier transform onto the scatter data to retrieve $\rho(\cdot)$.

### *7.2.1 Review of the LSM*

Qualitative imaging methods, like the LSM, take a different point of view of the inverse problem, where we aim to reconstruct the support $\Sigma$ rather than $\rho(\cdot)$ itself from the scattered data. A brief description of the LSM begins with defining the far-field operator $F: L^2(S) \to S$,

$$Fg(\hat{\boldsymbol{x}}) := \int_S u_\infty^s(\hat{\boldsymbol{x}},\hat{\boldsymbol{d}})\, g(\hat{\boldsymbol{d}}) ds(\hat{\boldsymbol{d}}). \tag{46}$$

Our aim is to find a weight function $g(\hat{\boldsymbol{d}},\boldsymbol{z}) \in L^2(S)$ so that the field resulting from application of Eq. (46) coincides with the far-field of a radiating point source located at $\boldsymbol{z} \in \Sigma$. In other words we aim to find a solution to the far-field equation

$$Fg(\hat{\boldsymbol{x}},\hat{\boldsymbol{z}}) = G_\infty(\hat{\boldsymbol{x}},\hat{\boldsymbol{z}}). \tag{47}$$

It can be shown [101] that for any $\epsilon > 0$, there always exists a density within $\epsilon$ distance of the point source that remains bounded whenever $\boldsymbol{z} \in \Sigma$. As $\boldsymbol{z} \to \Gamma$, any such approximating solution has the asymptotic behavior $\|g\|_{L^2(S)} \to \infty$ and remains unbounded for all $\boldsymbol{z} \in \Sigma^+$. In this sense, $\|g(\cdot,\boldsymbol{z})\|_{L^2(S)}$ forms the basis of an indicator function for the set $\Sigma$. Practical application of the technique however relies on a regularization solution to Eq. (17). The conventional approach is through Tikhonov regularization,

$$\min_{\|g(\cdot,\boldsymbol{z},k)\in L^2(S)\|} \|Fg - G_\infty\|_{L^2(S)}^2 + \alpha\|g\|_{L^2(S)}^2, \tag{48}$$

which is strictly convex for any $\alpha > 0$. There are a number of advantages for employing the Tikhonov approach: First, we can explicitly prove that this particular regularization scheme admits solutions that adhere to the properties we outlined above [102], and second, the solution can be computed in a rather efficient manner. We refer readers to section 3.1 of [75] for a discussion of an efficient numerical block-wise approach for Tikhonov-based LSM.

### 7.3 Monostatic to Multistatic Transformation

From Eq. (37), we can see that a major drawback to the LSM is the need to know $u_\infty^s(\cdot,\cdot)$ for all $(\hat{\boldsymbol{x}}, \hat{\boldsymbol{d}}) \in S \times S$, which is a considerable amount of spatial data. It is well known that when the data consists of only a few bistatic pairs, the LSM fails [103], and cannot even be applied with monostatic data in its native form. However, it is also well known that complete multistatic knowledge is overly redundant when frequency diversity is available, which is usually much easier to achieve in most applications.

Furthermore dense monostatic data over a band $B = [k_{\text{min}}, k_{\text{max}}]$ should contain enough information to image a scene in stable fashion, although again, it is not clear how techniques like LSM can leverage it. The spatial frequency representation of the data gives us perspective on how monostatic and multistatic geometries are related in terms of information overlap. In the monostatic case, the knots reduce to $\boldsymbol{k} = 2k\hat{\boldsymbol{k}}$, which means that the region of support is contained in an annular region $R$ centered at the origin as shown in Fig. 39. Now consider a single bistatic configuration with a fixed direction of incidence $\hat{\boldsymbol{d}}$ and fixed wavenumber $k_{\text{p}} \in (k_{\text{min}}, k_{\text{max}}]$. We see from Fig. 39 that the aperture traces out a circle $C_{\text{p}}$ (also known as an Ewald sphere [100]) centered at $k_p\hat{\boldsymbol{d}}$ with radius $k_{\text{p}}$. We can also observe that there is a segment of $C_{\text{p}}$ contained in $R$ while the remainder of bistatic aperture is outside the monostatic region of support. In fact, this holds for all $\hat{\boldsymbol{d}} \in S$ and for any $k_{\text{p}} \in (k_{\text{min}}, k_{\text{max}})$. The strategy is then clear: Given monostatic data on a band $B$, we aim to construct a virtual multistatic data set by filling in values on regions where the two coincide. As we can see in Fig. 39, this will yield data on a continuous portion of the aperture, while the remainder still remains unknown. However, under mild assumptions on $\Sigma$, the far-field data $u_\infty^s$ is analytic [104], thus for any $\hat{\boldsymbol{d}}$ and $k_{\text{p}}$, we can uniquely extend this function onto the entire aperture as justified by the principle of analytic continuation.

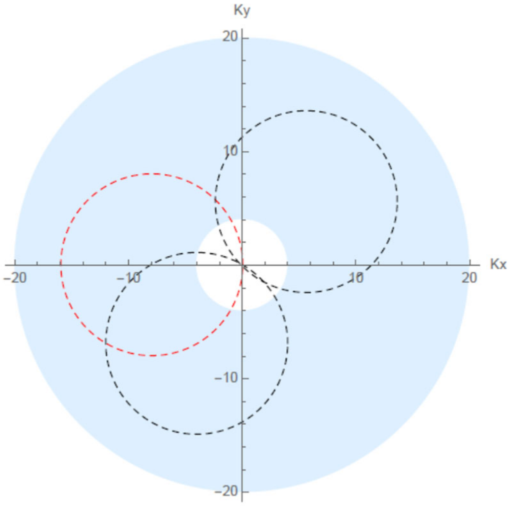

Fig. 39—An example of a full aperture monostatic region $R$ for $k_{\text{min}} = 2$ and $k_{\text{max}} = 10$, which is shaded in light blue. The dashed lines correspond to bistatic regions $C_{\text{p}}$ for $k_{\text{p}} = 8$, and 3 different incident angles. The white region contains spatial frequencies not captured by the monostatic geometry.

### 7.3.1 Far-Field Aperture Completion

The problem of extending $u_\infty(\widehat{\boldsymbol{x}}, \widehat{\boldsymbol{d}})$ for fixed $\widehat{\boldsymbol{d}}$ and $k > 0$ onto the entire aperture $S$ given knowledge of $u_\infty$ on a continuous subset of $S$ is known to be ill-posed. Previous works such as [105] use techniques such as Tikhonov or TV to regularize the inverse problem. However, we argue that these techniques have only a local point of view of the data and do not exploit multistatic redundancy as a prior. Instead, we look at the problem from the discrete perspective of matrix completion. In matrix completion [98], one seeks to predict/recover missing values of a matrix given the values of a small subset of known entries. The problem of course is highly ill-posed, however; it has been shown that if the underlying matrix is sufficiently low-rank, it can be recovered surprisingly accurately using a rather small number of known entries [98]. Furthermore, recovery of the matrix can be accomplished in polynomial time using convex optimization. To be more specific, let $\boldsymbol{X} \in \mathbb{C}^{n\times n}$ be a matrix and $P\colon \mathbb{C}^{n\times n} \to \mathbb{C}^{m\times 1}$ be the linear map that extracts the known $m$ entries of $\boldsymbol{X}$. We then seek to find a solution

$$\min_{\boldsymbol{X}\in\mathbb{C}^{n\times n}} \{\operatorname{rank}(\boldsymbol{X}) : \ \|P(\boldsymbol{X}) - b\|_2 < \epsilon\}. \tag{49}$$

While solving Eq. (49) is known to be NP-hard, a convex relaxation via the nuclear norm can be solved in polynomial time and under mild conditions can achieve an equivalent solution to Eq. (49). Therefore, we seek instead to solve

$$\min_{\boldsymbol{X}\in\mathbb{C}^{n\times n}} \left\{\|\boldsymbol{X}\|_{1,*} \colon P(\boldsymbol{X}) = b\right\} \tag{50}$$

with the nuclear norm defined as

$$\sum_{i=1}^{n} \sigma_i(\boldsymbol{X}), \tag{51}$$

and the $\sigma_i(\boldsymbol{X})$'s are the singular values of $\boldsymbol{X}$.

### 7.3.2 Discretized Numerical Approach

We now describe our numerical approach in more concrete terms. Given monostatic data at the spatial frequencies $\boldsymbol{k}_i$, which we assume are sampled sufficiently for the underlying scene, we interpolate the sampled data to obtain a model of $u_\infty^{\mathrm{BA}}(\boldsymbol{k})$ for all $\widehat{\boldsymbol{k}} \in R$. Next, we construct a $n \times n$ multistatic grid $(\widehat{\boldsymbol{x}}_i, \widehat{\boldsymbol{d}}_j)$, where $\widehat{\boldsymbol{x}}_i$ and $\widehat{\boldsymbol{d}}_j$ are the $i$th bistatic observation direction due to a planewave from the $j$th direction, for a chosen wavenumber $k_p \in (k_{\min}, k_{\max})$. These grid points will then correspond to a $n \times n$ multistatic response matrix $\boldsymbol{F}$ whose entries ideally would be given as

$$F_{ij} = u_\infty^{s}(\widehat{\boldsymbol{x}}_i, \widehat{\boldsymbol{d}}_j). \tag{52}$$

Let $\mathfrak{I}$ denote the index set $\{1,2,\dots,n\}$ and define the set of spatial frequencies

$$\mathcal{S} = \left\{\boldsymbol{k}_{i',j'} \in R \colon \boldsymbol{k}_{i',j'} = k_p(\widehat{\boldsymbol{x}}_{i'} - \widehat{\boldsymbol{d}}_{j'}), (i',j') \in \mathfrak{I}\times\mathfrak{I}\right\}. \tag{53}$$

Now let the index set $\mathcal{J} = 1, \dots, m = |\mathcal{S}|$ enumerate the set $\mathcal{S}$, for which we can define the mapping $P : \boldsymbol{F} \longmapsto \boldsymbol{b}$, where $\boldsymbol{b} \in \mathbb{C}^m$ is defined component-wise as

$$b_j = u_\infty^{\mathrm{BA}}(\boldsymbol{k}_j), \text{for } j \in \mathcal{J}. \qquad (54)$$

Then, for a defined tolerance $\epsilon > 0$, we complete the matrix $\boldsymbol{F}$ for the remainder of the entries via solving Eq. (50). In this work, we employ an accelerated proximal gradient (APG) approach similar in nature to the method employed in [106], the details of which we leave for a future paper.

### 7.4 Simulation Results

We present some imaging results to evaluate efficacy for the described monostatic LSM approach. For the first experiment, we consider a simple, perfectly conducting, kite-shaped target. For this scene, we simulated far-field scatter data corresponding to a low-frequency monostatic collection using a method of moments (MoM) code. The monostatic geometry was obtained at 1-degree increments for a band of frequencies corresponding to wavenumbers $k_{\min} = 2$ and $k_{\max} = 10$. For the virtual multistatic response data, we chose a grid of incident and observation directions both sampled in 1-degree increments, and set the desired wavenumber as $k_{\mathrm{p}} = 6$. Fig. 40 shows the simulated monostatic response, the virtual multistatic response corresponding to $k_{\mathrm{p}} = 6$ as obtained by our transformation procedure, and the associated LSM reconstruction obtained via Tikhonov regularization.

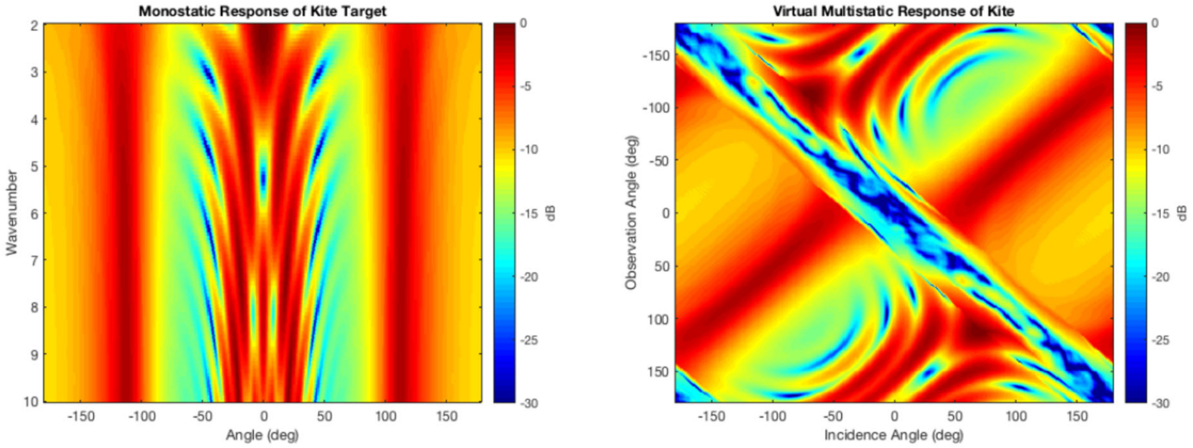

(a) Monostatic Data (b) Virtual Multistatic Data

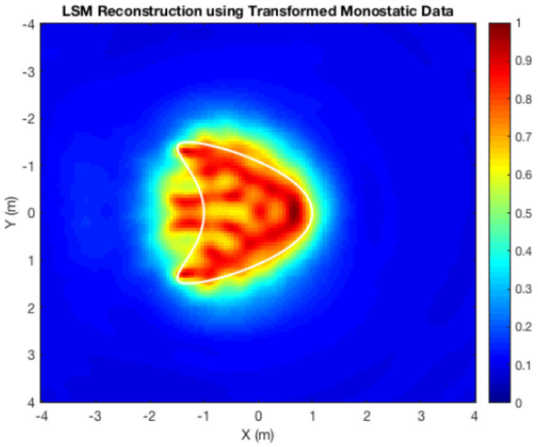

(c) LSM Reconstruction

Fig. 40—Results for a simple example of imaging a kite PEC scatterer, a) simulated monostatic data of the kite across angle and frequency. b) Virtual multistatic data corresponding to a single wavenumber $k_p = 6$ using 1-degree sampling in both observation and incidence. c) The resulting LSM reconstruction.

For the second experiment, we consider 2D monostatic scatter data taken from a detailed simulation [107] of the DJI Phantom II quadcopter target. The scatter data was obtained by FDTD code developed at ARL, where the monostatic response was measured again at every 1 degree over a 1-10 GHz range, which corresponded to approximately to $k_{\text{min}} = 21$ and $k_{\text{max}} = 209$. Looking at the HH monostatic response of the quadcopter target in Fig. 41, we note that the data does not exhibit as much symmetry as the kite's monostatic response. For our LSM reconstruction, we chose $k_p = 170$ and, as before, sampled both incidence and observation apertures using 1-degree increments. The resulting reconstruction of the quadcopter is also shown in Fig. 41.

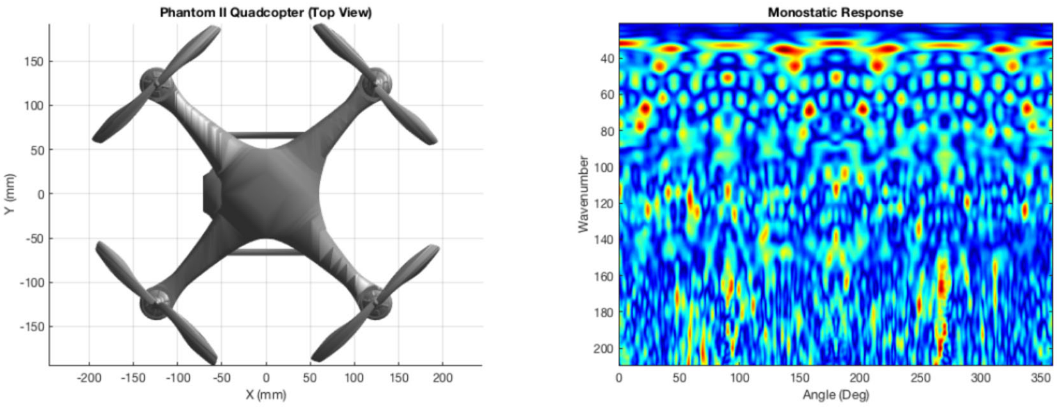

(a) Quadcopter Target (b) Virtual Multistatic Data

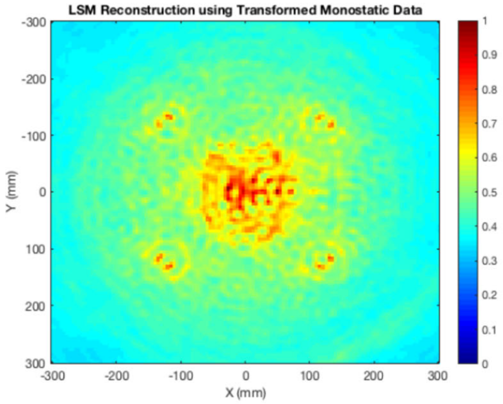

(c) LSM Reconstruction

Fig. 41—Reconstruction of the DJI Phantom quadcopter target a) A 3D model of the quadcopter oriented in the same direction as was used in the 2D FDTD simulation. b) The monostatic response in terms of wavenumber and angle. c) LSM reconstruction using the virtual multistatic data at virtual wavenumber $k_p = 170$ and 1-degree sampling in both observation and incidence.

## 7.5 Summary and Future Work

To summarize, in this paper, we presented an enrichment procedure that mapped dense monostatic data into a virtual multistatic data for the purpose of applying LSM-based imaging when only monostatic data is available. As discussed, the procedure was based on finding spatial frequency regions of common support which was then followed by a matrix completion algorithm to extend the predicted data onto the entire multistatic apertures. There are several clear paths of future extensions of this work. First, all frequencies should be incorporated simultaneously instead of pursuing enrichment on a single-frequency basis. Second, extension of the approach to the full 3D and polarimetric LSM framework remains to be investigated. More fundamentally, however, while the simulations given here do indicate initial efficacy of the approach, several questions still remain, as we note that the argument behind the presented procedure is only valid under the Born approximation, which goes against one of the main arguments for using the LSM in the first place. Therefore, as future work, it would be interesting to compare the LSM reconstructions using the procedure using data for which the Born approximation is satisfied as well as images obtained using conventional backprojection. More importantly, the work here lays the foundation for an enrichment procedure for when some bistatic data is known and needs to be extended to denser multistatic grids. In this case, we anticipate the procedure would be very similar to what we described here, and that reliance on the Born approximation should be less of an issue.

## 8. CONCLUSION

In this document, we reported the results of an NRL 6.1 Base Program project towards the development of RF imaging techniques that overcome the limitations of simplified linear scattering models used by most radar algorithms. The development goal was to achieve imagery of high fidelity to the true target geometry by leveraging a more complete electromagnetic model. The algorithm framework was the linear sampling method (LSM), an imaging technique that avoids simplified scattering models but is challenging to implement in practical scenarios due to its need for spatially dense, wide-angle, multistatic sensor arrays.

To overcome this challenge, we created new LSM-based imaging algorithms that mitigated the lack of spatial channels by incorporating information from other domains. We used the perspective of the LSM as a transmit-focusing problem and our knowledge of propagation and electromagnetics to constrain and stabilize the LSM solution. We sought to leverage both the magnitude and phase of the LSM solution, in contrast to much prior LSM work that focused only on the magnitude. We also developed new methods to leverage the information content inherent in multifrequency data.

These development strategies resulted in several effective, new imaging techniques. The phase-delay frequency variation (PDFV) LSM achieved fidelity by constraining the phase of the LSM solution to maintain an incident field focus in the imaging domain. The boundary-condition-enhanced LSM improved imaging performance against conducting targets by constraining the solution in order to satisfy electric field boundary conditions on the target surface. The beamforming-enhanced LSM allowed for imaging in limited-aspect scenarios, which are particularly challenging for conventional LSM, by incorporating a receive-beamforming enhancement into the PDFV-LSM. A new machine learning strategy used the LSM phase to classify the electrical properties of targets. Lastly, a frequency-domain interpolation method allowed for monostatic LSM imaging by leveraging data redundancy across frequency.

The imaging results from these techniques demonstrated significantly improved fidelity compared to conventional LSM processing across a variety of imaging geometries, including dense-transmit, sparse receive scenarios; limited-aspect scenarios; and monostatic scenarios. The robustness of the techniques was demonstrated by generating results using a variety of datasets, including finite-difference time-domain simulation as well as laboratory-collected experimental datasets from multiple publicly available external sources.

There are a number of interesting research avenues remaining for future work. The new techniques should be adapted and evaluated for three-dimensional apertures and three-dimensional targets. Imaging effectiveness should be investigated using a greater variety of experimental datasets and complex experimental targets. The challenging sparse-transmit, sparse-receive scenario should be addressed. Techniques should be developed for extracting features from the LSM imagery for automatic target recognition or classification. In particular, the use of target internal resonances, which are described in Section 4 and are somewhat unique to LSM, should be explored for this purpose. Lastly, challenges for LSM imaging in the field, such as generating appropriate Green's functions for the right-hand side of the LSM equation in Eq. (1), should be addressed.

## REFERENCES

[1] K. El-Darymli, E. Gill, P. Mcguire, D. Power and C. Moloney, "Automatic Target Recognition in Synthetic Aperture Radar Imagery: A State-of-the-Art Review," *IEEE Access,* vol. 4, pp. 6014-6058, 2016.

[2] M. Saville and J. Jackson, "Rethinking vehicle classification with wide-angle polarimetric SAR," *IEEE Aerospace and Electronics Systems Magazine,* vol. 29, no. 1, pp. 41-49, 2014.

[3] M. Saville, J. Compaleo, H. Judd and J. Smith, "Designing ISAR Lab Experiments for EO-SAR ATR," *IEEE Photonics Journal,* vol. 11, no. 3, p. 6602010, 2019.

[4] L. Potter and R. Moses, "Attributed Scattering Centers for SAR ATR," *IEEE Transactions on Image Processing,* vol. 6, no. 1, pp. 79-91, 1997.

[5] M. Horvath and B. Rigling, "Performance Prediction of Quantized SAR ATR Algorithms," *IEEE Transactions on Aerospace and Electronic Systems,* vol. 52, no. 1, pp. 189-204, 2016.

[6] E. Laubie, B. Rigling and R. Penno, "An empirical look at cross-target correlation in bistatic SAR images," in *Proceeding of the IEEE Radar Conference*, Oklahoma City, 2018.

[7] I. Catapano, L. Crocco and T. Isernia, "Improved sampling methods for shape reconstruction of 3-D buried targets," *IEEE Transactions on Geoscience and Remote Sensing,* vol. 46, no. 10, p. 3265–3273, 2008 .

[8] T. Counts, A. Cafer Gurbuz, W. Scott, Jr., J. McClellan and K. Kim, "Multistatic Ground-Penetrating Radar Experiments," *IEEE Transactions on Geoscience and Remote Sensing,* vol. 45, no. 8, pp. 2544-2553, 2007.

[9] M. Garcia-Fernandez, Y. Alvarez-Lopez and F. Las Heras, "Autonomous Airborne 3D SAR Imaging System for Subsurface Sensing: UWB-GPR on Board a UAV for Landmine and IED Detection," *Remote Sensing,* vol. 11, 2019.

[10] Y. Fuse, B. Gonzalez-Valdes, J. Martinez-Lorenzo and C. Rappaport, "Advanced SAR Imaging Methods for Forward-Looking Ground Penetrating Radar," in *European Conference on Antennas and Propagation*, Davos, Switzerland, 2016.

[11] L. Monte, D. Erricolo, F. Soldovieri and M. Wicks, "Radio Frequency Tomography for Tunnel Detection," *IEEE Transactions on Geoscience and Remote Sensing,* vol. 48, no. 3, pp. 1128-1137, 2010.

[12] S. Cogar, D. Colton and P. Monk, "Using eigenvalues to detect anomalies in the exterior of a cavity," *Inverse Problems,* vol. 34, p. 085006, 2018.

[13] F. Cakoni, S. Cogar and P. Monk, "A Spectral Approach to Nondestructive Testing via Electromagnetic Waves," *IEEE Transactions on Antennas and Propagation,* accepted, 2021.

[14] J. Tobón Vásquez, R. Scapaticci, G. Turvani, M. Ricci, L. Farina, A. Litman, M. Casu, L. Crocco and F. Vipiana, "Noninvasive Inline Food Inspection via Microwave Imaging Technology," *IEEE Antennas and Propagation Magazine,* vol. 62, no. 5, pp. 18-32, 2020.

[15] C. Gilmore, M. Asefi, J. Paliwal and J. LoVetri, "Industrial scale electromagnetic grain bin monitoring," *Computers and Electronics in Agriculture,* vol. 136, pp. 210-220, 2017.

[16] L. Farina, R. Scapaticci, J. Tobon Vasquez, J. Rivero, A. Litman, L. Crocco and F. Vipiana, "Microwave Imaging Technology for In-line Food Contamination Monitoring," in *Proceedings of the IEEE International Symposium on Antennas and Propagation and USNC-URSI Radio Science Meeting*, Atlanta, 2019.

[17] M. Mallach, P. Gebhardt and T. Musch, "2D microwave tomography system for imaging of multiphase flows in metal pipes," *Flow measurements and instrumentation,* vol. 53, pp. 80-88, 2017.

[18] H. Alidoustaghdam and M. Çayören, "Flow monitoring by microwave imaging inside a cuboid cavity: Theory and numerical feasibility analysis," *Flow Measurement and Instrumentation,* accepted, 2021.

[19] P. Meaney, M. Fanning, D. Li, S. Poplack and K. Paulsen, “A Clinical Prototype for Active Microwave Imaging of the Breast,” *IEEE Transactions on Microwave Theory and Techniques,* vol. 48, no. 11, pp. 1841-1853, 2000.

[20] T. Grzegorczyk, P. Meaney, P. Kaufman, R. diFlorio-Alexander and K. Paulsen, “Fast 3-D Tomographic Microwave Imaging for Breast Cancer Detection,” *IEEE Transactions on Medical Imaging,* vol. 31, no. 8, pp. 1584-1592, 2012.

[21] M. N. Akinci, M. Cayoren and E. Gose, “Qualitative Microwave Imaging of Breast Cancer with Contrast agents,” *Physics in Medicine and Biology,* vol. 64, no. 11, p. 115018, 2019.

[22] P. Meaney, D. Goodwin, A. Golnabi, T. Zhou, M. Pallone, S. Geimer, G. Burke and K. Paulsen, “Clinical Microwave Tomographic Imaging of the Calcaneus: A First-in-Human Case Study of Two Subjects,” *IEEE Transactions on Biomedical Engineering,* vol. 59, no. 12, pp. 3304-3313, 2012.

[23] I. Bisio, C. Estatico, A. Fedeli, F. Lavagetto, M. Pastorino, A. Randazzo and A. Sciarrone, “Brain Stroke Microwave Imaging by Means of a Newton-Conjugate-Gradient Method in Lp Banach Spaces,” *IEEE Transactions on Microwave Theory and Techniques,* vol. 66, no. 8, pp. 3668-3682, 2018.

[24] C. Dachena, A. Fedeli, A. Fanti, M. Lodi, M. Pastorino and A. Randazzo, “A Microwave Imaging Technique for Neck Disease Monitoring,” in *Proceedings of the European Conference on Antennas and Propagation*, Dusseldorf, Germany, 2021.

[25] C. Dachena, A. Fanti, A. Fedeli, G. Mazzarella, M. Pastorino and A. Randazzo, “Microwave Imaging of Cervical Myelopathy: A Preliminary Feasibility Assessment,” in *Proceedings of the European Conference on Antennas and Propagation*, Copenhagen, Denmark, 2020.

[26] M. Cheney and B. Borden, Fundamentals of Radar Imaging, Philadelphia: Society for Industrial and Applied Mathematics, 2009.

[27] F. Cakoni, D. Colton and P. Monk, The Linear Sampling Method in Inverse Electromagnetic Scattering, Philadelphia: Society for Industrial and Applied Mathematics, 2011.

[28] Y. M. Wang and W. C. Chew, “An Iterative Solution of the Two-Dimensional Electromagnetic Inverse Scattering Problem,” *International Journal of Imaging Systems and Technology,* vol. 1, pp. 100-108, 1989.

[29] W. C. Chew and Y. M. Wang, “Reconstruction of Two-Dimensional Permittivity Distribution Using the Distorted Born Iterative Method,” *IEEE Transactions on Medical Imaging,* vol. 9, no. 2, pp. 218-225, 1990.

[30] P. van den Berg and R. Kleinman, “A contrast source inversion method,” *Inverse Problems,* vol. 13, p. 1607–1620, 1997.

[31] M. J. Burfeindt and H. F. Alqadah, “Qualitative Inverse Scattering for Sparse-Aperture Data Collections Using a Phase-Delay Frequency Variation Constraint,” *IEEE Transactions on Antennas and Propagation,* vol. 68, no. 11, pp. 7530-7540, 2020.

[32] M. Burfeindt and H. Alqadah, “Boundary-condition-enhanced linear sampling method imaging of conducting targets from sparse receivers,” *IEEE Transactions on Antennas and Propagation,* accepted, 2021.

[33] M. Burfeindt and H. Alqadah, “Sparse-aperture qualitative inverse scattering using a phase-delay-based frequency variation constraint,” in *Proceedings of the IEEE Research and Applications of Photonics in Defense Conference*, Miramar Beach, FL, 2019.

[34] M. J. Burfeindt and H. F. Alqadah, “Machine learning for extracting target electrical parameters from qualitative inverse scattering imagery,” in *Proceedings of the SPIE 11408, Radar Sensor Technology XXIV*, online, 2020.

[35] M. J. Burfeindt and H. F. Alqadah, “Enhancement of Linear Sampling Method imaging of conducting targets using a boundary condition constraint,” in *Proceedings of the IEEE Research and Applications of Photonics in Defense (RAPID) Conference*, online, 2020.

[36] M. Burfeindt and H. Alqadah, “Receive-beamforming-enhanced Linear Sampling Method Imaging,” in *Proceedings of the IEEE Research and Applications of Photonics in Defense (RAPID) Conference*, online, 2021.

[37] H. Alqadah and M. Burfeindt, “A Far-Field Transformation Procedure for Monostatic Linear Sampling Method Imaging,” in *International Conference on Electromagnetics in Advanced Applications*, Granada, Spain, 2019.

[38] M. J. Burfeindt and H. F. Alqadah, “Sparse Aperture Multistatic Radar Imaging Techniques: FY19 Summary Report,” NRL/MR/5341-20-10083, 2019.

[39] M. Burfeindt and H. Alqadah, “Sparse Aperture Multistatic Radar Imaging Techniques: FY20 Summary Report,” in preparation, 2021.

[40] I. Catapano, L. Crocco and T. Isernia, “On simple methods for shape reconstruction of unknown scatterers,” *IEEE Transactions on Antennas and Propagation,* vol. 55, no. 5, p. 1431–1436, 2007.

[41] C. Balanis, Advanced Engineering Electromagnetics, New York: John Wiley and Sons, 1989.

[42] N. Shelton and K. F. Warnick, “Behavior of the regularized sampling inverse scattering method at internal resonance frequencies,” *Progress in Electromagnetics Research,* vol. 38, pp. 29-45, 2002.

[43] H. F. Alqadah, “A Compressive Multi-Frequency Linear Sampling Method for Underwater Acoustic Imaging,” *IEEE Transactions on Image Processing,* vol. 25, no. 6, pp. 2444-2455, 2016.

[44] I. Catapano, L. Crocco and T. Isernia, “On Simple Methods for Shape Reconstruction of Unknown Scatterers,” *IEEE Transactions on Antennas and Propagation,* vol. 55, no. 5, pp. 1431-1436, 2007.

[45] L. Crocco, L. Di Donato, I. Catapano and T. Isernia, “An Improved Simple Method for Imaging the Shape of Complex Targets,” *IEEE Transactions on Antennas and Propagation,* vol. 61, no. 2, pp. 843-851, 2013.

[46] K. Agarwal, X. Chen and Y. Zhong, “A Multipole-Expansion Based Linear Sampling Method for Solving Inverse Scattering Problems,” *Optics Express,* vol. 18, no. 6, pp. 6366-6381, 2010.

[47] P. C. Hansen, Rank-Deficient and Discrete Ill-Posed Problems, Philadelphia: Society for Industrial and Applied Mathematics, 1998.

[48] L. Poli, G. Oliveri and A. Massa, “Imaging sparse metallic cylinders through a local shape function Bayesian compressive sensing approach,” *Journal of the Optical Society of America,* vol. 30, no. 6, pp. 1261-1272, 2013.

[49] T. Takenaka, Z. Meng, T. Tanaka and W. Chew, “Local shape function combined with genetic algorithm applied to inverse scattering for strips,” *Microwave and Optical Technology Letters,* vol. 16, pp. 337-341, 1997.

[50] G. Otto and W. Chew, “Microwave Inverse Scattering-Local Shape Function Imaging for Improved Resolution of Strong Scatterers,” *IEEE Transactions on Microwave Theory and Technology,* vol. 42, no. 1, pp. 137-141, 1994.

[51] X. Ye, “Electromagnetic Imaging of Wave Impenetrable Objects,” in *Proceedings of the 11th European Conference on Antennas and Propagation*, Paris, France, 2017.

[52] X. Ye, X. Chen, Y. Zhong and K. Argawal, “Subspace-Based Optimization Method for Reconstructing Perfectly Electric Conductors,” *Progress in Electromagnetic Research,* vol. 100, pp. 119-218, 2010.

[53] X. Ye, Y. Zhong and X. Chen, “Reconstructing perfectly electric conductors by the subspace-based optimization method with continuous variables,” *Inverse Problems,* vol. 27, p. 055011, 2011.

[54] J. Shen, Y. Zhong and L. Ran, "Inverse Scattering Problems of Reconstructing Perfectly Electric Conductors With TE Illumination," *IEEE Transactions on Antennas and Propagation,* vol. 61, no. 9, pp. 4713-4721, 2013.

[55] M. Stevanovic, L. Crocco, A. Djordjevic and A. Nehorai, "Higher Order Sparse Microwave Imaging of PEC Scatterers," *IEEE Transactions on Antennas and Propagation,* vol. 64, no. 3, pp. 988-997, 2016.

[56] N. Vojnovic, M. Stevanovic, L. Crocco and A. Djordjevic, "High-Order Sparse Shape Imaging of PEC and Dielectric Targets Using TE Polarized Fields," *IEEE Transactions on Antennas and Propagation,* vol. 66, no. 4, pp. 2035-2043, 2018.

[57] M. Nikolic, A. Nehorai and A. Djordjevic, "Electromagnetic Imaging of Hidden 2-D PEC Targets Using Sparse-Signal Modeling," *IEEE Transactions on Geoscience and Remote Sensing,* vol. 51, no. 5, pp. 2707-2721, 2013.

[58] M. Bevacqua and T. Isernia, "Shape Reconstruction via Equivalence Principles, Constrained Inverse Source Problems and Sparsity Promotion," *Progress in Electromagnetic Research,* vol. 158, pp. 37-48, 2017.

[59] M. Bevacqua and R. Palmeri, "Qualitative Methods for the Inverse Obstacle Problem: A Comparison on Experimental Data," *Journal of Imaging,* vol. 5, no. 4, p. 47, 2019.

[60] S. Sun, B. Kooij, A. Yarovoy and T. Jin, "A Linear Method for Shape Reconstruction Based on the Generalized Multiple Measurement Vectors Model," *IEEE Transactions on Antennas and Propagation,* vol. 66, no. 4, pp. 2016-2025, 2018.

[61] F. Wang and Q. Liu, "A Bernoulli–Gaussian Binary Inversion Method for High-Frequency Electromagnetic Imaging of Metallic Reflectors," *IEEE Transactions on Antennas and Propagation,* vol. 68, no. 4, pp. 3184-3193, 2020.

[62] F. Soldovieri, A. Brancaccio, G. Leone and R. Pierri, "Shape Reconstruction of Perfectly Conducting Objects by Multiview Experimental Data," *IEEE Transactions on Geoscience and Remote Sensing,* vol. 43, no. 1, pp. 65-71, 2005.

[63] R. Solimene, A. Buonanno, F. Soldovieri and R. Pierri, "Physical Optics Imaging of 3-D PEC Objects: Vector and Multipolarized Approaches," *IEEE Transactions on Geoscience and Remote Sensing,* vol. 48, no. 4, pp. 1799-1808, 2010.

[64] T. Benoudiba-Campanini, J. Giovannelli and P. Minvielle, "SPRITE: 3-D SParse Radar Imaging Technique," *IEEE Transactions on Computational Imaging,* vol. 6, pp. 1059-1069, 2020.

[65] C. Austin, E. Ertin and R. Moses, "Sparse Signal Methods for 3-D Radar Imaging," *IEEE Journals of Select Topics in Signal Processing,* vol. 5, no. 3, pp. 408-423, 2011.

[66] X. Ren, L. Qiao, Y. Qin and P. Li, "Sparse Regularization Based Imaging Method for Inverse Synthetic Aperture Radar," in *Proceedings of the IEEE Progress in Electromagnetic Research Symposium*, Shanghai, China, 2016.

[67] G. Zhang, W. Wang and W. Wang, "Energy Estimation Based TR-MUSIC Microwave Imaging of Extended Targets," *Progress in Electromagnetics Research B,* vol. 47, pp. 107-126, 2013.

[68] R. Solimene and A. Dell'Aversano, "Some Remarks on Time-Reversal MUSIC for Two-Dimensional Thin PEC Scatterers," *IEEE Geoscience and Remote Sensing Letters,* vol. 11, no. 6, pp. 1163-1167, 2014.

[69] M. Hajihashemi and M. El-Shenawee, "TE Versus TM for the Shape Reconstruction of 2-D PEC Targets Using the Level-Set Algorithm," *IEEE Transactions on Geoscience and Remote Sensing,* vol. 48, no. 3, pp. 1159-1168, 2010.

[70] M. Hajihashemi and M. El-Shenawee, "Shape Reconstruction Using the Level Set Method for Microwave Applications," *IEEE Antennas and Wireless Propagation Letters,* vol. 7, pp. 92-96, 2008.

[71] M. Hajihashemi and M. El-Shenawee, "Inverse Scattering of Three-Dimensional PEC Objects Using the Level-Set Method," *Progress in Electromagnetics Research,* vol. 116, pp. 23-47, 2011.

[72] A. Hassan, T. Bowman and M. El-Shenawee, "Efficient Microwave Imaging Algorithm Based on Hybridization of the Linear Sampling and Level Set Methods," *IEEE Transactions on Antennas and Propagation,* vol. 61, no. 7, pp. 3765-3773, 2013.

[73] M. Cheney, "The Linear Sampling Method and the MUSIC Algorithm," *Inverse Problems,* vol. 17, pp. 591-595, 2000.

[74] B. Guzina, F. Cakoni and C. Bellis, "On the multifrequency obstacle reconstruction via the linear sampling method," *Inverse Problems,* vol. 29, p. 125005, 2010.

[75] H. Alqadah and N. Valdivia, "A Frequency Based Constraint for a Multi-Frequency Linear Sampling Method," *Inverse Problems,* vol. 29, no. 9, p. 095019, 2013.

[76] H. Alqadah, "A Compressive Multi-Frequency Linear Sampling Method for Underwater Acoustic Imaging," *IEEE Transactions on Image Processing,* vol. 25, no. 6, pp. 2444-2455, 2016.

[77] F. Cakoni, D. Colton and H. Haddar, "On the Determination of Dirichlet and Transmission Eigenvalues from Far Field Data," *Comptes Rendus Mathematique,* vol. 348, pp. 379-383, 2010.

[78] F. Cakoni, D. Colton and P. Monk, "On the use of transmission eigenvalues to estimate the index of refraction from far field data," *Inverse Problems,* vol. 23, pp. 507-522, 2007.

[79] F. Cakoni, M. Cayoren and D. Colton, "Transmission eigenvalues and nondestructive testing of dielectrics," *Inverse Problems,* vol. 24, p. 065016, 2008.

[80] H. Alqadah, "Resonant Mode Feature Extraction via a Compressive Multi-Frequency Linear Sampling Method," in *Proceedings of the International Conference on Electromagnetics in Advanced Applications*, Queensland, Australia, 2016.

[81] H. Alqdah, "Space-Frequency Regularization for Qualitative Inverse Scattering," PhD Dissertation, University of Cincinnati , 2011.

[82] C. Gilmore, A. Zakaria, P. Mojabi, M. Ostadrahimi, S. Pistorius and J. LoVetri, "The University of Manitoba Microwave Imaging Repository: A Two-Dimensional Microwave Scattering Database for Testing Inversion and Calibration Algorithms," *IEEE Antennas and Propagation Magazine,* vol. 53, no. 5, pp. 126-133, 2011.

[83] K. Belkebir and M. Saillard, "Special Section: Testing Inversion Algorithms Against Experimental Data," *Inverse Problems,* vol. 17, pp. 1565-1571, 2001.

[84] M. Akıncı, M. Çayören and I. Akduman, "Near-field orthogonal sampling method for microwave imaging: theory and experimental verification," *IEEE Transactions on Microwave Theory and Techniques,* vol. 64, no. 8, pp. 2489-2501, 2016.

[85] K. Leem, J. Liu and G. Pelekanos, "Two direct factorization methods for inverse scattering problems," *Inverse Problems,* vol. 34, p. 125004, 2018.

[86] M. Burfeindt, J. Shea, B. Van Veen and S. Hagness, "Beamforming-Enhanced Inverse Scattering for Microwave Breast Imaging," *IEEE Transactions on Antennas and Propagation,* vol. 62, no. 10, pp. 5126-5132, 2014.

[87] A. Abubakar, T. Habashy and G. Pan, "Microwave Data Inversions Using the Source-Receiver Compression Scheme," *IEEE Transactions on Antennas and Propagation,* vol. 60, no. 6, pp. 2853-2864, 2012.

[88] M. Ambrosanio, M. Bevacqua, T. Isernia and V. Pascazio, "Experimental multistatic imaging via the linear sampling method," in *Proceedings of the IEEE International Geoscience and Remote Sensing Symposium*, 2019.

[89] S. Caorsi and P. Gamba, “Electromagnetic Detection of Dielectric Cylinders by a Neural Network Approach,” *IEEE Transaction on Geoscience and Remote Sensing* , vol. 37, no. 2, pp. 820-827, 1999.

[90] I. Rekanos, “Neural-Network-Based Inverse-Scattering Technique for Online Microwave Medical Imaging,” *IEEE Transactions on Magnetics,* vol. 38, no. 2, pp. 1061-1064, 2002.

[91] R. Guo, M. Li, F. Yang, S. Xu, G. Fang and A. Abubakar, “Application of Supervised Descent Method to Nonlinear Inversion for Transient EM Data,” in *European Conference on Antennas and Propagation*, 2018.

[92] R. Guo, X. Song, M. Li, F. Yang, S. Xu and A. Abubakar, “Imaging of Two Dimensional Scatterers using Descent Learning Techniques,” in *APS/URSI*, 2018.

[93] P. Shah, G. Chen and M. Moghaddam, “Learning Nonlinearity of Microwave Imaging Through Deep Learning,” in *APS/URSI*, 2018.

[94] L. Li, L. Wang, F. Teixeira, C. Lui, A. Nehorai and T. Cui, “DeepNIS: Deep Neural Network for Nonlinear Electromagnetic Inverse Scattering,” *IEEE Transactions on Antennas and Propagation,* vol. 67, no. 3, pp. 1819-1825, 2019.

[95] J. Platt, “Fast Training of SVMs Using Sequential Minimal Optimization,” MIT Press, Cambridge, MA, Advances in Kernel Method - Support Vector Learning.

[96] Q. Chen, H. Haddar, A. Lechleiter and P. Monk, “A Sampling Method for Inverse Scattering in the Time Domain,” *Inverse Problems,* vol. 26, p. 085001, 2010.

[97] A. Barucq, C. Bekley and R. Djellouli, “A Multi-Step Procedure for Enriching Limited Two-Dimensional Acoustic Far-Field Pattern Measurements,” *Journal of Inverse and Ill-Posed Problems,* vol. 18, pp. 189-216, 2010.

[98] E. Candes and B. Recht, “Exact Matrix Completion via Convex Optimization,” *Foundations of Computational Mathematics,* vol. 9, p. 717, 2009.

[99] W. McLean, Strongly Elliptic Systems and Boundary Integral Equations, Cambridge University Press, 2000.

[100] A. Devaney, Mathematical Foundations of Imaging, Tomography, and Wavefield Inversion, Cambridge University Press, 2012.

[101] F. Cakoni and D. Colton, “On the Mathematical Basis of the Linear Sampling Method,” *Georgian Math Journal,* vol. 10, pp. 95-104, 2003.

[102] T. Arens and A. Lechleiter, “The Linear Sampling Method Revisited,” *Journal of Integral Equations and Applications,* vol. 21, pp. 179-202, 2009.

[103] H. Alqadah, N. Valdivia and E. Williams, “High Resolution Near-Field Electromagnetic Holography for Dynamic Source Identification in Underwater Mediums,” *Progress in Electromagetic Research,* vol. 65, pp. 109-127, 2016.

[104] D. Colton and R. Kress, Inverse Acoustic and Electromagnetic Scattering Theory, Springer, 1998.

[105] H. Barucq, C. Bekkey and R. Djellouli, “Full Aperture Reconstruction of the Acoustic Far-Field Pattern from Few Measurements,” *Communications on Computational Physics,* vol. 11, pp. 647-659, 2012.

[106] Z. Shen, K. Chuan Toh and S. Yun, “An Accelerated Proximal Gradient Algorithm for Nuclear Norm Regularized Linear Least Squares Problems,” *Pacific Journal of Optimization,* pp. 615-640, 2010.

[107] T. Dogaru, K. Gallagher and C. Le, “Doppler Radar Phenomenology in Small Commercial Unmanned Aerial Systems,” in *IEEE International Symposium on Antennas and Propagation and USNC/URSI National Radio Science Meeting*, 2017.